NORTHWESTERN UNIVERSITY

Mechanics-informed Diagnosis and Treatment Planning: Application to Esophageal Disorders

A DISSERTATION

SUBMITTED TO THE GRADUATE SCHOOL

IN PARTIAL FULFILLMENT OF THE REQUIREMENTS

for the degree

DOCTOR OF PHILOSOPHY

Field of Theoretical and Applied Mechanics

By

Sourav Halder

EVANSTON, ILLINOIS

June 2023

© Copyright by Sourav Halder 2023

All Rights Reserved

ABSTRACT

Mechanics-informed Diagnosis and Treatment Planning: Application to Esophageal Disorders

Sourav Halder

The esophagus plays a crucial role in the functioning of the gastrointestinal tract and esophageal disorders are associated with reduced quality of life. Several studies have reported that there is a high worldwide prevalence of esophageal disorders. Esophageal disorders are related to the mechanical properties and function of the esophageal wall. Therefore, to understand the underlying fundamental mechanisms behind various esophageal disorders, it is crucial to map mechanical behavior of the esophageal wall to altered bolus transit and increased intrabolus pressure. This thesis demonstrates how mechanics can be used for better diagnosis of esophageal disorders, improved treatment planning, and identifying the unique mechanical characteristics of various esophageal disorders. To begin with, an in silico model is presented to estimate the optimal parameters of an esophageal surgery called myotomy to reduce the risk of formation of a complication called blown-out myotomy (BOM). Furthermore, two frameworks are described that work with the esophageal diagnostic tests: fluoroscopy and magnetic resonance imaging (MRI),

to estimate the mechanical "health" of the esophagus through a set of mechanics-based parameters such as esophageal wall stiffness and active relaxation. These frameworks not only provide valuable information about the underlying wall mechanics behind the measurements of the diagnostic devices but also increase the capabilities of these diagnostic technologies either by adding automation or by increasing the resolution of the images generated by them. Finally, a framework called mechanics-informed variational autoencoder (MI-VAE) is described which generates a mechanics-based parameter space called virtual disease landscape (VDL). Clusters of various esophageal disorders and normal function form within the VDL which help capture similarities and dissimilarities between various diseases. This also helps in identifying mechanical physiomarkers that distinguish the various esophageal disorders. In addition, the VDL helps in estimating the effectiveness of treatments and tracking patient condition over time. Together, these frameworks provide a formal approach by which mechanics can be meaningfully used for diagnosis and treatment planning.

Acknowledgements

First and foremost, I would like thank God Almighty for His blessings throughout my PhD. It is by His grace that I exist, and without whom I could never have achieved anything in my life.

I consider myself extremely lucky to have Prof. Neelesh A. Patankar as my advisor. I am grateful to him for introducing me to the exciting research area of esophageal mechanics and it is my privilege to work with one of the pioneers in this field. Prof. Patankar has not only helped me in developing a discipline in rigorous scientific research, but also taught me to think freely while tackling difficult problems. His support and encouragement kept me going in the most pessimistic moments during my PhD. This thesis would not have been possible without him, but even then, it reflects only a small part of what I have learned from him. The larger part this knowledge is something that guide me for the rest of my life.

Special thanks to Dr. John E. Pandolfino and Dr. Peter J. Kahrilas for their continual guidance and support throughout the duration of my PhD. Coming from a background in Engineering, I had very little exposure to Biology. I am deeply grateful to Dr. Pandolfino and Dr. Kahrilas for bearing with all my foolish questions on esophageal physiology and patho-physiology.

I would like to thank all my dissertation committee members Prof. Gregory Wagner, Dr. John Pandolfino, Dr. Peter Kahrilas, and Prof. Neelesh Patankar for their time

and consideration. Their support and assurance have been very encouraging for me to complete my PhD thesis.

I acknowledge the support provided by Public Health Service Grants R01-DK079902 and P01-DK117824, and National Science Foundation Grants OAC 1450374 and OAC 1931372 in the completion of this work. I also acknowledge the computational resources provided by Northwestern University's Quest High Performance Computing Cluster. I have also utilized the Extreme Science and Engineering Discovery Environment (XSEDE) cluster Comet, at the San Diego Supercomputer Center through allocation TG-ASC170023, which is supported by National Science Foundation grant number ACI-1548562. I am very grateful for the Terminal Year Fellowship during the 2022-23 academic year funded by the Damoder Pati and Soumitri Pati Reddy Graduate Fellowship at McCormick.

I thank all my labmates, Nishant, Brennen, Shashank, Tom, Guy and Xinyi, for creating such a wonderful lab environment to work in. I am especially grateful to Shashank for helping during the early days of my PhD and for spending countless hours discussing various topics in esophageal mechanics. Tom's cheerful attitude towards research has been a source of constant encouragement for me. I will always cherish our conversations during our walks to get coffee (although he never actually got coffee, he just liked to walk). They were some of the essential breaks from work and learn about each other's research. Special thanks to Jun Yamasaki for lending a helping hand in my research which helped me complete a few projects much faster than I could had been able to on my own. His focus and drive in research has also been a huge encouragement.

I would like to thank some of the closest friends that I have made during my PhD, Prithvijit, Nibir, Aritra, and Aileen. Their accompaniment made the lock-down during

Covid-19 global pandemic bearable. I would also like to give special thanks to Jasmine for her constant encouragement and support during my PhD. Her presence in my life made a huge impact on my emotional well-being and attitude towards research. I would also like to thank my pastor, Deanna, for her thoughtful guidance and spiritual mentorship. Lots of thanks to Jason, Sam, Benjamin, Cindy, Aaron, Steve, and Maddy, for their genuine love and care which has been a huge emotional support for me.

This acknowledgment would not be complete without talking about my parents. It has been their dream that I get a good education. Being a poor family in India, this was not a simple dream. They had to undergo a tremendous amount of sacrifices for a really long time. The few moments of joy in their life have always been through my academic achievements. They have borne all the harsh burdens so that I would not have to bear them. They have made my dreams their own and always encouraged in the pursuits of my dreams. As I write this thesis and look ahead to the completion of my PhD, I feel a sense of achievement. But this feeling sprouts not from the reality of finishing this long journey, but from their smiles.

Dedication

To my parents

Table of Contents

List of Tables

List of Figures

CHAPTER 1

Introduction

The esophagus is a multi-layered muscular tube that transports food from the pharynx to the stomach with the help of neurally activated peristaltic contractions. Esophageal disorders can cause disruption of the process of swallowing, and a variety of symptoms including dysphagia, chest pain, and heartburn. Some of these disorders are gastroesophageal reflux disease (GERD), achalasia and eosinophilic esophagitis (EoE). There is a high worldwide prevalence of esophageal diseases exemplified by studies [**1, 2**] reporting that gastro-esophageal reflux disease (GERD) has a prevalence of $18.1\% - 27.8\%$ in North America alone with an increase across all age groups. Another study [**3**] reported that dysphagia (swallowing difficulty) affects 1 in 25 adults annually in the United States. Hence, it is necessary to understand the underlying causes of the various esophageal diseases for better treatment practices. In addition, there is a also a need for more quantitative approaches for diagnosing esophageal diseases to increase the precision of current diagnostic techniques. This thesis aims to provide a novel direction (and a few steps in that direction) towards esophageal diagnosis and treatment planning using mechanics.

The effects of various esophageal diseases are manifested in different scales ranging from cellular to organ level. For example, EoE exhibits cellular structural changes in the mucosal layer (inner-most layer) as well as increase the overall stiffness and appearance of the tissue at macroscopic tissue level. Esophageal motility disorders such as achalasia display abnormal/absent contractions of the esophageal wall and unrelaxed lower

esophageal sphincter (LES) tone due to abnormal muscles activation. Irrespective of the scale at which the disorders originate, the final stage at which they are manifested (through dysphagic symptoms) is the macroscopic tissue/organ scale. This is because the primary function of the esophagus is to physically transport the swallowed bolus and empty it into the stomach. Thus, any form of dysphagia is directly related to the this transport and emptying process to varying extent. This is why some of the most popular diagnostic technologies such as high resolution manometry (HRM), functional lumen imaging probe (FLIP), barium esophagram and endoscopy test the state and function of the esophagus at this scale. Mechanics plays a very dominant and crucial role at this scale of esophageal function since the transport of any swallowed bolus and the deformation of the esophageal walls must follow the physical laws of mass and momentum conservation. Thus, any esophageal disorder that manifests itself at the tissue level must also reveal its unique characteristic through mechanics-based parameters such as the esophageal wall material properties and active stretches in the muscle fibers due to neural activation. Hence, understanding the biomechanics of esophageal transport can provide important insights into the nature of these disorders as well as the physiology of esophageal functioning. Our main research involves the bio-physiologic modeling of the esophagus using mechanics and deep learning, and can be categorized into three focus areas: fundamental research, patient-specific analysis and virtual disease landscape (VDL) as shown by the pictorial description in Figure 1.1.

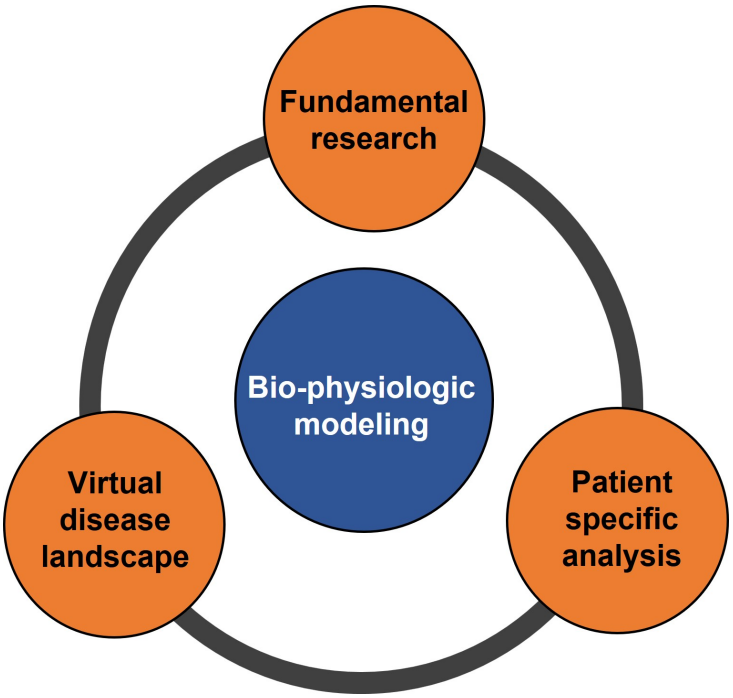

Figure 1.1. Main focus areas of this thesis.

1.1. Fundamental research: vEsophagus

The main goal of this focus area is to develop a fully-resolved model of the esophagus [**4, 5**] to describe various mechanics based physiological processes involved in the functioning of the esophagus and the pathophysiology of various esophageal disorders that can be explained using mechanics. This model forms the basis of applying well-established knowledge of the anatomical components of the esophagus such as the fiber architecture of the wall muscles, orientation of the different layers, and the activation of the muscle fibers, to understand their relative imapct on verious esophageal diseases. Using the vEsophagus, we have performed simulations to identify the factors that play a major role in the formation an esophageal disorder called blown-out myotomy (BOM) or pseudodiverticulum, which often accompanies an esophageal surgery called myotomy used to treat

patients suffering from achalasia as described in chapter 2. This might be helpful in guiding and establishing myotomy procedures that would reduce the risk of the formation of an esophageal BOM.

1.2. Patient-specific analysis: FluoroMech and MRI-MECH

Some of the common tests for diagnosing esophageal disorders are barium esophagram using fluoroscopy, high resolution manometry (HRM) [**6, 7, 8, 9, 10**], and functional lumen imaging probe (FLIP) [**11, 12**]. An esophagram is non-invasive test wherein a patient swallows a radiopaque material, usually dilute barium, and fluoroscopic imaging is used to visualize the esophageal lumen. HRM and FLIP are more invasive procedures where a catheter with sensors is inserted into the esophagus to quantitatively assess the esophageal contractility. Measurements made by HRM and FLIP are physical quantities such as the pressure developed within the esophagus when a fluid is swallowed and/or the cross-sectional area variation along the esophageal length. These physical quantities serve as surrogates for fundamental physiomarkers such as tissue integrity and neuromuscular function that define the health of an organ. In fact, since the fundamental physiomarkers are often unknown or unmeasurable, clinical decisions often need to be based on these physical quantities. However, such measurements never precisely track the relevant physiomarkers and this can lead to discrepancies. For example, the widely used Chicago Classification v4.0 (CCv4.0) [**13**] classifies esophageal disorders based on a set of parameters derived from pressure measurements made with HRM. Since luminal pressure and cross-sectional area, which occur at a tissue level, are the physical quantities commonly measured by HRM, FLIP, or esophagram, the first stage of quantifying the fundamental

physiomarkers of esophageal function are at the tissue level. In this context, the mechanical properties of the esophageal wall as well as its dynamic behavior related to active contraction and relaxation could be important physiomarkers. Thus, mechanics-based analysis provide valuable mechanistic insight regarding esophageal function.

Previous mechanics-based studies on the esophagus have been done both experimentally and computationally. Experimental studies [**14, 15, 16, 17, 18**] focused on the mechanical properties of the esophageal walls in-vitro. In-silico modeling of the esophagus have been performed both in the context of pure fluid mechanics [**19, 20, 21, 22, 23**] to understand the nature of bolus transport as well as fully resolved fluid-structure interaction models to understand how the esophageal muscle architecture influences esophageal transport as well as the stresses developed in the esophageal walls during bolus transport [**4, 5**]. The continuum mechanics based fully-resolved model discussed above explains some very fundamental behavior of esophageal transport, but suffers from two major drawbacks: 1) its works on a simple cylindrical model with well-defined structured behavior and material properties, and fails to capture the variability observed in reality, and 2) it takes a long time to run each simulation, and therefore, is not feasible to apply in patient-specific scenarios. For patient-specific analysis of esophageal transport, we have developed two models: 1) **FluoroMech** and 2) **MRI-MECH** that can process physiologic data from patients, and predict the state and functioning of the esophagus. These models read radiographic images from fluoroscopy and MRI, and transform them using deep learning so that they can be used by mechanics-based models to predict potential physio-markers. Therefore, these models bridge the gap between clinical observations

and mechanics based analysis. FluoroMech and MRI-MECH are described in detail in chapters 3 and 4, respectively.

1.3. Virtual disease landscape

The hybrid models, FluoroMech and MRI-MECH, can estimate the state and function of the esophagus through a set of mechanics-based parameters. We have developed another hybrid framework called mechanics-informed variational autoencoder (MI-VAE) that uses these mechanics-based parameters to identify the underlying physics of various esophageal disorders (motility disorders, eosinophilic esophagitis, reflux disease, scleroderma esophagus) and maps them onto a parameter space which we call the virtual disease landscape (VDL). A modified version of FluoroMech processes the output from the functional lumen imaging probe (FLIP) to estimate the mechanical "health" of the esophagus by predicting a set of mechanics-based parameters such as esophageal wall stiffness, muscle contraction pattern and active relaxation of esophageal walls. The mechanics-based parameters were then used to train a variational autoencoder that generated a latent space. The latent vectors along with a set of discrete mechanics-based parameters define the VDL and formed clusters corresponding to specific esophageal disorders. The VDL not only distinguishes among disorders but also displayed disease progression over time. Finally, we demonstrated the clinical applicability of this framework for estimating the effectiveness of a treatment and tracking patients' condition after a treatment. MI-VAE is descrived in detail on chapter 5.

CHAPTER 2

Myotomy technique and esophageal contractility impact blown-out myotomy formation in achalasia: an in-silico investigation

Achalasia is an esophageal motility disorder characterized by impaired esophagogastric junction (EGJ) relaxation and absent peristalsis. The Chicago Classification [**24, 13**] categorizes achalasia into subtypes I, II and III based on pressure topography patterns observed with high resolution manometry (HRM). A recent study [**25**] showed that the incidence and prevalence of achalasia diagnosed using high resolution manometry is at least 2- to 3-fold greater than previous estimates with an incidence in the range of 2-3/100,000 and a steadily rising prevalence as newly diagnosed cases accumulate. The standard surgical treatment of achalasia is laparoscopic Heller myotomy (LHM) during which the circular muscle fibers of the distal esophagus and lower esophageal sphincter (LES) are disrupted. Figure 2.1 (A) shows three sequential time points during a LHM procedure. The myotomy extends for a variable length onto the distal esophagus and gastric cardia [**26**]. Because myotomy can lead to uncontrolled reflux, it is usually combined with a partial fundoplication [**27**], wherein the gastric fundus is mobilized and partially wrapped around the LES to reduce the severity of post-procedure reflux.

Another potential complication of myotomy is the formation of a blown out myotomy (BOM) in the distal esophagus [**28, 29**]. A BOM is a pseudodiverticulum in the distal

esophagus that can progressively enlarge and compromise esophageal emptying, potentially mandating further surgery (Figure 2.1(B)). BOM is characterized by an outward protrusion of the mucosa through the defect in the muscle layers resultant from the myotomy. BOM formation can be attributed to a complex combination of physical and biological factors such as strength of the esophageal wall after myotomy, elastic and plastic behavior of the esophagus wall, remodeling and neural-activated peristaltic contraction strength. In this work, we investigated the underlying physics potentially leading to the formation of BOM using a fully coupled three-dimensional in-silico model called virtual esophagus (vEsophagus). A previous study using a computational model of the esophagus analyzed the effect of anatomical asymmetry, tissue anisotropy, and the LES in the formation of epiphrenic diverticula [**30**]. We used a similar model to understand the impact of the dimensions of myotomy in the formation of BOMs. Furthermore, although myotomy obliterates the LES, there is some residual tone at the esophagogastric junction (EGJ) attributable to the crural diaphragm, the remains of the esophageal wall at the myotomy site, and the associated partial fundoplication. The impact of this collective tone at the EGJ in the formation of BOM was also investigated and described in the following sections.

2.1. vEsophagus: In-silico model of the esophagus

The vEsophagus was modeled as a multilayered axisymmetric cylindrical tube as shown in Figure 2.1(C). It is a computational model that captures the fluid-structure interaction between the esophageal walls and the swallowed bolus using the immersed

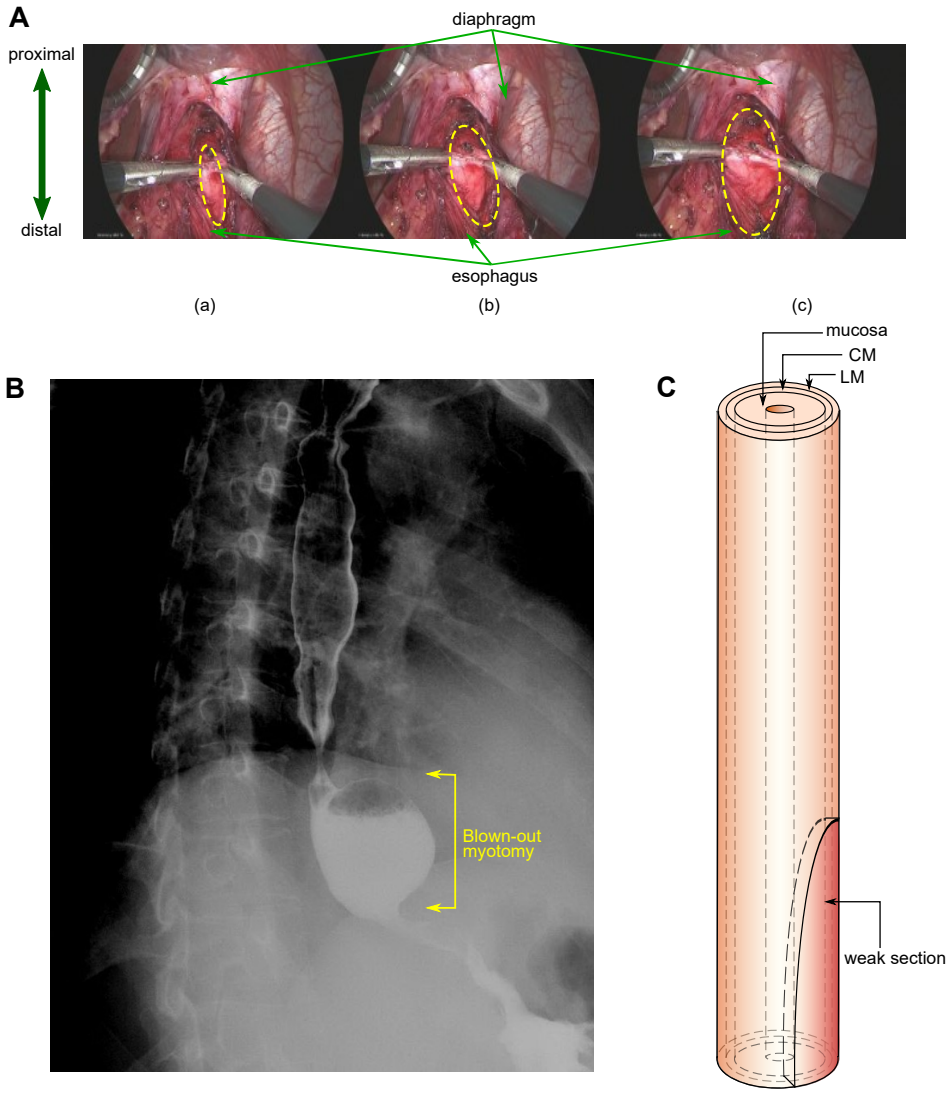

Figure 2.1. A) Laparoscopic Heller Myotomy. The top of the figures shows the diaphragmatic crus arcing over the esophagus. Figures (a) – (c) show three times during the myotomy. The dashed yellow ellipses show the enlarging area of bared mucosa with progression of the myotomy. (B) Esophagram of a blown out myotomy (BOM). Barium is retained inside the pseudodiverticulum, almost filling it. (C) vEsophagus model used in our simulations with 3 layers: LM, CM and mucosa. The weakened region from the myotomy is shown as an ellipse at the distal end.

boundary (IB). This model was based on a previous work [**5**] and the mathematical details of the IB method are provided in the Appendix A. Due to the use of IB method, the vEsophagus wall has a viscoelastic nature, which is also observed in reality [**31, 32**].

The dimensions of the vEsophagus were based on a typical LHM video, a few instants of which are shown in Figure 2.1(A). The maximum extension of the opened grasper is 2 cm. Using that as a scale, we estimated the average outer diameter of the collapsed esophagus to be 1.6 cm. The vEsophagus wall was composed of three main layers: mucosa (which includes both mucosa and submucosa), circular muscle (CM), and longitudinal muscles (LM). The approximate thickness of each layer was estimated experimentally in a previous study [**33**]. Using the same relative ratios of the layers, we calculated the CM and LM thickness to be approximately 1 mm each and mucosal thickness to be 5.5 mm. For our simulations, we assumed the total length of the esophagus including the upper esophageal sphincter (UES) and LES to be 24 cm. The UES and LES were assumed 3 cm each. The UES opens for a brief interval during a swallow to allow bolus entry into the esophagus and then closes for the duration of the sequence [**34, 35**]. Hence, in our simulations we eliminated the UES by assuming the proximal end of the vEsophagus to be fixed and only considered the esophagus distal to the UES.

2.1.1. Esophageal wall material properties

The wall of the vEsophagus was modeled as a composite of hyperelastic materials with each layer composed of fibers embedded in a matrix [**16, 36**]. The hyperelastic behavior of the vEsophagus wall layers was defined in other in-silico models [**5, 37, 38, 15**] and

discussed below. The material model used for the mucosal layer is as follows:

$$\psi^{\text{mucosa}} = \psi^{\text{mucosa}}_{\text{matrix}} + \psi^{\text{mucosa}}_{\text{fiber}}, \tag{2.1}$$

$$\psi^{\text{mucosa}}_{\text{matrix}} = \frac{C_o}{2}\left(I_1 - 1\right), \tag{2.2}$$

$$\psi^{\text{mucosa}}_{\text{fiber}} = \frac{C_1}{2}\left(\sqrt{I_4^{\text{mucosa}}} - 1\right)^2, \tag{2.3}$$

where $I_1 = \text{tr}(\mathbb{C})$, $I_4^{mucosa} = \mathbb{C} : (\boldsymbol{a}^{\text{mucosa}} \otimes \boldsymbol{a}^{\text{mucosa}})$, and $\boldsymbol{a}^{\text{mucosa}}$ is the unit vector along the axial direction. ψ^{mucosa}, $\psi^{\text{mucosa}}_{\text{matrix}}$, and $\psi^{\text{mucosa}}_{\text{fiber}}$ are the total, matrix, and fiber strain energy function of the mucosa, respectively. The matrix is modeled as a Neo-Hookean material, and the fibers are modelled as a bilinear model. $\mathbb{C}$ is the right Cauchy-Green tensor. In this model, $C_o = 0.004$ kPa and $C_1 = 0.04$ kPa. The material model used for the muscle layers are as follows:

$$\psi^{\text{muscle}} = \psi^{\text{muscle}}_{\text{muscle}} + \psi^{\text{muscle}}_{\text{fiber}}, \tag{2.4}$$

$$\psi^{\text{muscle}}_{\text{matrix}} = \frac{C_2}{2}\left(I_1 - 1\right), \tag{2.5}$$

$$\psi^{\text{muscle}}_{\text{fiber}} = \frac{C_3}{2}\left(\frac{\sqrt{I_4^{\text{muscle}}}}{\lambda} - 1\right)^2, \tag{2.6}$$

where $I_4^{muscle} = \mathbb{C} : (\boldsymbol{a}^{\text{muscle}} \otimes \boldsymbol{a}^{\text{muscle}})$, and $\boldsymbol{a}^{\text{muscle}}$ unit vector along the circumferential and axial direction for circular muscles (CM) and longitudinal muscles (LM), respectively. ψ^{muscle}, $\psi^{\text{muscle}}_{\text{matrix}}$, and $\psi^{\text{muscle}}_{\text{fiber}}$ are the total, matrix, and fiber strain energy function of the muscle layers, respectively. The parameter λ induces a contraction in the muscle fibers when $\lambda < 1$. λ lies between 0 and 1, with a smaller value indicating a tighter contraction. The CM and LM are significantly stiffer than the mucosal layer. In this model, $C_2 = 0.4$

kPa and $C_3 = 40$ kPa. Although we used the same strength for the longitudinal and circular muscles fibers (C_3), the net strength of each muscle layer depends on both the strength of the fibers and their orientation (as specified by $\boldsymbol{a}^{\text{muscle}}$).

2.1.2. Contraction patterns

Based on the contractile behavior of the esophagus, it is possible to distinguish different esophageal motility disorders. A normal subject exhibits normal peristalsis. Type I achalasia patients do not show any prominent contractile behavior. Type II achalasia patients experience pan-esophageal pressurization. Type III achalasia patients have a huge variability in the contraction pattern, but typically they exhibit a combination of peristalsis in the proximal esophagus and spasm in the distal esophagus. In order simulations, the contraction is implemented by specifying λ. The mathematical details of the different contraction patterns discussed in the three simulation sets are described below.

2.1.2.1. Peristaltic contraction.

$$\lambda_{\text{peristalsis}} = \begin{cases} 1 & \text{for} \quad t \leq \frac{L-z}{c}, \\ 1 - \lambda_o e^{-0.5(z-ct)^2/w^2} & \text{for} \quad \frac{L-z}{c} < t < \frac{L-z}{c} + \frac{\Delta L}{c} \\ 1 & \text{for} \quad t \geq \frac{L-z}{c} < t < \frac{L-z}{c} + \frac{\Delta L}{c}, \end{cases} \tag{2.7}$$

wherein $z = 0$ at the distal end of the esophagus and $z = L$ at the proximal end, L is the length of the esophagus, c is the speed of the peristaltic contraction, ΔL is the length of the contracting segment, λ_o is the amplitude of the activation parameter, and w is a parameter that specifies the width of the Gaussian function that controls the nature of

the contraction. In our simulations, we used $\lambda_o = 0.4$, $c = 200$ mm/s, $\Delta L = 60$ mm, and $w = 15$ mm.

2.1.2.2. Panesophageal pressurization.

(2.8)

$$\lambda_{\text{panesophageal}} = \begin{cases} 1 & \text{for} \quad Z < 0, \\ 1 - \gamma(t)\lambda_o \left[1 - \cos\left(\frac{2\pi Z}{l_1}\right)\right] & \text{for} \quad 0 < Z < \frac{l_1}{2}, \\ 1 - 2\gamma(t)\lambda_o & \text{for} \quad \frac{l_1}{2} \leq Z < \frac{l_1}{2} + l_2, \\ 1 - \gamma(t)\lambda_o \left[1 - \cos\left(\frac{2\pi\left(Z - \frac{l_1}{2} - l_2\right)}{l_2}\right)\right] & \text{for} \quad \frac{l_1}{2} + l_2 \leq Z < \frac{l_1}{2} + l_2 + \frac{l_3}{2}, \\ 1 & \text{for} \quad Z \geq \frac{l_1}{2} + l_2 + \frac{l_3}{2}, \end{cases}$$

wherein $Z = L - z$, $0 < \gamma(t) < 1$ is the parameter that determines the speed at which the pressurization occurs. l_1 and l_3 are the length segments at the proximal and distal ends of the esophagus where the maximal amplitude of the contraction strength reduces to zero at the two ends. l_2 is the length segment at the center of the esophagus where the maximum pressurization acts. λ_o is the amplitude of the contraction, and in our simulations, we used $\lambda_o = 0.85$.

2.1.2.3. Proximal peristalsis with distal spasm. To implement this contraction, we enforce $\lambda_{\text{peristal}}$ to the proximal half of the esophagus with a reduction in strength at the transition between the proximal and distal portions of the esophagus. In the distal half of the esophagus, the value of λ is specified as follows:

(2.9)
$$\lambda_{\text{spasm}} = \alpha\lambda_{\text{panesophageal}}$$

wherein $\alpha = \frac{1}{4}\left[3 + \sin\left(\frac{2n\pi z_d}{L_d}\right)\right]$, L_d is the length of the distal half of the esophagus, z_d is the coordinate along the length of the esophagus starting from the middle of the esophagus to its distal end, and n is the number of high spastic zones. In our simulations, we have used $n = 3$. The maximum amplitude of spasm in the distal esophagus was $\lambda_o = 0.75$.

2.2. Simulation details

We performed three sets of simulations to investigate the effect of myotomy on the pressure stresses that can potentially lead to the formation of a BOM. First, we did a parametric study with 5 cases with different myotomy dimensions, specifically the length and width of the weakened section. Table 2.1 shows the details of different cases simulated. In all cases, we assumed the extreme case wherein the LES remained occluded. This helped to quantify the effect of myotomy as a set of baseline cases that were not influenced by other physiological factors. Since we assumed the EGJ to be fully occluded in these first simulations, we eliminated the LES in the vEsophagus, leaving 18 cm of esophagus between the UES and LES, fixed at both ends. The lengths of the myotomies specified in Table 2.1 are considered from the proximal end of the LES. Thus, the total lengths of the myotomies were 3 cm more than shown in Table 2.1. The contraction pattern was kept the same for all 5 cases (pan-esophageal pressurization) for comparison.

Second, we investigated the effect of four different physiologically motivated esophageal muscle contraction patterns that can potentially lead to the formation of a BOM: normal peristalsis, minimal/no contraction as observed in achalasia type I, pan-esophageal contraction as observed in achalasia type II, and peristalsis transitioned into distal spasm

Table 2.1. Dimensions of the elliptical LHM section in simulation set 1

Case number	**1/2 Major axis**	**Minor axis**
1	60.0 mm	7.0 mm
2	90.0 mm	7.0 mm
3	30.0 mm	7.0 mm
4	60.0 mm	4.0 mm
5	60.0 mm	10.0 mm

i.e., spasm in the distal half of the esophagus which predominantly contains smooth muscles, as observed in achalasia type III. These contraction patterns are neurally controlled manifest by the circumferential contraction of the CM and the longitudinal shortening of the LM [**39, 40**]. The details of these cases are given in Table 2.2. All these cases model EGJ outflow obstruction (EGJOO) by a closed distal end. We performed two sets of this simulation, one with the standard reference length of 6, and the other with a short myotomy length of 2 cm to describe the difference in outcome of myotomy length.

Third, we investigated the effect of EGJ tone and remnant musculature at the myotomy site on pressure stresses that can potentially lead to the formation of a BOM by considering two groups with six cases for group I and one case of group II as detailed in Table 2.3. Since the LES is obliterated by the myotomy, the EGJ tone can be contributed to external anatomical features such as the hiatus as well as a fundoplication. This EGJ tone was modeled as increased stiffness at a short section of the distal esophagus. This is reasonable as the effective impact of the EGJ tone in HRM and FLIP appears as a region of higher stiffness by providing more resistance to opening compared to the remainder of the esophagus. Although the muscle fibers are damaged at the myotomy site, the wall stiffness at that site might not necessarily be equal to the strength of the mucosa. This is

Table 2.2. Contraction types for simulation set 2

Case number	**Contraction type**	**Details**
1	Peristalsis (Normal), standard myotomy	Contraction width: 6 cm, speed: 2 cm/s, EGJOO, Myotomy length: 6 cm
2	Very weak contraction (Achalasia I), standard myotomy	Stationary over the entire esophageal length, EGJOO, Myotomy length: 6 cm
3	Pan-esophageal contraction (Achalasia II), standard myotomy	Stationary over the entire esophageal length with weak irregularities in strength along the length, EGJOO, Myotomy length: 6 cm
4	Proximal peristalsis transitions with distal spasm (Achalasia III), standard myotomy	Peristalsis in the proximal half of the esophagus that merges with spasm (3 stationary peaks) in the distal half, EGJOO, Myotomy length: 6 cm
5	Peristalsis (Normal), short myotomy	Contraction width: 6 cm, speed: 2 cm/s, EGJOO, Myotomy length: 2 cm
6	Very weak contraction (Achalasia I), short myotomy	Stationary over the entire esophageal length, EGJOO, Myotomy length: 2 cm
7	Pan-esophageal contraction (Achalasia II), short myotomy	Stationary over the entire esophageal length with weak irregularities in strength along the length, EGJOO, Myotomy length: 2 cm
8	Proximal peristalsis transitions with distal spasm (Achalasia III), short myotomy	Peristalsis in the proximal half of the esophagus that merges with spasm (3 stationary peaks) in the distal half, EGJOO, Myotomy length: 2 cm

because some remnant muscle fibers might be present after myotomy. Additionally, the myotomy site might heal or scar to some extent with time, which can raise the stiffness of the wall at the myotomy site. The total length of the esophagus in these cases was 21 cm since the LES was included and the lower end of the esophagus was free to move.

Table 2.3. Details of simulation set 3

Group I	
Case number	**Details**
1	Standard myotomy length (6 cm); no EGJ tone; myotomy affected zone walled by mucosa only; contraction type: normal peristalsis
2	Standard myotomy length (6 cm); with an EGJ tone; myotomy affected zone walled by mucosa only; contraction type: normal peristalsis
3	Standard myotomy length (6 cm); with an EGJ tone; myotomy affected zone walled by mucosa as well as weakened muscle layers (the strength of the muscle fibers were reduced by 99% but the matrix of the muscle layers were intact at the myotomy site); contraction type: normal peristalsis
4	Short myotomy length (3 cm); no EGJ tone; myotomy affected zone walled by mucosa only; contraction type: normal peristalsis
5	Short myotomy length (3 cm); with an EGJ tone; myotomy affected zone walled by mucosa only; contraction type: normal peristalsis
6	Short myotomy length (3 cm); with an EGJ tone; myotomy affected zone walled by mucosa as well as weakened muscle layers (the strength of the muscle fibers were reduced by 99% but the matrix of the muscle layers were intact at the myotomy site); contraction type: normal peristalsis
Group II	
POEM length: 12 cm; LM intact at the myotomy site while CM fibers were broken, and CM matrix strength reduced 100-fold; with an EGJ tone; contraction type: normal peristalsis	

In reality, the factors discussed above (myotomy dimensions, contraction pattern, and EGJ tone) work together making it impossible to investigate their individual impact. The

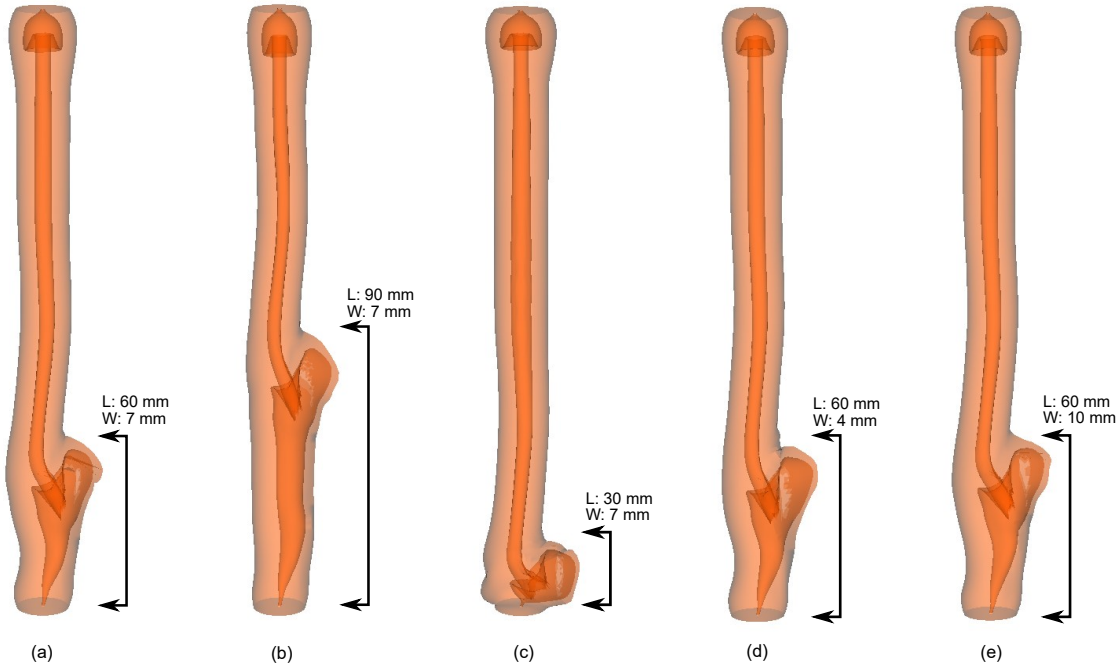

Figure 2.2. Panel (a): Length 60 mm, max width 7 mm; Panel (b): Length 90 mm, max width 7 mm; Panel (c): Length 30 mm, max width 7 mm; Panel (d): Length 60 mm, max width 4 mm; Panel (e): Length 60 mm, max width 10 mm; Panels (a) – (e) shows the deformed shape of the esophagus for cases 1 – 5, respectively at the same time instant.

simulation sets described above addresses this problem by systematically investigating the impact of varying each factor independently while holding the others constant. The numerical simulations were performed using the immersed boundary method adaptive mesh refinement (IBAMR) software infrastructure [**41**]. For post-processing and visualization of the simulation results, we used an open-source visualization software VisIt [**42**].

2.3. Simulation set 1: parametric study of the effect of myotomy with fully occluded EGJ

The deformation of the esophagus during bolus transport for the cases detailed in Table 1 is shown in Figure 2.2 for the same time instant. Case 1 used the dimensions of the weakened section estimated from the LHM video as shown by Figure 2.1(A) and is the used as a reference for comparison with the other cases. Physiologically, the conditions for this simulation set are similar to an incomplete myotomy or tight fundoplication performed on a Type II achalasia patient. Cases 1, 2, and 3 had a maximum outward displacement at the myotomy site of 9.5 mm, 9.2 mm, and 9.3 mm, respectively. Thus, although both increasing and decreasing the length of myotomy from the reference case 1, reduced the degree of deformation, the difference in the magnitude of maximum outward displacement was minimal. The percentage volume of fluid accumulated in the myotomy affect region with respect to the total bolus volume for cases 1, 2, and 3 were found to be 48.6%, 67.6%, and 28.7%, respectively. Thus, the volume of fluid that accumulated inside the myotomy was proportional to the length of myotomy. Cases 1, 4 and 5 had varying minor axes and the maximum displacements were 9.5 mm, 9.6 mm, and 9.7 mm, respectively. Like the cases with varied myotomy length, the differences were minimal. The percentage volume of fluid accumulated in the myotomy affect region with respect to the total bolus volume for cases 1, 4, and 5 were found to be 48.6%, 48.8%, and 48.4%, respectively. Thus, the volume of fluid which accumulated inside the myotomy site was also very similar as can be seen in Figure 2.2.

2.4. Simulation set 2: effect of muscle contraction

The maximal deformation at the myotomy site associated with the four different patterns of esophageal contraction detailed in Table 2 are shown in Figure 2.3. The maximum outward displacement at the standard myotomy site for cases 1-4 were found to be 18.0 mm, 0.4 mm, 5.9 mm, and 7.4 mm, respectively. The percentage volume of fluid accumulated at the myotomy affected regions with respect to the total bolus volume for these cases were 95.1%, 29.9%, 46.5%, and 81.7%, respectively. The maximum outward displacement at the short myotomy site for cases 5-8 are 9.4 mm, 0.4 mm, 7.5 mm, and 12.8 mm, respectively. The percentage volume of fluid accumulated at the short myotomy affected regions with respect to the total bolus volume for cases 5 - 8 were 87.7%, 0.33%, 16.2%, and 57.2%, respectively. Thus, the volume of fluid accumulated at the myotomy site for short myotomy was less compared to that for a longer myotomy. On comparing these cases, we observed that the maximum outward displacement at the myotomy occurred with normal peristalsis. Additionally, the peristaltic contraction passed over the weakened section without collapsing the outward protrusion, but rather, increased its outward displacement, and aided the deformation at the myotomy site as shown in Figure 2.3A (a) and 3B (a). No prominent deformation at the myotomy site was observed for cases 2 and 6. The pan-esophageal pressurization of cases 3 and 7 does not lead to efficient transport of the bolus from the proximal to the distal esophagus as evident by the remnant fluid at the proximal esophagus. The BOMs formed in these cases had lesser volumes compared to cases 1, 4, 5, and case 8. Cases 4 and 8 shows that proximal normal peristalsis which transitioned into distal spasms resulted in volumes accumulated at the myotomy site less than case 1 and 4, but greater than the other cases. The effect

of distal spasm in shorter myotomy was more prominent compared to that observed for longer myotomy as observed by comparing the shape of the bolus in Figure 2.3A (d) and fig-sim2B (d). Due to the lack of contractions, there was no prominent deformation at the myotomy site for case 6 just like case 2.

2.5. Simulation set 3 (Group I): effect of EGJ tone and musculature at the myotomy site

The effect of varied EGJ tone and remnant muscle fibers at the myotomy site on deformation at the myotomy affected zone was investigated by comparing 6 cases as detailed in Table 3. Figure 2.4 shows bolus transport through an esophagus with a standard size myotomy (panels a-c), and with a short myotomy (panels d-f). Comparing cases 1 and 2, we see that without EGJ tone the peristaltic contraction successfully emptied the esophagus in case 1, but due to the presence of the EGJ tone in case 2, a prominent deformation at the myotomy site was observed. But, as we see in Figure 2.4A (c), even with the presence of the EGJ tone, the esophagus with a stronger wall at the myotomy site was able to empty with the help of a peristaltic contraction without a prominent deformation at the myotomy location. Additionally, Figure 2.4B (a)-(c) illustrate the bolus emptying in cases 1 and 3 by the high fluid velocity at the distal end of the esophagus, and the negligible emptying of case 2 by almost no fluid flow at the distal end and the accumulated fluid at the myotomy location. Figures 2.4C (a) and (b) show that the intrabolus pressure reached a higher value for case 2 compared to case 1 and led to a prominent deformation at the myotomy site in case 2. The intrabolus pressure was significantly higher in case 3 compared to cases 1 and 2 but did not lead to large

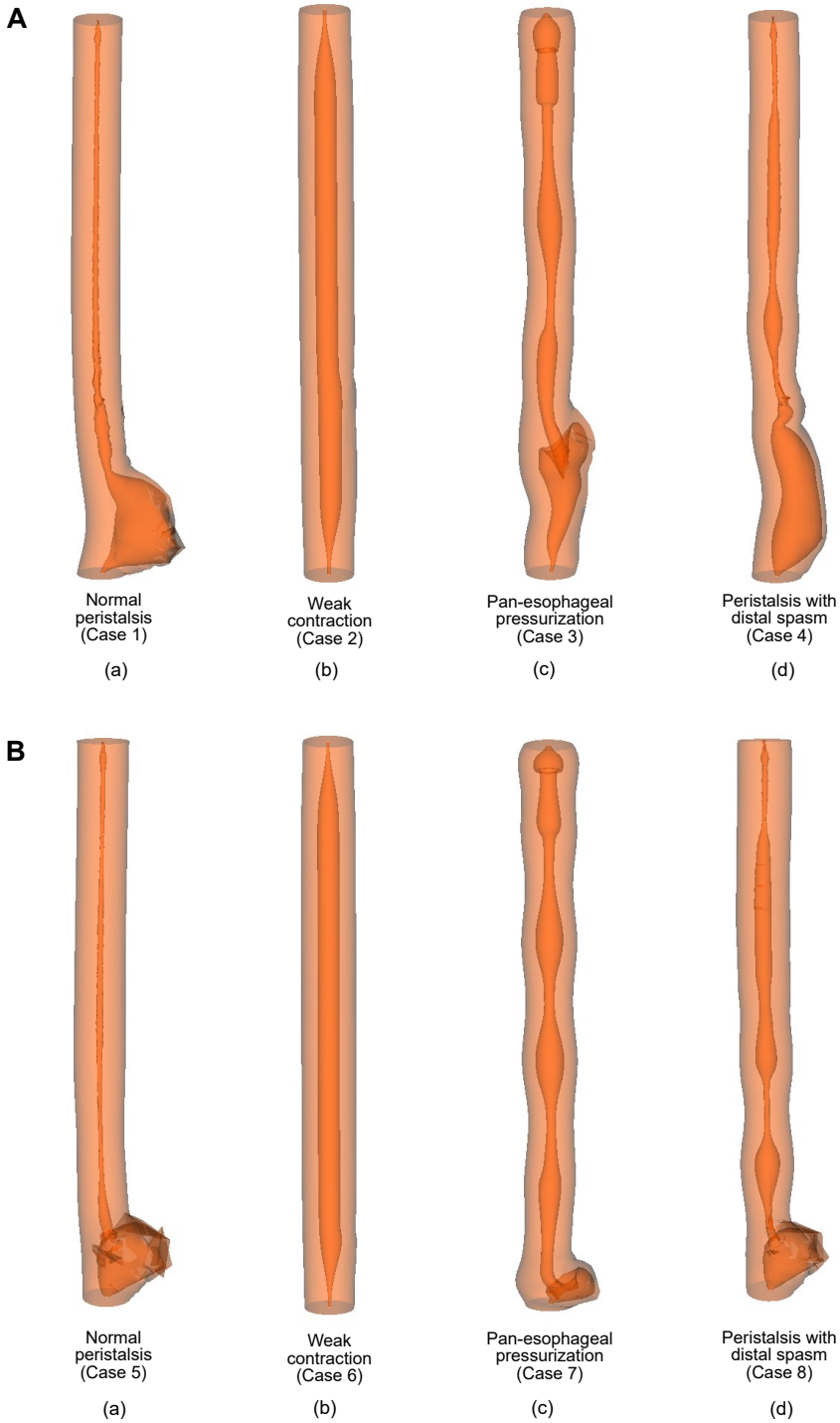

Figure 2.3. Effect of muscle contraction (A) Standard myotomy (= 6 cm). (B) Short myotomy (= 3 cm).

deformation at the myotomy site. Figures 2.4A (d)-(f) show that shorter myotomy length always resulted in adequate emptying. The velocity field at the distal end of the esophagus as shown in Figures 2.4B (d)-(f) demonstrates the emptying process. Additionally, Figures 2.4C (d)-(f) show that the intrabolus pressure in cases 4-6 was higher compared to that observed in cases 1 and 2. As shown in Figure 2.4A, the volume of the bolus accumulated inside the esophagus at the end of the simulation for cases 1 - 6 were 37.9%, 98.1%, 15.0%, 15.9%, 13.3%, and 11.5% of the initial bolus volume, respectively. For the time instant shown in Figure 2.4C, the average intrabolus pressure in case 2 was 33% higher than case 1. Cases 3 - 6 had significantly higher intrabolus pressure compared to cases 1 and 2. We found that the average intrabolus pressure of cases 3 - 6 were 7.3, 7.4, 8.1, and 8.9 times that of case 1, respectively.

2.6. Simulation set 3 (Group II): effect of POEM at the myotomy site

Cases 3 and 6 of group I demonstrated that the esophagus with greater stiffness at the myotomy site compared to the other cases resisted deformation at the myotomy site and aided in bolus emptying. In LHM both CM and LM fibers are obliterated resulting in a very weak esophageal wall at the myotomy site. Peroral endoscopic myotomy (POEM), on the other hand, only obliterates the CM fibers and leaves the LM intact increasing the wall strength at the myotomy site compared to that seen with LHM. Group II simulation investigates the impact of POEM on BOM formation and bolus emptying. Figure 2.5 (a) shows the final configuration of the vEsophagus after bolus transport. The high velocity field at one instant, as shown by Figure 2.5b) describes how the bolus empties out of the esophagus by the peristaltic contraction. The high intrabolus pressure (shown by Figure

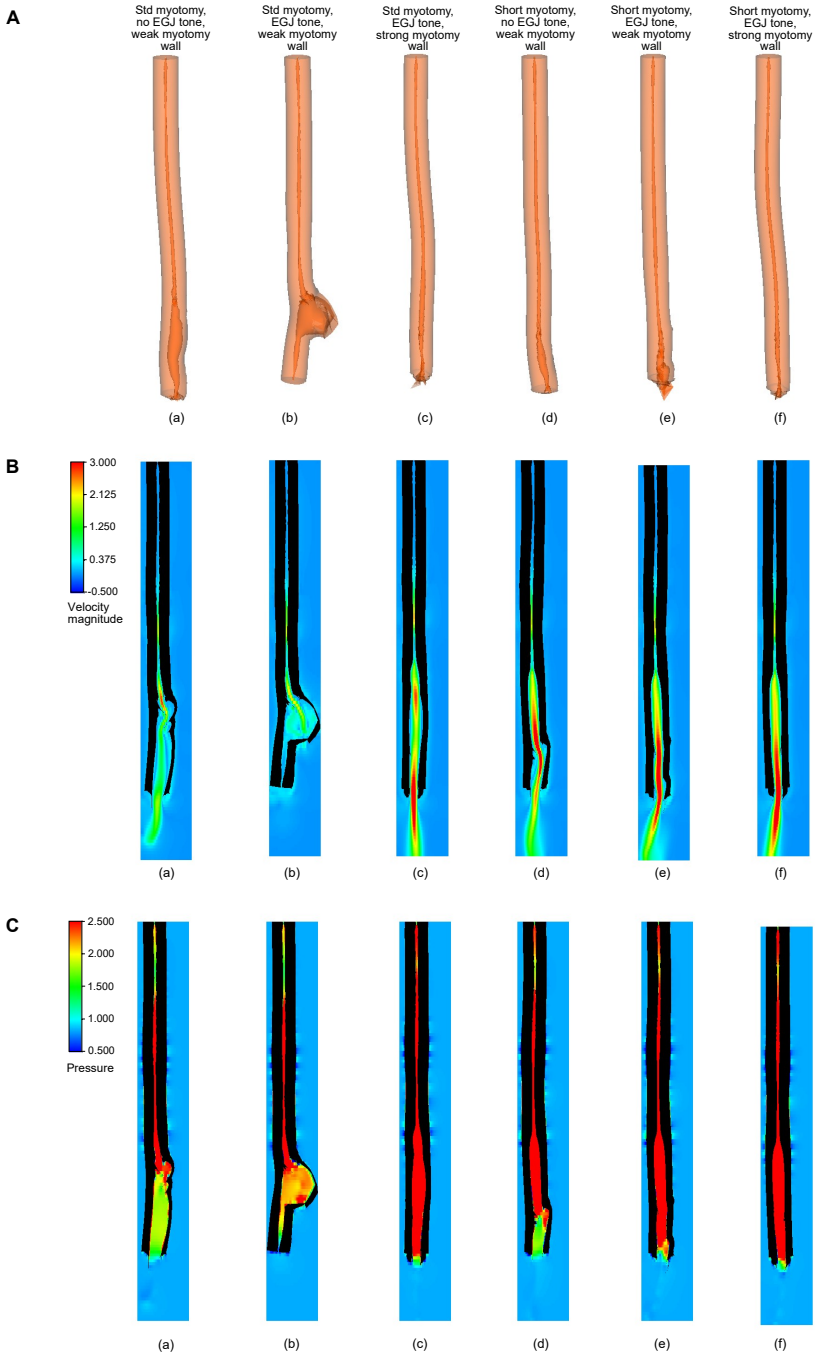

Figure 2.4. (A) Panels (a) – (f) show the myotomy deformation associated with cases 1 - 6, respectively. (B) Non-dimensional velocity distribution within the esophagus with a myotomy at the same time instant. Panels (a) – (f) illustrate cases 1 – 6, respectively. (C) Non-dimensional pressure distribution within the esophagus with a myotomy at the same time instant. Panels (a) – (f) illustrate cases 1 - 6, respectively.

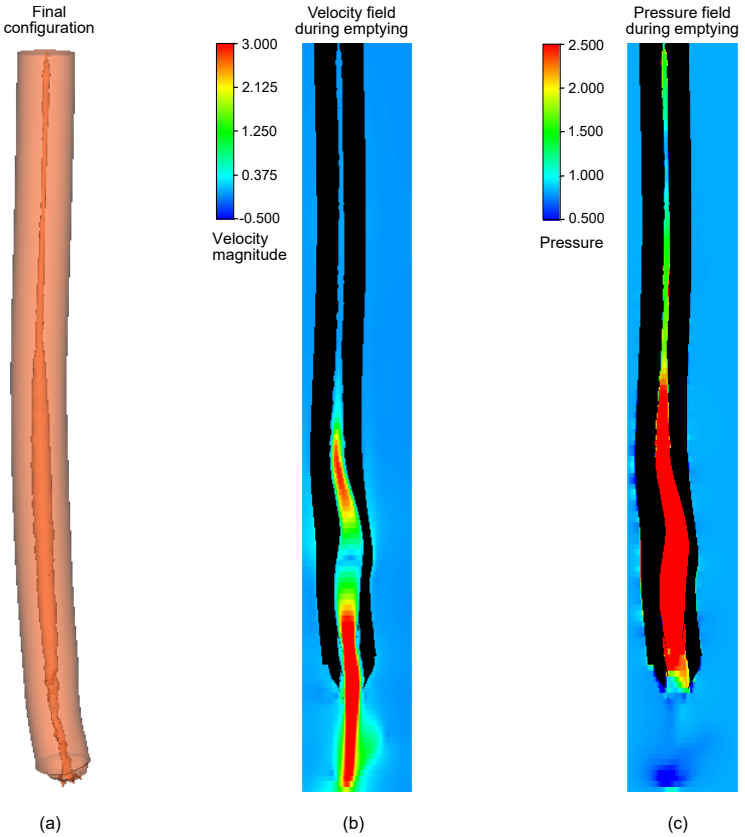

Figure 2.5. Panel (a) shows the final configuration of the esophagus undergone with POEM. No prominent deformation observed at the myotomy site. Panels (b) and (c) show the velocity and pressure fields inside the esophagus at a time instant when the EGJ opens due to the intrabolus pressure, and the bolus empties out of the esophagus. The IBP in this case is 5.3 times that of case 1 of group I (which was used as a reference).

2.5 (c)) drives the fluid out of the esophagus. The intrabolus pressure in this case was 5.3 times higher than that of case 1 of group I (which was used as a reference for the other simulations in simulation set 3).

2.7. Implications and future directions

In practice, only the myotomy length is controlled while the width depends on the myotomy length. In general, a longer myotomy leads to the formation of a wider weak section. Since the effect of width on the volume accumulated inside the deformed myotomy site is negligible, our study validates the current practice of controlling only the length of myotomy to control the formation of a BOM. Identifying the LES during a myotomy procedure can be challenging. Therefore, a longer myotomy might appear to be safer choice to make sure EGJOO is no longer present. Additionally, myotomies are accompanied by fundoplication, which increase the overall EGJ tone. But our simulations show that this combination of long myotomy with a strong EGJ tone possibly due to fundoplication maximizes the risk of BOM formation. Instead, effort should be made to have shorter myotomies focused at the LES and try to avoid fundoplication to minimize the chances of BOM formation. This is consistent with the initial description of BOM [**28**] that showed that BOM was not found in patients undergoing pneumatic dilation (essentially a short myotomy despite not being complete) but occurred frequently in patients treated with LHM and Dor fundoplasty. Our simulations show that even with fundoplication that raises EGJ tone, shorter myotomies lead to proper bolus outflow as well as decrease the chances of BOM formation. This is because smaller myotomy affected regions have a higher overall esophageal wall stiffness compared to larger myotomy affected zone. Stiffer walls lead to increased intrabolus pressure which opens the EGJ while weaker walls deform easily without raising the bolus pressure, and thus, the EGJ does not open, and the bolus gets retained at the myotomy site. For the same reason, as shown by simulation set 3, if the myotomy was not transmural or continued to have some

muscle fibers at the myotomy site, then the chances of BOM formation are reduced. Thus, myotomy procedures such as POEM have an advantage over LHM since it may target only the CM and leaves the LM relatively intact as described by group II of simulation set 3. POEMs are especially useful for Type III achalasia patients and patients with distal esophageal spasm where the myotomy length needs to be sufficient to include the spastic region. Hence, POEMs can go upwards of 10 cm but still be successful in retaining the myotomy wall strength sufficient to resist large deformation and aid in bolus emptying. Additionally, a real time tailored myotomy as possible with intraoperative FLIP to obtain targeted values of distensibility at the myotomy affected zone as well as at the EGJ might help in performing myotomies with lower chances of forming BOM. Different contraction patterns as observed in different achalasia types have different effects on the deformation at the myotomy site. Additionally, it has been observed that some achalasia patients have evidence of partial peristalsis after myotomy likely due to it becoming more evident in the less dilated esophagus post-treatment [**43**]. Due to the absence of contraction in achalasia I, the chances of BOM formation are minimal irrespective of the myotomy length and EGJ tone after fundoplication. But, based on our simulations, patients with EGJOO with normal peristalsis and patients suffering from achalasia III have a higher risk of forming BOM with longer myotomy length and strong EGJ tone. Therefore, it might be beneficial to aim for shorter myotomy without fundoplication for such patients. Longer myotomies performed on achalasia III patients can sometimes weaken the spastic contractions at the distal segment of the esophagus. This would reduce the chances of forming a BOM. But, on the other hand, if the myotomy is partially through the spastic segment with remnant spasm forcing bolus into the distal esophagus, it might aid in the formation of a BOM.

Thus, the myotomy length should be determined in a patient-specific manner with the help of diagnostic devices such as HRM as well as physics-based simulations [**44**] that work with HRM data.

2.8. Limitations

BOM was qualitatively defined in Triggs et al. [**28**], but there is a lack of quantitative definition of BOM in the literature. BOMs form due to tissue remodeling over a long timeline compared to the single swallows used in our modeling. Our simulations do not account for tissue remodeling. Thus, the deformation at the myotomy site seen in our simulations is not a BOM, but rather the repetitive strain that would be exerted on the myotomy. This is a limitation of the vEsophagus model. With our simulations, we can only hypothesize that factors leading to maximum deformation at the myotomy site will also impact in the formation of a BOM over a longer period. The material properties used in the vEsophagus were motivated from experimental observations of porcine esophagus due to the lack of experimental data on human esophagus. Additionally, due to the presence of the surrounding organs, the effective distensibility of the esophagus varies along its length. These complexities were not considered in our model and future work will focus on adding these components with higher level material property data from esophagectomy specimens. Additionally, the vEsophagus focuses just on the esophagus without considering the stomach. Adding a stomach to the model would increase the stiffness at distal end of the esophagus and the intragastric pressure will require higher intrabolus pressure to empty out the bolus. Considering these factors would increase the

computation time significantly without any significant additions to our current observations. Another significant limitation of this study is that we have investigated only a few types of contraction patterns as typically might be observed. In reality, the nature of contraction varies significantly swallow to swallow, particularly for achalasia II and III. Additionally, the fully closed EGJ in simulation sets 1 and 2 are idealized scenarios. Simulating the actual physiological conditions of the wide variety of contraction patterns and EGJ tone is too computationally complex and costly to be practical. The observations from our simulations are still applicable to a wide variety of contraction patterns, but it might be worthwhile to investigate the impact of contractions on BOM formation which are significantly different from what we discussed in this study. Finally, we did not consider gravity in our simulations although it is a factor in generating intrabolus pressure. Unfortunately, introducing gravity significantly increases the complexity of the simulations putting it beyond the scope of this work and making it a limitation of this work.

2.9. Conclusion

In conclusion, we performed in-silico simulations to investigate the impact of different biomechanical factors that lead to the formation of a BOM such as dimensions of the myotomy, esophageal contraction pattern, EGJ tone and residual state of muscle fibers at myotomy location. We found that long myotomies with greater EGJ tone and preserved peristalsis maximize the chances for BOM formation. Our simulations show that the best possible myotomy to minimize the chances of BOM formation is a short myotomy spanning only the length of the LES that is not transmural and has some structural architecture

intact. This should be the approach in Type II achalasia or EGJOO with propagating peristalsis that may be observed in patients with achalasia in evolution. Type I achalasia will likely not develop a BOM. Type III achalasia will most likely develop a BOM if the myotomy is partially through the spastic segment with remnant spasm forcing bolus into the distal esophagus. Although the final decision on the dimensions and modality of the myotomy will depend on multiple factors such as the type and severity of achalasia and fundoplication, our simulations using vEsophagus should be helpful in guiding the surgical plan.

CHAPTER 3

FluoroMech: Mechanics-informed fluororscopy of esophageal transport

Popular methods for evaluating esophageal disorders are the barium swallow esophagram, video fluoroscopy swallowing exam (VFSE), and high-resolution manometry (HRM). Both the esophagram and VFSE are radiographic tests that examine the dynamic function of the esophagus. In a barium swallow, barium is used as a contrast material to clearly delineate the esophageal lumen on an X-ray. This can reveal structural abnormalities of the esophagus and stomach such as hiatal hernia, diverticula, dilatation, etc. Video fluoroscopy uses the same concept, but creates a real-time X-ray movie of bolus transport. In HRM, a catheter is passed transnasally through the esophagus into the stomach (see Figure 3.1(a)). The catheter incorporates pressure sensors along its length that quantify the intraluminal pressure along the length of the esophagus as the patient swallows fluid or food. HRM provides information about the strength and velocity of peristaltic contractions as well as the tone of the upper and lower esophageal sphincters. Barium swallow and VFSE are non-invasive but provide only qualitative information about esophageal transport. On the other hand, HRM is invasive, but provides precise quantitative information about esophageal contractility. In this work, we present a method to partially bridge the gap between these methods. We have developed a method called mechanics informed fluoroscopy (FluoroMech) that can be used along with VFSE to predict the flow

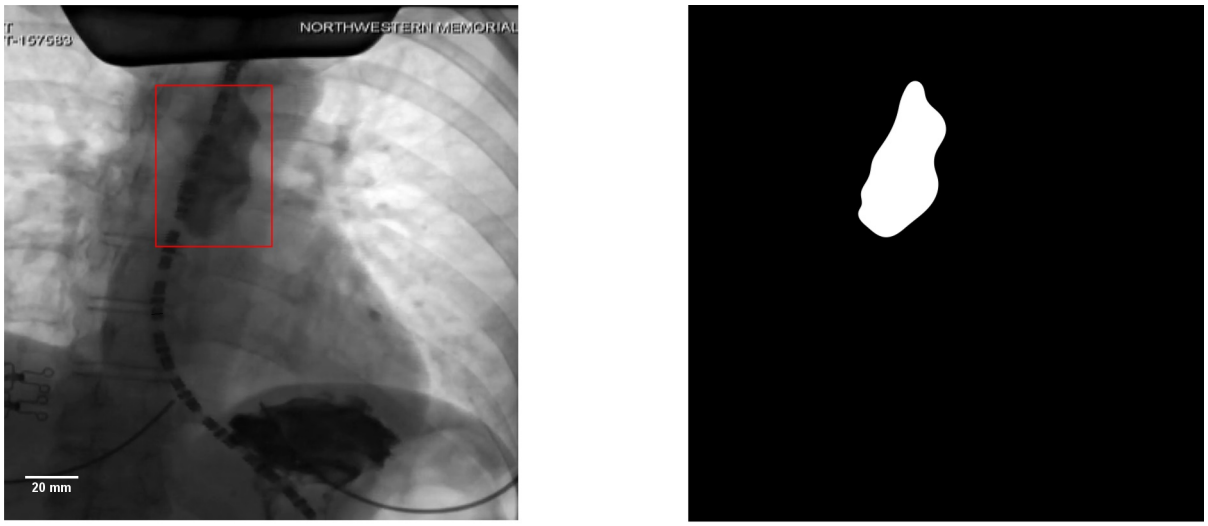

Figure 3.1. Example of an image from VFSE performed jointly with HRM on a normal subject in supine position. (a) Original esophagram image. The bolus is the dark region inside the red box. The dashed curve is the HRM catheter passing through the esophagus. The pressure sensors in the catheter can be seen as the black dashes which are separated by gaps of 1 cm. The diameter of the catheter is 4.2 mm, and is used to define the scale shown in the figure. (b) Label image showing the bolus in white and the remainder as black. The original and label images were used to train the CNN

rate, pressure and esophagus wall state, thereby providing quantitative information about bolus transport and esophageal contractility.

Previous studies have used data from fluoroscopy and manometry for the analysis with fluid mechanics [**21, 22**] and provided important insights into esophageal transport and mechanisms of a variety of disorders. However, a drawback of these techniques is that substantial time and effort is required to manually obtain the shape of the bolus from the fluoroscopy images and then perform an analysis based on that geometry. Since the geometry varies from patient to patient as well as for different swallows in the same patient, this entire analysis has to be repeated for every test sequence. Hence, these

methods are not practical for clinical applications. FluoroMech uses deep learning to perform automatic segmentation of image sequences from fluoroscopy. This eliminates the tedious manual process of segmenting the fluoroscopy images, thereby making the process significantly faster and much more convenient. These segmented images delineate the outline of the bolus which then becomes input to a one-dimensional model that predicts the fluid flow rate and pressure. We also present a method to predict the regional stiffness of the esophageal walls and the active relaxation at the locus of the bolus using the pressure predicted from the one-dimensional model and the shape of the bolus. Our analysis requires minimal input from the user and requires minimal computational time. Hence, FluoroMech can be used in clinical applications, particularly to aid in making VFSE a more powerful non-invasive diagnosis tool.

3.1. Extracting the bolus geometry

The volumetric quantification of fluid inside the esophagus can be approximated from two-dimensional images of the bolus in fluoroscopy. Figure 3.1(a) shows an example of a single image from a sequence of images generated from a VFSE of a normal subject performed with the subject in supine position. In general, a single VFSE generates 100 – 500 images depending on the time taken for each swallow sequence to complete. Hence, it is not feasible to manually outline the boundary of the barium bolus repetitively throughout the transport process. Rather, an automated technique is desirable to perform segmentation of the image sequences. There are several methods available in the literature for image segmentation such as thresholding [**45**], region growing [**46**], clustering [**47**], edge

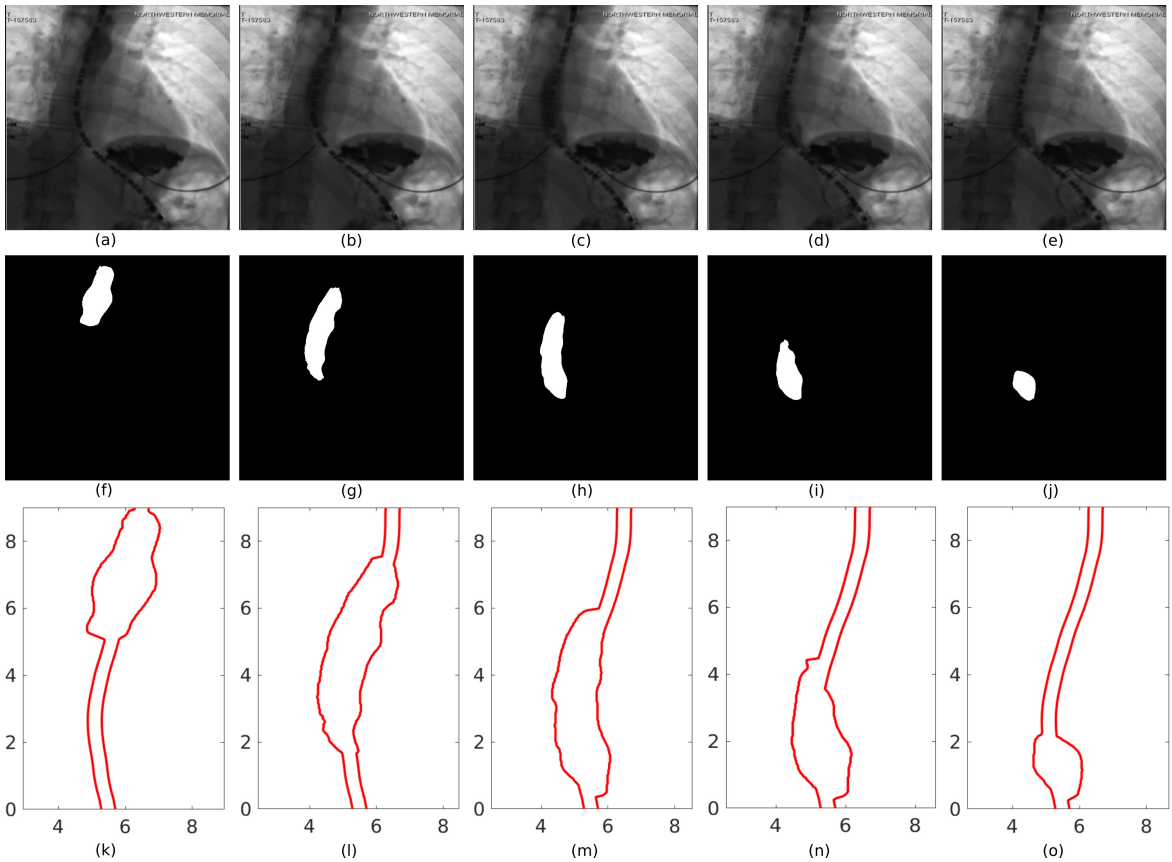

Figure 3.2. Segmentation of image frames of a VFSE. (a)-(e) Bolus transported from the proximal to the distal end of the esophagus and emptying into the stomach, (f)-(j) corresponding image segmentation, (k)-(o) corresponding outline of the esophageal lumen for analysis

detection [**48**], artificial neural networks [**49, 50, 51, 52, 53**]. Surveys of the various image segmentation techniques used in medical applications were performed by [**53, 54**]. In this work, we used a convolutional neural network architecture (CNN) called TernausNet [**51**] to perform image segmentation. TernausNet is a modified form of the classical UNet [**50**] which consists of an encoder and decoder path with skip connections that combine feature maps from the encoder and decoder paths leading to precise localization. TernausNet takes advantage of transfer learning by replacing the encoder part of U-Net with

VGG11/VGG16 network pretrained on ImageNet dataset, which consists of millions of images. Therefore, the low-level features learned from a huge dataset can be efficiently utilized and the total number of parameters to be learned is reduced significantly. The details of the neural network and its training is provided in Appendix B. Figure 3.2 shows the results after image segmentation.

3.2. Mathematical formulation

3.2.1. Governing equations

An important aspect of patient-specific analysis of esophageal transport is obtaining the flow rate and pressure field inside the esophagus with reasonable accuracy using limited computational resources and time. To that extent, we have used the formulation of a one-dimensional flow through a flexible tube [**55, 56, 57, 58**] in FluoroMech to model the transport process. The mass and momentum conservation equations in one-dimension are follows:

$$\frac{\partial A}{\partial t} + \frac{\partial Q}{\partial x} = 0, \tag{3.1}$$

$$\frac{\partial Q}{\partial t} + \frac{\partial}{\partial x}\left(\frac{4}{3}\frac{Q^2}{A}\right) + \frac{A}{\rho}\frac{\partial P}{\partial x} + \frac{8\pi\mu Q}{\rho A} = 0, \tag{3.2}$$

where ρ is the density of the fluid, μ is viscosity of the fluid, A is the cross-sectional area of the esophagus, Q is the flow rate, P is the pressure, t is the time and x is the spatial coordinate along the length of the esophagus with its positive direction defined as moving from the pharynx to the stomach. In our analysis, we only consider VFSE performed on subjects in supine position. Therefore, we do not have a gravity term in the momentum

equation. To apply our analysis on VFSE performed on subjects in upright position, it is necessary to introduce a gravity term in Equation 3.2. The factor 4/3 in Equation 3.2 comes from assuming a parabolic velocity profile perpendicular to the direction of flow.

As reported in [**59**], the fluid pressure developed within the esophagus is directly proportional to the cross-sectional area of the esophageal lumen. Hence, the pressure can be estimated using a tube-law of the form:

$$P = P_o + K\left(\frac{A}{\theta A_o} - 1\right), \tag{3.3}$$

where K is the stiffness of the esophageal wall, θ is the active relaxation factor and P_o is the intrathoracic pressure. The pressure tube law is used to estimate esophageal wall stiffness and active relaxation in Section 3.2.6. Note that K in Equation 3.3 is an average estimate of the esophageal stiffness and assumed to be constant along the length of the esophagus. The variation of the bolus shape along the esophagus length is due the variation of θ. If there is relaxation then $\theta > 1$, which effectively reduces the overall pressure developed inside the bolus.

Equations 3.1 and 3.2 are non-dimensionalized to the following form:

$$\frac{\partial \alpha}{\partial \tau} + \frac{\partial q}{\partial \chi} = 0, \tag{3.4}$$

$$\frac{\partial q}{\partial \tau} + \frac{\partial}{\partial \chi}\left(\frac{4q^2}{3\alpha}\right) + \alpha\frac{\partial p}{\partial \chi} + \psi\frac{q}{\alpha} = 0, \tag{3.5}$$

where, $\chi = x/L$, $\alpha = A/A_o$, $p = P/(\rho c^2)$, $q = Q/(A_o c)$, $\tau = ct/L$ and $\psi = 8\pi\mu L/(\rho c A_o)$. Here L is the length of the esophagus visible in the esophagram, A_o is the relaxed cross-sectional area of the esophageal lumen, and c is the average velocity of the center of the

bolus. The center of the bolus (x_b) was located at each time instant using the following relation:

$$x_b = \frac{\int_0^L x(A - A_o)dx}{\int_0^L (A - A_o)dx}. \tag{3.6}$$

Similarly, the tube law can be non-dimensionalized and written as follows:

$$p = p_o + k\left(\frac{\alpha}{\theta} - 1\right), \tag{3.7}$$

where $k = K/\rho c^2$, $p = P/\rho c^2$, and $p_o = P_o/\rho c^2$.

In this instance, $L = 11.86$ cm, $A_o = 59.04$ mm^2 and $c = 3.5$ cm/s. We assumed the properties of water (at STP) for the swallowed fluid, i.e $\rho = 1000$ kg/m^3, $\mu = 8.9 \times 10^{-4}$ Pa. s. Using these values, we get $\psi = 2.413$. The total time required for bolus to be transported through the esophagus was 5.1 seconds.

3.2.2. Initial and Boundary Conditions

The boundary conditions imposed on the FluoroMech model depend on the behavior of the upper and lower esophageal sphincters at the proximal and distal ends of the esophagus, respectively. The upper esophageal sphincter (UES) is located at the distal end of the pharynx and remains closed [**35**] in order to prevent the entry of air into the esophagus during breathing and reflux of the bolus from the esophagus back into the pharynx [**60**]. It relaxes for 0.32 - 0.5 seconds [**34**] in order to allow the bolus to enter the esophagus. The esophageal pressure topography in Figure 3.3 illustrates this behavior of the UES. The horizontal high-pressure zone at the top marks the location of the UES, which remains contracted on the HRM catheter. It opens only to allow the bolus to enter the esophagus,

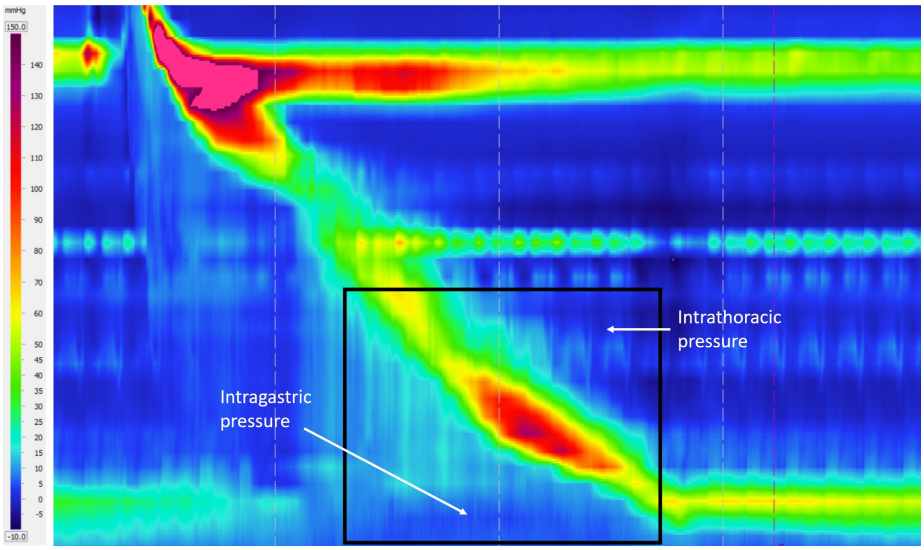

Figure 3.3. Esophageal pressure topography generated from pressure sensors on the HRM catheter. The horizontal axis represents time, and the vertical axis represents the length along the esophagus. The rectangular box shows the location of the EPT corresponding to the fluoroscopy. The horizontal high-pressure band (in red) at the top and bottom show the UES and LES tone, respectively. The peristaltic contraction is shown by the oblique high-pressure band that travels from the UES to the LES to push the bolus through the esophagus

which is visible as the break in the continuous high-pressure zone due to relaxation. The oblique band of pressure represents the peristaltic contraction which propels the bolus along the esophagus. Hence, the location of the proximal end of the bolus can be roughly identified to be just distal to the contraction. The lower esophageal sphincter (LES) is marked by the lower horizontal high-pressure zone. There is a break in high pressure in this location soon after the bolus enters the esophagus. This represents the relaxation of the LES to facilitate the bolus emptying into the stomach. In our analysis, the bolus is already inside the esophagus, and so the UES is closed. Hence, there is no flow at the entry, i.e. $q(\chi = 0, \tau) = 0$. Additionally, we assume that there was no initial flow

inside the esophagus, i.e. $q(\chi, \tau = 0) = 0$. Since Equation 3.5, contains a first-order derivative form for pressure, we have specified a reference value for the pressure (p) at the distal end equal to the intragastric pressure which in this scenario is 21.4 mmHg. This is a reasonable assumption because the LES relaxes immediately at the beginning of a swallow, and the distal end of the esophagus experiences the intragastric pressure.

3.2.3. Enforcing volume conservation

The fluoroscopy images show only a two-dimensional projection of the esophagus. Assuming a circular cross-section, we calculated the total volume of fluid inside the esophagus (as shown in Figure 3.4a). The volume V is non-dimensionalized using the product of the non-distended cross-sectional area and the length of the esophagus, i.e. $V^* = V/(A_o L)$. In terms of the volume of fluid inside the esophagus, the bolus transport is categorized into two parts: pure transport (no flow at $\chi = 1$) and emptying. From the VFSE image sequences we have observed that the transport without emptying occurs until $\tau = 0.5$, and then the volume within the esophagus decreases continuously. Since we have no flow boundary condition at the proximal end, the volume within the esophagus can never exceed the total volume at $\tau = 0$. However, during pure transport at $\tau < 0.5$, there are some fluctuations in the calculated volume within the esophagus. This can be attributed to our calculation of volume assuming the esophagus is always perfectly circular in cross-section. Since we have no information about the actual shape of the cross-section at $\tau = 0$, we can neither use the calculated volume at $\tau = 0$, nor the maximum calculated volume during the whole transport in order to enforce volume conservation.

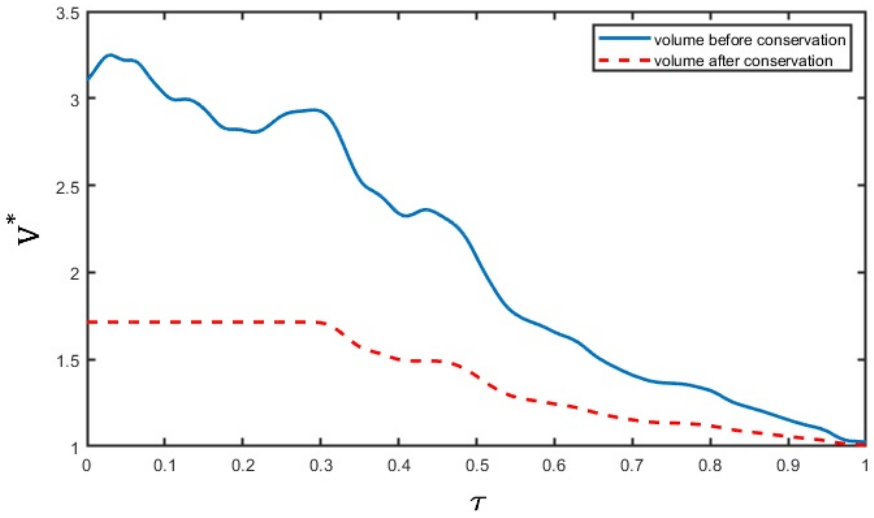

(a) Non-dimensional volume (V^*) inside the esophagus. The blue line shows the total volume of fluid inside the esophagus calculated assuming a bolus with a circular cross-section with diameter obtained from the bolus width observed in the segmented images. The red dashed line shows the total volume inside the esophagus after volume correction using the fact that the swallowed bolus is 5 mL

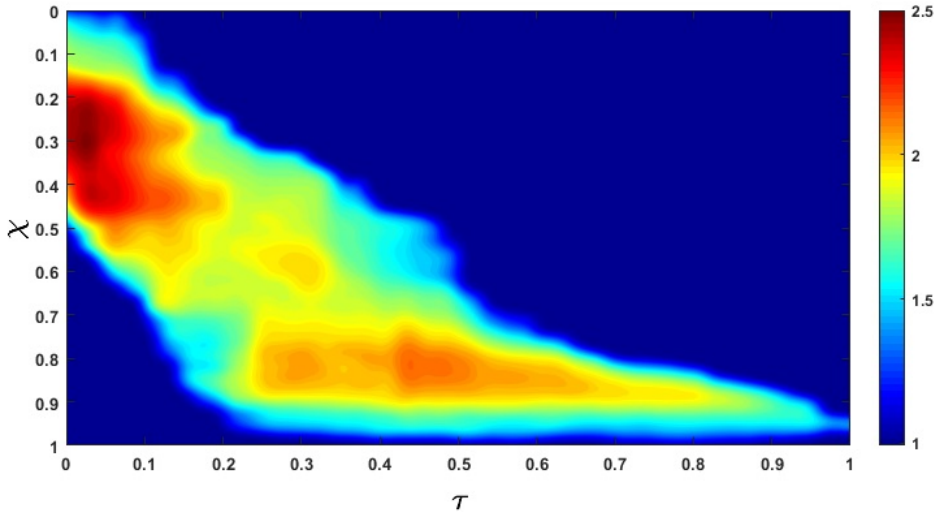

(b) Ratio of the initially assumed circular cross-sectional area (A) and the corrected cross-sectional area (A^*). The oblique band of high cross-sectional area correction shows that the correction is performed only inside the bolus, and not in the relaxed parts of the esophagus where $A/A^* = 1$

Figure 3.4. Enforcing volume conservation

In reality, the shape of the esophagus cross-section is approximately elliptical [**61**], with the major axis being observed in the fluoroscopy images. Additionally, due contact with the surrounding organs, the esophagus cross-section might take irregular shapes. Hence, the volume of the bolus calculated assuming a perfectly circular cross-section does not match the volume of fluid swallowed during every test, i.e. $V_o = 5$ mL. Therefore, it is necessary to perform a volume correction so that our analysis uses the calculated volume that is consistent with the actual swallowed volume. Since fluoroscopy images do not contain any information about the three-dimensional geometry of the bolus, the only alternative is to perform a volume correction using the two-dimensional shape of the bolus. This was done by scaling the initially assumed circular cross-sectional areas as shown below:

$$A^* = A_o + \beta\,(A - A_o)\,; \qquad \beta = \frac{V_o}{\int_0^L (A - A_o)\,dx}, \tag{3.8}$$

where A^* is the scaled cross-sectional area to conserve volume and β is the scaling factor. This method scales the cross-section of the esophagus at the bolus location only and does not change the relaxed sections.

We enforced a constant volume during pure transport (as shown by the red dashed line in Figure 3.4a) until $\tau = 0.5$. However, during emptying ($\tau > 0.5$), the volume within the esophagus begins to decrease, so, we cannot scale the volume using a reference value. Therefore, the volume is scaled using β calculated at the beginning of the emptying process ($\tau = 0.5$). In general, the shape of the esophageal cross-section varies along its length, and the shape it takes when distended depends upon the material properties of the wall. The β calculated at each time step during pure transport gives a measure of the

shape of the cross-section. As the bolus is transported through the esophagus, the β takes on different values, thereby estimating the shape in finite segments along the length. At the beginning of emptying, the distal end of the bolus has already reached the end of the esophagus. After this, the length of the bolus progressively decreases without moving any forward. Therefore, the β calculated at $\tau = 0.5$ is a reasonable scaling for volume during emptying.

During emptying, the volume within the esophagus must decrease. Therefore, if at any instant, the calculated volume inside the bolus is greater than it was in the previous time instant, we force the volume at the current instant to be equal to that of the previous instant. The effect of the bolus volume correction is shown in Figure 3.4a. The ratio of the initially assumed circular cross-sectional area (A) and the scaled cross-sectional area (A^*) is shown in Figure 3.4b. We see that the cross-sectional area scaling occurs only at the location of the bolus since A/A^* remains equal to 1 for the remainder of the esophagus. Comparing Figure 3.4a and 3.4b, we see that the maximum scaling occurs before $\tau = 0.2$ when the difference between the reference volume and the calculated volume is maximal.

It has been observed in fluoroscopy studies that sometimes the bolus gets split into two segments during transport in the upper esophagus. In such a scenario, our analysis can be applicable with some modifications. The two segments of the bolus have to be treated independently, and volume correction needs to be done separately using the reference volumes of the corresponding segments calculated at the instant when the bolus completely splits. The proximal segment continues to be in a state of pure transport, and the distal segment moves on from a state of pure transport to emptying. Although this

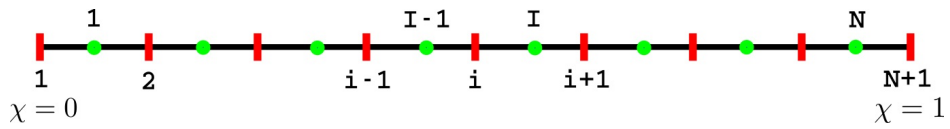

Figure 3.5. Staggered meshing of the domain. The cell boundaries and centers are shown in red and green, respectively

method works in principle, the implementation is significantly involved and is beyond the scope of this thesis.

3.2.4. Numerical solution

Using the cross-sectional areas α obtained after enforcing volume conservation, we solved for q and p in Equations 3.4 and 3.5 using the finite volume method. The flow rate (q) was calculated by solving Equation 3.4. A staggered grid was used to discretize the domain as shown in Figure 3.5. The flow rate q was calculated at the cell boundaries and pressure p was calculated at the cell centers. The cross-sectional area α was known for both the cell boundaries and centers. The quantities specified at the cell centers have subscripts in upper case, and those at the cell boundaries in lower case. The superscript o represents the value of a quantity in the previous time instant. Equation 3.4 was solved using a fully-implicit method with the following discretized form:

$$q_i = q_{i-1} + \frac{\Delta\chi}{\Delta\tau}\left(\alpha_{I-1} - \alpha^o_{I-1}\right), \tag{3.9}$$

where, N is the total number of cells, $i, I = 2, 3, ..., N, (N+1)$. Using the calculated values of q and the known values of α, we calculated the values of p at the cell centers

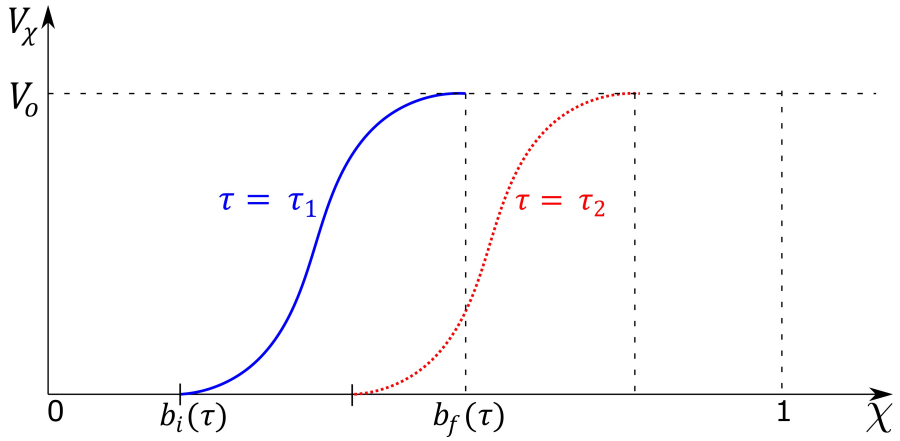

Figure 3.6. Volume inside the esophagus from 0 up to χ. The blue line shows the volume distribution at time instant τ_1, and the red dotted line shows the same as the bolus has progressed in time at τ_2. Before the beginning of the bolus $b_i(\tau)$, there is no fluid inside the esophagus, and the volume is 0. The volume inside the esophagus rises from $b_i(\tau)$ to the total volume swallowed ($V_o = 5$ mL) at the end of the bolus $b_f(\tau)$

using the following discretized form:

$$\begin{aligned} p_I =& p_{I+1} + \left(\frac{\Delta\chi}{\alpha_i}\right)\frac{q_{i+1} - q^o_{i+1}}{\Delta\tau} + \psi\frac{q_{i+1}\Delta\chi}{\alpha^2_{i+1}} \\ & - \frac{1}{3\alpha_{i+1}}\left[\frac{(q_{i+2} + q_{i+1})^2}{\alpha_{I+1}} - \frac{(q_i + q_{i+1})^2}{\alpha_I}\right], \end{aligned} \tag{3.10}$$

where $i, I = 1, 2, ..., (N-1)$. In this simulation, the total number of time steps and the total number of cells used were 510 and 171, respectively. Using these values, $\Delta\tau$ and $\Delta\chi$ was calculated as 0.003 and 0.006, respectively. The above mentioned numerical solution was implemented using MATLAB ver. R2018b.

3.2.5. Pressure variation with the shape and speed of the bolus

The intrabolus pressure during pure transport (before emptying) can be used to calculate the esophageal wall stiffness and active relaxation. Therefore, it is necessary to identify

and estimate the factors that lead to pressure variations. The flow rate can be calculated by integrating Equation 3.4 with respect to χ as follows:

$$q = -\frac{\partial}{\partial \tau}\int_0^{\chi} \alpha d\chi = -\frac{\partial}{\partial \tau}\int_0^{\chi} (\alpha' + 1)\, d\chi = -\frac{\partial V_\chi}{\partial \tau}, \tag{3.11}$$

where the cross-sectional area α is decomposed into the non-distended cross-section area (which is equal to 1 in non-dimensional form) and the extra volume present only inside the bolus (α'). V_χ is the volume inside the bolus calculated by integrating α' from 0 to χ. The variation of V_χ is shown in Figure 3.6, where b_i and b_f represent the location of the proximal and distal end of the bolus, respectively. Since the total volume V_o is conserved within the esophagus prior to the start of emptying, $V_\chi = 0$ for $\chi < b_i$ and $V_\chi = V_o$ for $\chi > b_f$. Therefore, using Equation 3.11, we get $q = 0$ for $\chi < b_i$ and $\chi > b_f$.

The effect of fluid viscosity is captured by the term $\psi \frac{q}{\alpha}$ in Equation 3.5. For a fluid with viscosity similar to water, we have observed that the viscous term is negligible compared to the other terms of Equation 3.5. Therefore, we assume the flow to be inviscid and with a flat velocity profile, and write Equation 3.5 as follows:

$$\frac{\partial}{\partial \tau}\left(\frac{q}{\alpha}\right) + \frac{\partial}{\partial \chi}\left[\frac{1}{2}\left(\frac{q}{\alpha}\right)^2\right] + \frac{\partial p}{\partial \chi} = 0. \tag{3.12}$$

On integrating Equation 3.12 with respect to χ from the distal end and using Equation 3.11, we get

$$p = p_1 + \frac{1}{2\alpha_1^2}q_1^2 - \frac{1}{2\alpha^2}\left(\frac{\partial V_\chi}{\partial \tau}\right)^2 + \frac{\partial}{\partial \tau}\int_1^{\chi} \frac{1}{\alpha}\frac{\partial V_\chi}{\partial \tau} d\chi, \tag{3.13}$$

where the subscript χ indicates the location at which each of the quantities are calculated, and p_1, q_1 and α_1 are the pressure, flow rate and cross-sectional area at $\chi = 1$, respectively. Before emptying begins, $q_1 = 0$ so, the second term of Equation 3.13 becomes equal to 0. Since $q = 0$ for $\chi < b_i$ and $\chi > b_f$, Equation 3.12 implies $\partial p/\partial \chi = 0$ at these points. Therefore, $p = p_1$ for all $\chi > b_f$ and $p = p_i$ for all $\chi < b_i$ wherein p_i is the pressure at $\chi = b_i$. Our results showed that the maximum and minimum values of p are observed at $\chi = b_i$, so p_i was used as the upper and lower bound of the pressure variation for each time step. At $\chi = b_i$, $V_\chi = 0$ so, the third term of Equation 3.13 becomes equal to 0. On applying these arguments to Equation 3.13, we get

$$p_i = p_1 + \frac{\partial}{\partial \tau} \int_{b_i}^{b_f} \frac{q}{\alpha} d\chi. \tag{3.14}$$

We define an average estimate of the bulk velocity of the bolus, u_b for every time instant as follows

$$u_b = \frac{1}{L_b} \int_{b_i}^{b_f} \frac{q}{\alpha} d\chi, \tag{3.15}$$

where, $L_b = b_f - b_i$, is the length of the bolus at each instant of time. Using Equation 3.14 and 3.15, we get

$$p_i = p_1 + u_b \frac{\partial L_b}{\partial \tau} + L_b \frac{\partial u_b}{\partial \tau}. \tag{3.16}$$

From Equation 3.16, we see that the pressure variation between its maximum and minimum can be attributed to the variation of the bulk velocity of the bolus and the change in length of the bolus during transport through the esophagus.

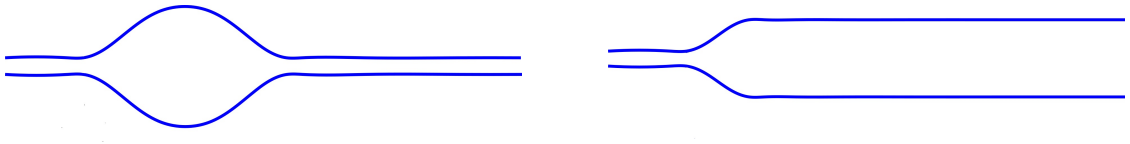

(a) Bolus shape with active relaxation in a finite segment distal to the contraction. A prominent bulge is formed in the presence of localized active relaxation

(b) Bolus shape without localized active relaxation. Typically, there is no prominent bulge in the absence of localized active relaxation

Figure 3.7. Effect of active relaxation on the shape of the bolus

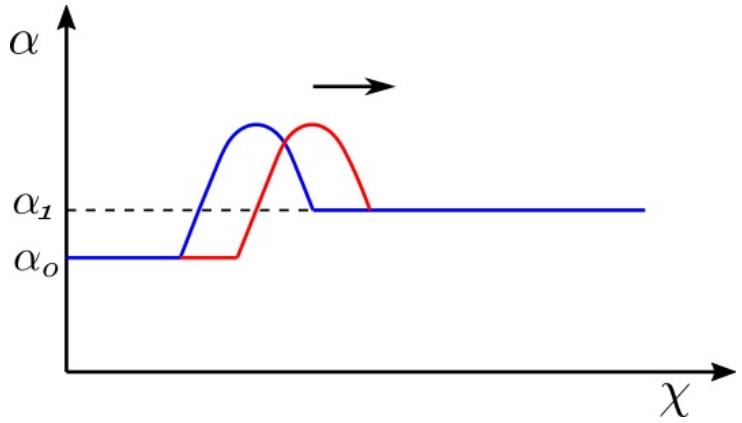

Figure 3.8. The variation of cross-sectional area shows the bolus moving in the positive χ direction. The transition from blue to the red line shows the movement of the bolus with time (also indicated by the arrow). The bulge at the bolus is due to localized active relaxation. The cross-sectional area distal to the localized bulge is α_1, and this part of the esophagus does not experience active relaxation

3.2.6. Estimating the stiffness and active relaxation of esophageal wall

The schematic diagram in Figure 3.7a shows the localized nature of active relaxation that leads to the formation of an ellipsoidal bolus. Without localized active relaxation, the shape of the bolus would typically be as shown in Figure 3.7b. In localized active relaxation as shown in Figure 3.7a, $\theta > 1$ inside the bolus and $\theta = 1$ distal to the bolus. The difference between the total pressure inside the bolus and distal to the bolus using

Equation 3.7, leads to the following form for θ after some mathematical manipulations:

$$\theta = \frac{\alpha}{\frac{\Delta p}{k} + \alpha_1}, \tag{3.17}$$

where Δp is the pressure difference between the fluid inside the bolus and distal to the bolus, and α and α_1 are the cross-sectional areas inside the bolus and distal to the bolus, respectively. Figure 3.8 shows the variation of cross-sectional area in a typical bolus transport. In the above equation, $\alpha_1 > 1$, and due to negligible viscous losses, $\Delta p << k$. With these assumptions, the active relaxation in Eq, 3.17 can be approximated without significant errors as follows:

$$\theta \approx \frac{\alpha}{\alpha_1}. \tag{3.18}$$

Sometimes it might be difficult to visualize the esophageal lumen distal to the bolus in fluoroscopy images. In such scenarios, it is impossible to accurately calculate active relaxation using this formulation. Since the minimum value of α_1 is 1, Equation 3.18 can be used to set bounds on the magnitude of θ as follows:

$$1 < \theta < \alpha. \tag{3.19}$$

A simple mathematical manipulation of Equation 3.7 gives the following relation:

$$\frac{p - p_o}{\alpha - 1} = \frac{k}{\theta}\left[1 - \frac{\theta - 1}{\alpha - 1}\right]. \tag{3.20}$$

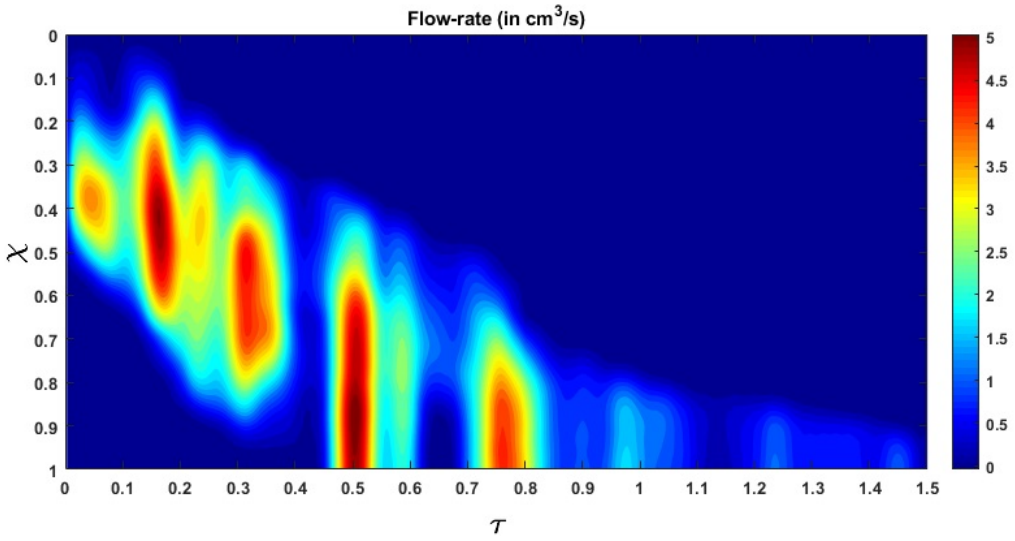

Figure 3.9. Flow rate within the esophagus. The high flow rate at $\tau = 0.5$ marks the start of emptying

Since $\alpha, \theta > 1$ and $\theta > \alpha$, the above equation leads to the following inequality:

$$\frac{k}{\theta} > \frac{p - p_o}{\alpha - 1}. \tag{3.21}$$

The left-hand side of the above equation represents the effective stiffness of the esophageal walls with the presence of active relaxation. The right-hand side represents the lower bound of this effective stiffness. The esophageal stiffness experienced by the bolus is lower than the actual stiffness of esophagus wall due to active relaxation. Therefore, the lower bound of k/θ provides an estimate of the in-vivo stiffness of the esophageal walls at the location of the bolus.

3.3. Predictions of pressure and flow rate

The variation of flow rate and pressure with non-dimensional time and distance along the length of the esophagus is shown in Figure 3.9 and 3.10, respectively. There is no

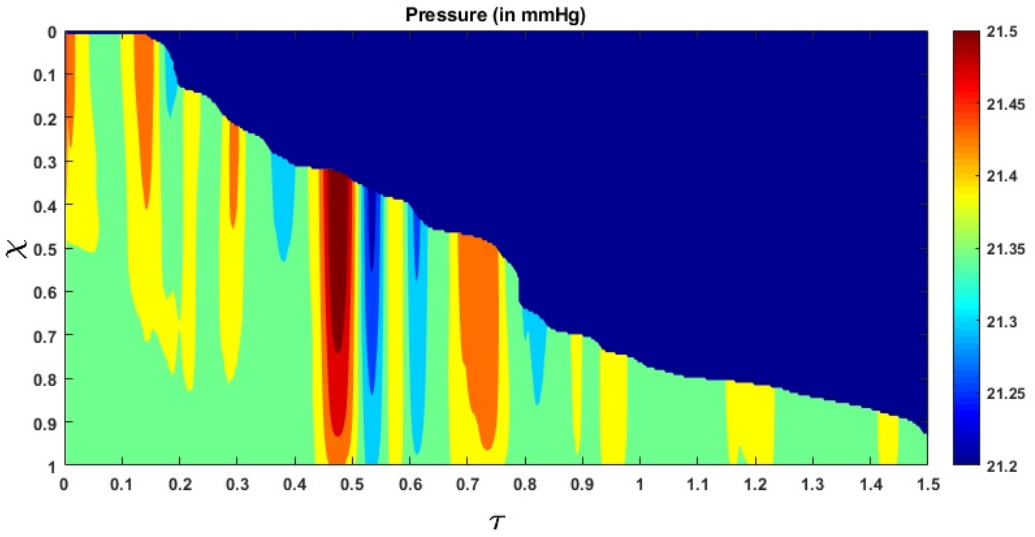

Figure 3.10. Fluid pressure within the esophagus. The high pressure gradient near $\tau = 0.5$ shows the LES requires a high pressure gradient to allow fluid to pass through it. The dynamic pressure variations are significantly small compared to the static pressure inside the esophagus

flow at $\chi = 1$ for $\tau < 0.5$, which indicates pure transport without emptying. The flow rate is non-zero only at the location of the bolus. This matches our observation from the fluoroscopy where the bolus is transported without emptying into the stomach. The variations of area with χ and τ lead to fluctuations in pressure (see Figure 3.10). As we stated in Section 3.2.5, we observe in Figure 3.10 that the maximum pressure variations can be estimated from the pressure at the proximal end of the bolus. According to Equation 3.16, these fluctuations in pressure is estimated from the variation of the bulk speed u_b and length L_b of the bolus as shown in Figures 3.11a and 3.11b, respectively. Although p is calculated over the whole domain, the fluid pressure within the bolus is the most accurate description of the actual transport process. This is because the VFSE provides information only about the shape of the bolus. Therefore, we have ignored the calculated pressure proximal to the bolus and replaced with a reference value of zero.

Additionally, the peristaltic contraction at the proximal end of the bolus, where the diameter is significantly less, cannot be observed in the fluoroscopy, and is fully occluded most of the time, thereby dividing the fluid domain into two parts. Our FluoroMech model does not incorporate this contraction zone, and instead treat this zone the same as the remainder of the non-bolus domain. Consequently, we do not see a high-pressure zone at the proximal end of the bolus as seen in the Figure 3.3. The calculated fluid pressure is the sum of the contributions from the static and dynamic fluid pressures inside the bolus. In this particular scenario, the static pressure is the intragastric pressure specified as a boundary condition at the distal end of the esophagus and is equal to 21.4 mmHg. The static pressure is independent of the flow and remains constant throughout the fluid domain. On the other hand, the dynamic pressure depends only on the fluid flow and is shown as the pressure variations in Figure 3.10. From the magnitude of the fluid pressure variations, we see that the dynamic pressure is 2 orders of magnitude smaller than the static pressure. The total pressure inside the bolus is therefore mainly due to the static pressure. The difference between the static pressure inside the bolus and the intrathoracic pressure (8 - 12 mmHg in this case) is balanced by the stresses developed in the esophagus walls due to elastic deformation. The dynamic pressure in the bolus accelerates or decelerates the bolus fluid and balances the viscous drag on the fluid at the esophagus walls. The low values of dynamic pressure compared to the static pressure indicate that the effect of viscosity and fluid acceleration/deceleration on the total fluid pressure in this case is significantly lower compared to the effect of elastic deformation of the esophagus walls in pressurizing the bolus fluid. The manometer readings of fluid pressure inside the bolus mainly represent the static pressure, and in

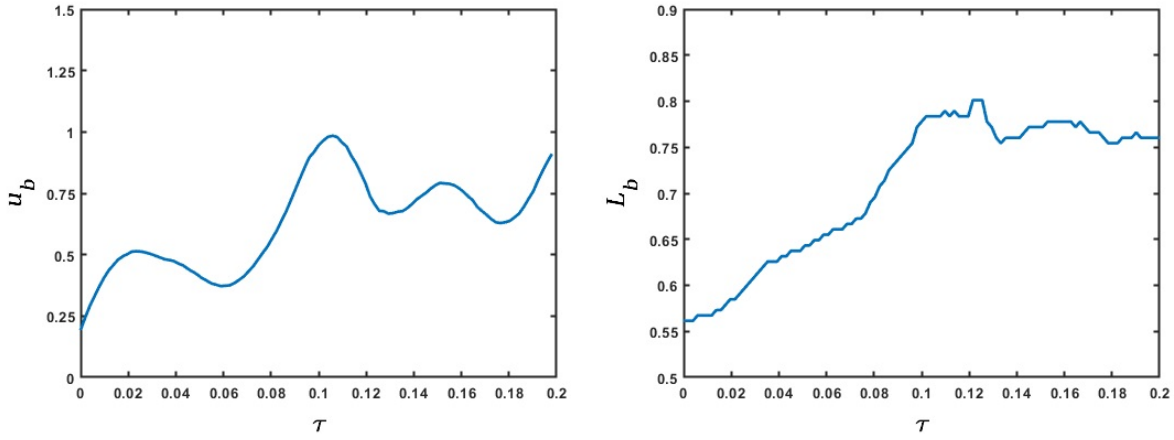

(a) Bulk speed of the bolus

(b) Length of the bolus

Figure 3.11. Variation of bolus speed and length before emptying. The rate of change of the product of bulk bolus speed and length of the bolus with respect to time quantifies the dynamic pressure variations shown in the previous figure. The variation of bulk bolus speed and its length provide physical intuition of the sources of pressure fluctuations

this case, the measured intrabolus pressure lies between 20 - 25 mmHg. The dynamic pressure variations are too small to be accurately measured by manometry, and so cannot be validated with manometry data. The magnitude of pressure from manometry at the contraction is 50-110 mmHg (shown in Fig. 3.3). Therefore, the contraction pressure is roughly 3 orders of magnitude greater than the dynamic fluid pressure predicted by FluoroMech. Emptying begins at $\tau = 0.5$, which corresponds to $q > 0$ at $\chi = 1$. This continues until all fluid is emptied into the stomach. From Figure 3.9 and 3.10 we see that during emptying, a high flow rate corresponds to a high intrabolus pressure. In our model, the reference intragastric pressure is specified at $\chi = 1$, so, a high flow rate at $\chi = 1$ requires a higher pressure to be developed inside the esophagus to drive the fluid out. This high pressure inside the bolus indicates the presence of the LES and shows how it behaves differently from the remainder of the esophagus. During normal esophageal

transport, the walls distend to accommodate the incoming bolus, and contract back to their relaxed state once the bolus has passed. However, the LES does not distend like the rest of the esophagus, hence a greater pressure inside the bolus is required for the fluid to traverse it.

It is difficult to identify the sources of the dynamic pressure fluctuations as shown in Figure 3.10 from the two-dimensional fluoroscopy study. Although our analysis is based on VFSE performed with the subject in supine position, internally the esophagus is never fully horizontal and might have many undulations with varying extents. These undulations can be thought of as small hills and valleys along the length of the esophagus. When the bolus moves up an undulation, it slows down locally and when it moves down an undulation, it locally accelerates. These local acceleration and deceleration lead to fluctuations in the calculated pressure. The esophagus might deform as well due to contact with surrounding organs, which in turn vary with time due to the heart beating, vasculature pulsating, respiration, and overall body movement leading to variations in cross-sectional areas and consequently the pressure.

3.4. Predictions of stiffness and active relaxation

The esophageal wall stiffness and active relaxation predicted by the FluoroMech model depends on the cross-sectional area only at the bolus. The variation of cross-sectional area during pure transport is shown in Fig. 3.12. In this figure, we see that the bolus cross-sectional area varies from 2 to 3.5. As described in Section 3.2.6, our model predicts the minimum stiffness of the esophageal walls which occurs at location of the bolus. The wall stiffness at the bolus is smaller than the rest of the esophagus due to active relaxation.

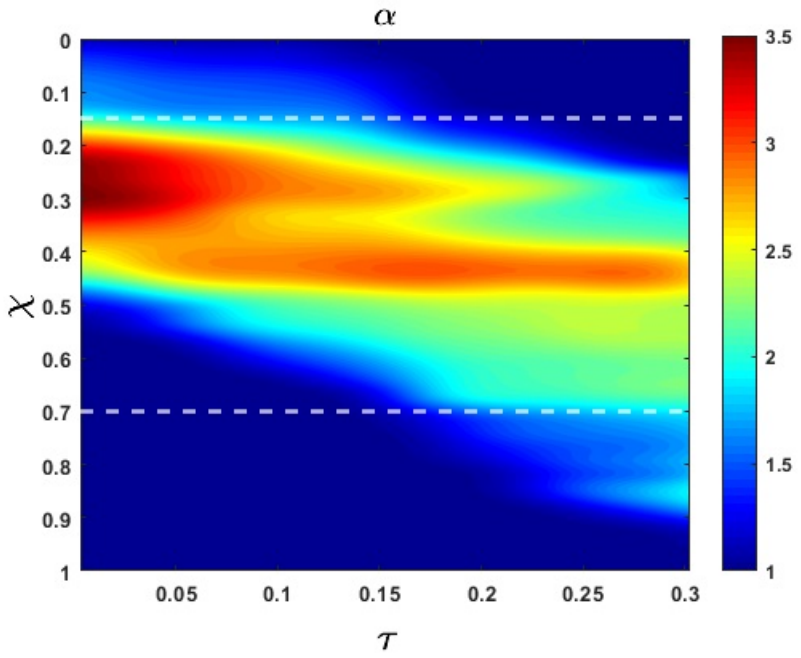

Figure 3.12. Variation of non-dimensional cross-sectional area with χ and τ during bolus transport without emptying. At $\tau = 0$, α is higher but the bolus has a shorter length. Towards the end of the transport, the bolus elongates but α decreases due to conserved volume during pure transport. The white horizontal dashed lines (at $\chi = 0.15$ and 0.7) mark the length of the esophagus that displays a prominent bolus that can be used to estimate stiffness and active relaxation of the esophageal walls

Additionally, the cross-sectional areas are known most accurately at the bolus since that is the only part of the esophagus observed in fluoroscopy. Therefore, in order to calculate stiffness and active relaxation, we consider cross-sectional areas inside the bolus only as indicated by the two horizontal white dashed lines in Figure 3.12. The intrathoracic pressure p_o can also be observed from the EPT in Figure 3.3 as the pressure readings proximal to the peristaltic contraction. In this case, the intrathoracic pressure is approximately 8 - 12 mmHg. Using the pressure predicted by our model, and intrathoracic pressure observed from EPT, we calculated the lower bound of esophageal stiffness according to

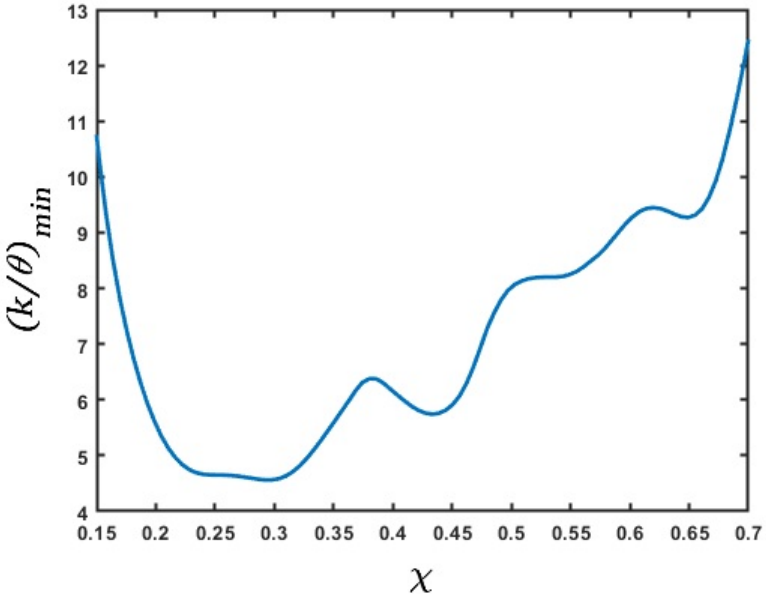

Figure 3.13. Variation of minimum stiffness (in mmHg) along the length of the esophagus. The x-axis represents the length of the esophagus marked by the dashed horizontal lines in Figure 3.12. This measure of stiffness incorporates the effect of active relaxation, therefore, its low values correspond to the high values of cross-sectional areas. The predicted high stiffness at $\chi = 0.15$ and 0.7 is due to the influence of the peristaltic contraction and the LES, respectively

Equation 3.21. This estimate of stiffness refers to lowest stiffness that the bolus encounters and captures the effect of active relaxation. Figure 3.13 shows the variation of the minimum value of k/θ along the length of the esophagus lying between the white dash lines in Figure 3.12. These values of stiffness correspond to the maximum cross-sectional area at any point along the length of the esophagus. In this plot, we have considered the mean of the range of values for intrathoracic pressure, i.e. 10 mmHg. The plot shows the variation of esophageal wall stiffness to be approximately 4.5 - 12.0 mmHg. On comparing Figures 3.12 and 3.13, we see that the minimum stiffness correspond to the maximum cross-sectional areas and vice-versa, which is consistent with the tube-law in Equation 3.7.

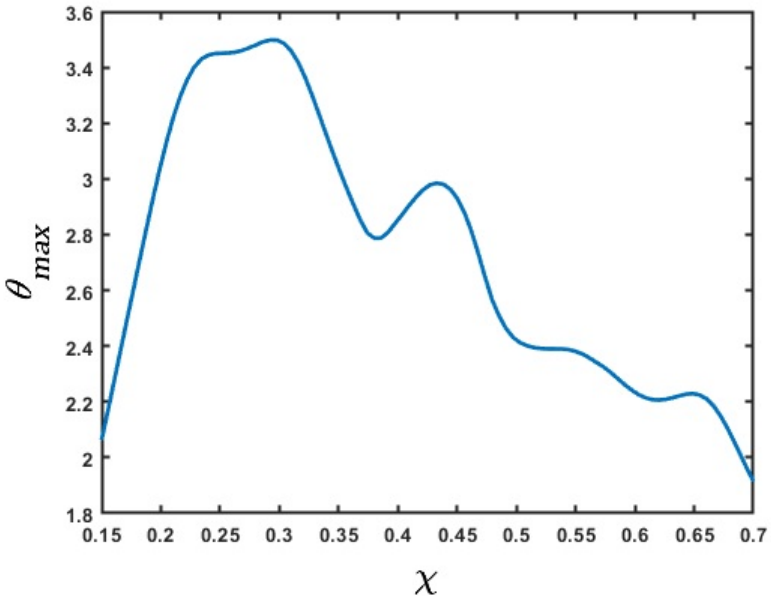

Figure 3.14. Variation of the maximum active relaxation factor. The x-axis represents the length of the esophagus marked by the dashed horizontal lines in Figure 3.12. The high values of θ_{max} correspond to the low values of stiffness. The low values of θ_{max} at the $\chi = 0.15$ and 0.7 are due to the influence of the peristaltic contraction and the LES, respectively

It should be noted that the values of the calculated stiffness have a contribution from the surrounding organs as well. Some locations of the esophagus experience indentations from surrounding organs, and that appears in form of a prediction of relatively high stiffness. Since the stiffness is predicted using fluid pressure, there is no way to distinguish the effect of the surrounding organs from the actual stiffness of the esophagus walls. In Figure 3.13 we see that the stiffness values are higher towards the two ends of the x-axis. At the left end, the peristaltic contraction collapses the esophagus, and therefore, our model captures this behavior by predicting a higher stiffness near this region. At the right end, the LES does not distend like the rest of the esophagus. This behavior is manifested

through a higher predicted stiffness at the right end. Therefore, we hypothesize that the lower values of predicted stiffness are closer to reality.

The in-vivo mechanical properties of human esophagus are reported in [**62, 63, 59**]. In these studies, a probe with a balloon/FLIP (functional lumen imaging probe) was inserted into the esophagus and the balloon/FLIP was filled with water to distend the esophagus. The sensors in the probe measure the cross-sectional areas and pressure inside the esophagus. [**62**] reported the data of 13 healthy subjects (9 male; age range, 20-27 years), [**63**] reported data of 11 healthy subjects (5 male; age range, 22-39 years), and [**59**] reported data of 15 healthy subjects (6 male; age range, 21-68 years). These studies show a linear relationship between pressure and cross-sectional area, and were the motivation for the use of a linear tube-law in Equation 3.7. The slopes of their reported plots give an estimate of the quantity A_o/K, where A_o is the relaxed cross-sectional area of the esophagus, and K is the stiffness of the esophagus walls. The A_o/K from [**62**] and [**59**] were approximately 11.6 mm^2/mmHg and 9.1 mm^2/mmHg, respectively. [**63**] reported the relation between pressure and cross-sectional areas at different regions of the esophagus. The A_o/K in these regions lies in the range 9.5 - 11.5 mm^2/mmHg. Using the relaxed cross-sectional area in our analysis, we calculated A_o/K to be 4.9 - 13.1 mm^2/mmHg for the subject analyzed. The relaxed cross-sectional area of the esophagus is reported in [**61**] as $7-59 mm^2$. Using this range for cross-sectional areas, the stiffness from [**62**], [**63**], and [**59**] results to 0.6 - 5.0 mmHg, 0.6 - 6.2 mmHg, and 0.8 - 6.5 mmHg, respectively. Therefore, the stiffness of the esophagus of the subject in our analysis is of the same order and close to the range of values reported in literature. An accurate measure of the intrathoracic pressure would increase our accuracy for prediction of esophageal stiffness.

Figure 3.14 shows the variation of the maximum active relaxation along the length of the esophagus lying between the white dashed lines in Figure 3.12 according to Equation 3.18. Since it is difficult to visualize the esophagus lumen distal to the bolus in the fluoroscopy images used for this analysis, we assume $\alpha_1 = 1$, which correspond to the upper bound of active relaxation according to Equation 3.19. We see that the maximum value of the active relaxation lies between 2 and 3.5. On comparing Figures 3.13 and 3.14, we observe that the maximum relaxation occurs at the locations of minimum stiffness.

Although the FluoroMech model provides a simple non-invasive technique to predict esophageal wall stiffness and active relaxation, the fluoroscopy images that are used as input to the model, impose certain limitations to the capability of FluoroMech. Due to the inherent lack of information about the three-dimensional geometry of the bolus, we make some assumptions about the esophageal cross-sectional areas by enforcing volume conservation of the bolus so that the transport follows the physical laws. The cross-sectional areas obtained after volume conservation might not be exactly the same as in reality, and might lead some inaccuracies in our predictions. The dynamic pressure variations due to the unnecessary variations in cross-sectional areas are negligible compared to the static pressure inside the bolus. Therefore, the effect of minor inaccuracies in extracting cross-sectional areas from fluoroscopy images in the prediction of esophageal wall stiffness and active relaxation is mitigated to a reasonable extent. The stiffness predicted by the model can be higher than the actual stiffness at some locations due to the surrounding organs pressing against the esophagus. The prediction of esophageal wall stiffness and active relaxation is sensitive to the relaxed lumen cross-sectional area and the cross-sectional area

distal to the bolus, respectively. Identifying these cross-sectional areas in fluoroscopy images is sometimes difficult due to the lack of barium lining the esophageal lumen in such locations. This might add to some inaccuracies in our prediction. FluoroMech can be very easily applied to other imaging techniques such as computed tomography (CT) or magnetic resonance (MR) imaging that can provide a better imaging of the three-dimensional bolus, relaxed lumen cross-section and identify locations where the surrounding organs press against the esophagus, and hence predict wall stiffness and active relaxation more accurately. Additionally, the esophageal wall stiffness prediction is dependent on the accurate measurement of the intragastric and intrathoracic pressure. Therefore, FluoroMech used along with manometry (as described in this work) leads to better prediction of wall stiffness.

3.5. Conclusion

We have presented FluoroMech, a technique for analyzing fluoroscopy image data using deep learning and computational fluid dynamics. The image sequence from fluoroscopy was segmented using a Convolutional Neural Network to obtain the outline of the bolus as it transits the esophagus. This bolus outline then becomes the input to a computational model that solves the one-dimensional mass and momentum conservation equations to obtain the fluid flow rate and pressure. Since fluoroscopy provides information only about the shape of the bolus in a single two-dimensional plane, we made approximations regarding the esophageal cross-sectional areas to conserve the volume of swallowed fluid. We observed that the static pressure inside the bolus is significantly greater than the dynamic pressure. This indicates that the effect of elastic deformation is

significantly greater than combined effect of the viscous drag at the esophageal walls and local acceleration or deceleration of the bolus fluid in pressurizing the bolus fluid. Based on our mechanistic study, we have categorized the esophageal transport into four zones: contraction zone behind the bolus, active relaxation zone at the bolus, stiff zone at the LES and a baseline zone for the remainder of the esophagus.

Using the shape of the bolus and the pressure predicted from this model, we have presented a method to estimate the esophageal wall stiffness. We concluded that the lower values of the predicted stiffness reflect the actual stiffness of the walls since contact with surrounding organs can lead to a higher predicted stiffness. The stiffness predicted by FluoroMech was of the same order and close to the range of values reported in other studies. We also presented a method to estimate active relaxation of the esophagus walls at the bolus using a relaxation factor. Since the dynamic pressure variations are negligible compared to the static pressure inside the bolus, the stiffness and active relaxation estimated by our model are not sensitive to minor inaccuracies in cross-sectional areas extracted from fluoroscopy images. Thus, FluoroMech reliably predicts the state and functioning of the esophagus.

CHAPTER 4

MRI-MECH: Mechanics-informed MRI to estimate esophgeal health

Dynamic magnetic resonance imaging (MRI) is a popular medical imaging technique to generate image sequences of the flow of a contrast material inside tissues and organs. However, its application to imaging bolus movement through the esophagus has only been demonstrated in few feasibility studies and is relatively unexplored. In chapter 3, we introduced a framework called FluoroMech applied to fluoroscopy images to estimate the mechanical health of the esophagus. FluoroMech enhances the capability of fluoroscopy by adding quantitative predictions to fluoroscopy data which is inherently qualitative in nature. In this chapter, we present a framework called MRI-MECH which uses dynamic MRI as input to estimate esophageal health. Both FluoroMech and MRI-MECH utilize the input of esophageal cross-sectional area varying as a function of time and length along the esophagus. However, there are some key differences in their approach that can be classified into two categories. The first category pertains to differences between fluoroscopy and dynamic MRI. Fluoroscopy is an older and simpler approach wherein X-ray imaging is used to visualize a swallowed bolus passing through the esophagus resulting in a video with high temporal resolution, but only a two-dimensional projection of the bolus. Hence, the three-dimensional geometry of the bolus is unknown. Fluoroscopy is a well established clinical test. Dynamic MR imaging, on the other hand, is a relatively

complicated and evolving technology. In its current state, dynamic MRI images have significantly lower temporal resolution but very detailed three-dimensional representation of the bolus. However, dynamic MR imaging is currently not a standard practice for evaluating esophageal disorders offering a vast potential for improvement. The second category of differences between FluoroMech and MRI-MECH lie in the implementations of the frameworks. FluoroMech uses the finite volume method to predict esophageal wall stiffness and active relaxation with the variation of cross-sectional area as input. It is computationally fast (less than a minute) and requires very limited computational resources but requires a complete dataset of the variation of cross-sectional area. Assumptions are required regarding the 3-D shape of the bolus based on the volume of fluid swallowed and since model predictions are sensitive to cross-sectional area variation, inaccuracies in measurements reflect on the predictions as well. MRI-MECH, on the other hand, uses a physics-informed neural network (PINN) [**64**] to make predictions and is much computationally demanding (takes approximately one hour to run) requiring better hardware, especially the GPU, to train the PINN. However, MRI-MECH is not sensitive to missing or imperfect measurements. Additionally, it does not require assumptions regarding the esophageal lumen cross-sectional shape because MRI provides three-dimensional geometry of the esophageal lumen. In the following sections, we describe the MRI-MECH framework in detail along with its application to a dynamic MRI sequence.

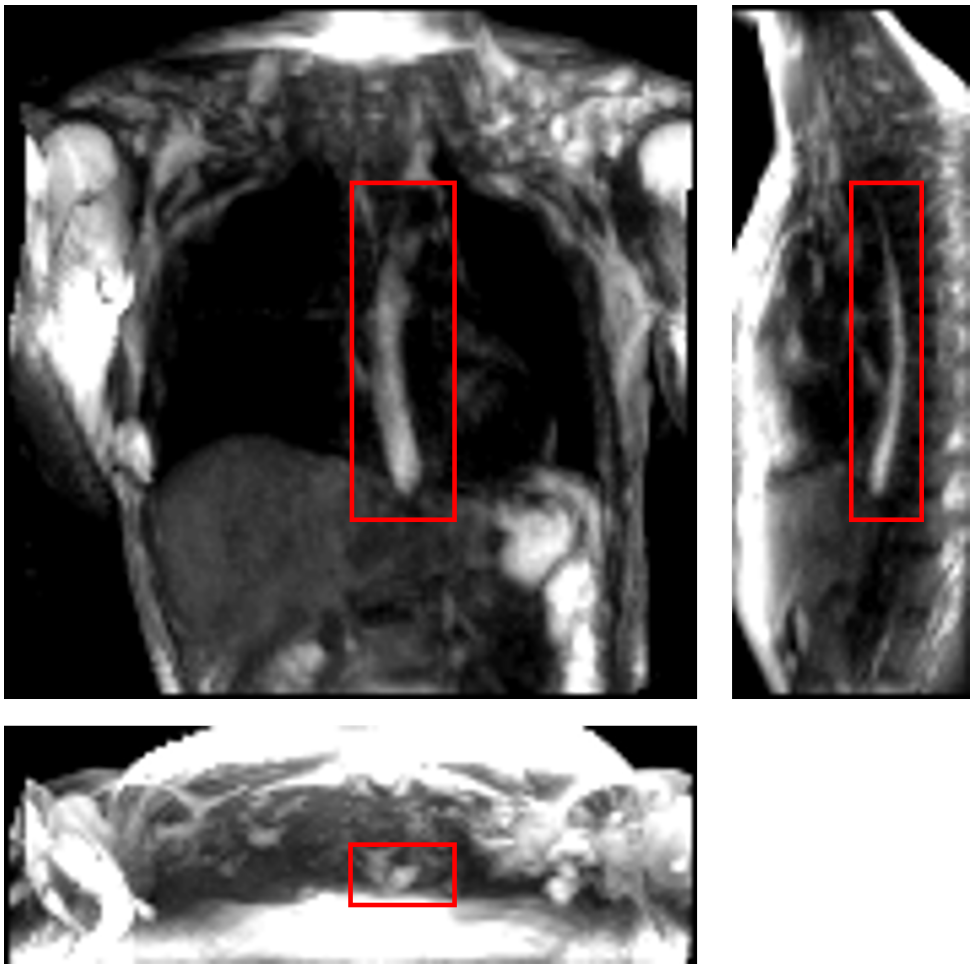

Figure 4.1. One instant of a dynamic MRI of a normal subject as seen in three perpendicular planes. The planes (from left to right to bottom) are coronal, sagittal and axial, respectively. The bolus can be seen as the bright region inside the red boxes. Concentrated pineapple juice was swallowed as a contrast agent.

4.1. Accelerated dynamic MRI

Imaging was performed at 1.5 T (Aera, Siemens, Germany) using a 3D MR angiography sequence (TWIST, Siemens, Germany) designed for contrast-enhanced cardiac imaging applications which was adapted to be used for esophageal imaging using pineapple juice as an oral contrast agent. Sequence parameters included $(3.25\ \text{mm})^3$ spatial / 1.17

s temporal resolution, $(416\ \text{mm})^2 \times 143$ mm coronal field of view, 0.78 ms echo time, 2.36 ms repetition time, 29^o tip angle, 620 Hz/pixel bandwidth, 6/8 partial Fourier acquisition, R=2 GRAPPA acceleration, 8% central size / 10% outer density view sharing. A 4-channel cardiac coil was used for image acquisition, placed on the upper torso surface. To improve image conspicuity of the juice bolus, pineapple juice (100%, Costa Rica) was reduced to a volume factor of 0.48 (i.e. 52% volume removed) through gradual heating without boiling. By doing so, the T1 of the juice at 1.5 T was reduced from 265 ms (raw / non-volume reduced juice) to 76 ms (volume-reduced juice), as measured by variable flip angle signal fit. A healthy volunteer (37 year old male) was given 20 ml of the volume-reduced pineapple juice to swallow during image acquisition. The juice was administered via a plastic tube and syringe controlled by the scan subject. The subject was instructed to swallow by voice command from the scan operator, given 10 seconds after the start of image acquisition, with 75 seconds of imaging performed to capture complete esophageal transit. To visualize the bolus transport, maximum intensity projections were created. Figure 4.1 shows an instant during bolus transport on three perpendicular slices.

4.2. Extraction of bolus geometry

The MRI output consisted of a cuboid wherein voxels in a Cartesian coordinate system had different magnitudes of intensity. The temporal resolution of the dynamic MRI (1.17 second) determined the number of images with the bolus seen within the esophagus; 7 time instants in this study. The typical length of an adult esophagus is 18 - 25 cm [**65**]. The average velocity of a normal peristalsis is approximately 3.3 cm/s [**66**]. Thus, an average swallow sequence usually takes 5 - 8 seconds. Therefore, temporal resolutions similar to

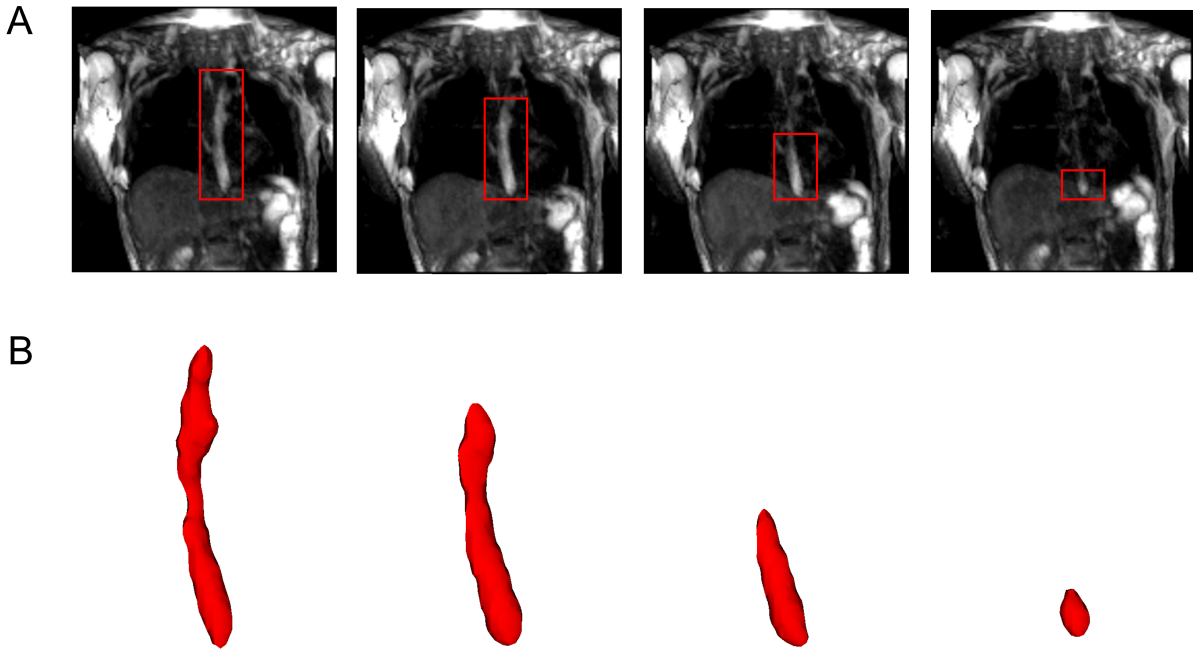

Figure 4.2. Segmentation of MR images. (A) The bolus is shown in the coronal plane at four time instants (progressing from left to right). The bolus is seen as the bright region inside the red boxes. The bolus volume decreased with time as it was emptied into the stomach. (B) The corresponding 3D segmented bolus shapes for the four time instants. Bolus size has been magnified for visualization.

what we used in our analysis typically result in 5 - 8 images. Although this temporal resolution is not comparable to fluoroscopy, the detailed three-dimensional geometry of the bolus in MRI leads to better prediction of velocity and intrabolus pressure resulting in better prediction of esophageal wall properties. The bolus was manually segmented for the 7 time instants, a few of which are shown in Figure 4.2. The segmentation assigned a value of 1 and 0 to each voxel that lay inside and outside the bolus, respectively. The image segmentation was performed using the open-source software ITK-SNAP [**67**]. With improved MR imaging and better temporal resolution, manual image segmentation might

not be feasible and more sophisticated automated segmentation techniques [**68**] might be necessary.

MRI-MECH modeled the esophagus as a one-dimensional flexible tube. For such one-dimensional analysis, the variation of cross-sectional areas at different points along the length of the esophagus and different time instants had to be extracted from the three-dimensional bolus obtained from segmentation. This was done in two steps. The first step was to generate a center line along the length of the esophagus. The bolus shapes observed at different time instants were superimposed and then cross-sections of the superimposed shape at different horizontal planes from the proximal to the distal end of the superimposed shape were generated. The centroids of these cross-sections were connected to form the center line. The length of the center line in this case was 9.65 cm. The second step, after extracting the center line, was to generate planes perpendicular to the centerline as shown in Figure 4.3. The segmented voxels marked 1 which lay near these perpendicular planes were projected onto these planes. These projected points were connected using Delaunay triangulation as shown in Figure 4.3. The cross-sectional area at each point along the center line was then calculated as the sum of the triangles in the Delaunay triangulated geometries.

4.3. MRI-MECH formulation

4.3.1. Governing equations

Transport through the esophagus was modeled as one-dimensional fluid flow through a flexible tube. The mass and momentum conservation equations in one dimension [**55, 58,**

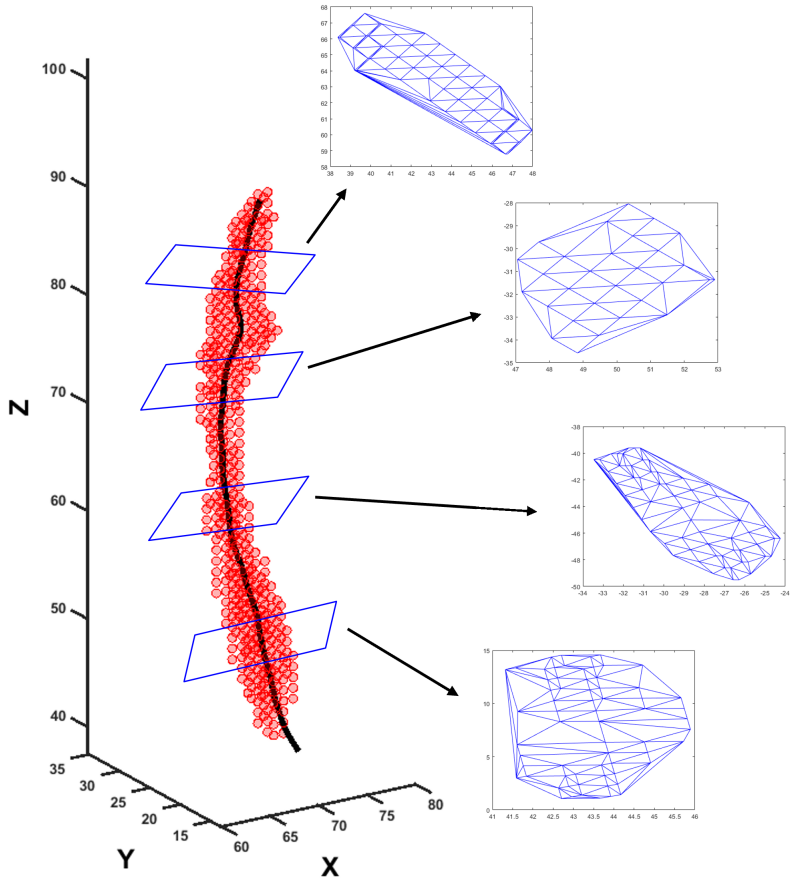

Figure 4.3. Extraction of cross-sectional areas from dynamic MR images. The segmented bolus geometry at one time instant is shown by the red points in the scatter plot. The generated center line is shown by the black curve inside. A few planes are shown which are perpendicular to the center line and on which the cross-sectional areas were calculated. The points on the planes were meshed using Delaunay triangulation and the triangulated shapes approximate the cross-sectional areas at those planes.

57, 56] (with slight modification from Equations 3.1 and 3.2) are as follows:

$$\frac{\partial A}{\partial t} + \frac{\partial (AU)}{\partial x} = 0, \tag{4.1}$$

$$\frac{\partial U}{\partial t} + \frac{\partial}{\partial x}\left(\frac{U^2}{2}\right) + \frac{1}{\rho}\frac{\partial P}{\partial x} + \frac{8\pi\mu U}{\rho A} = 0, \tag{4.2}$$

where A is the cross-sectional area of the esophageal lumen, U and P are the velocity and pressure in the bolus fluid, respectively. x represents the distance along the length of the esophagus from the mouth to the stomach and t represents time. The total time for bolus transport in our analysis was 6.95 seconds. ρ and μ are the density and dynamic viscosity of the transported fluid, respectively. Pineapple juice was the swallowed fluid whose density and viscosity were 1.06 g/cm^3 and 0.003 Pa.s [**69**], respectively.

As described in chapter 3, the fluid pressure developed inside the esophagus is linearly proportional to the cross-sectional area of the esophageal lumen [**62, 59**] in the absence of any neuromuscular activation. Using this information, we used the same pressure tube law as described by Equation 3.3. In this case, the inactive cross-sectional area A_o was 27mm^2. The activation parameter θ takes the value of 1 in the inactive state of the esophagus. It can be seen from Equation 3.3 that in the inactive state, when the cross-sectional area of the esophageal lumen is equal to A_o, the pressure inside the esophagus is equal to P_o. Due to the lack of information about the thoracic pressure, we assume that $P_o = 0$ mmHg. An activation is induced when $\theta < 1$ raising the pressure locally. On the other hand, $\theta > 1$ decreases the bolus pressure and estimates the active relaxation of the esophageal wall. Thus, the parameter θ captures the effect of the esophageal motility.

Due to the low resolution of the dynamic MRI, it was necessary to interpolate the MRI data to smaller temporal and spatial scale. The measured volume V_m of the bolus from the proximal end ($x = 0$) to any point $x > 0$ was calculated as follows:

$$V_m = \int_0^x A_m dx, \tag{4.3}$$

where A_m is the measured cross-sectional area of the esophageal lumen at a coarse x and t. The volume V_m was interpolated using piecewise cubic Hermite interpolating polynomial to a smaller temporal and spatial scale to obtain V. V_o was known at 7 time instants and 59 points along x. The interpolated V was calculated at 100 time instants and 100 points along x. Using Equations 4.1 and 4.3, the cross-sectional areas and velocities at finer t and x were calculated as follows:

$$A = \frac{\partial V}{\partial x}, \tag{4.4}$$

$$U = -\frac{1}{A}\frac{\partial V}{\partial t}. \tag{4.5}$$

The values of A and U were then used to solve for P in Equation 4.2. Equations 4.1 and 4.2 were non-dimensionalized as follows:

$$\frac{\partial \alpha}{\partial \tau} + \frac{\partial(\alpha u)}{\partial \chi} = 0, \tag{4.6}$$

$$\frac{\partial u}{\partial \tau} + \frac{\partial}{\partial \chi}\left(\frac{u^2}{2}\right) + \frac{\partial p}{\partial \chi} + \varphi\frac{u}{\alpha} = 0, \tag{4.7}$$

where $\alpha = A/A_s$, $u = U/c$, $\chi = x/\sqrt{A_s}$, $\tau = ct/\sqrt{A_s}$, $p = P/(\rho c^2)$, $\varphi = (8\pi\mu)/(\rho c\sqrt{A_s})$, $A_s = \max(A)$, and $c = 5$ cm/s is a reference speed of peristalsis. In this work, $A_s = 197.73$ mm^2. Using the properties of the swallowed fluid and the scales for A and U, we found $\varphi = 0.101$. The non-dimensional form of the pressure tube law remains the same as described by Equation 3.7. This non-dimensionalization ensures that the magnitudes of α, u, and p lie between -1 and 1, which is essential for good prediction by the PINN as described later.

Figure 4.4. The lower esophageal sphincter (LES) identified at a single time instant outlined in red with a diameter of approximately 7.89 mm and a length of approximately 2.78 cm. The stomach can be seen to the right of the LES with the accumulated pineapple juice shown in bright white. The esophageal body cannot be seen in this slice because this plane does not intersect the esophagus.

4.3.2. Initial and boundary conditions

The boundary conditions of this problem were specified to capture the physiological conditions of normal esophageal transport. The upper esophageal sphincter (UES) at the proximal end of the esophagus opens to allow the bolus into the esophagus, closes once the fluid has passed through it, remains closed thereafter. Hence, we specified zero velocity at $x = 0$ for all time instants. This condition also ensures that $V_m = 0$ at $x = 0$ at all time instants and is consistent with Equations 4.3 and 4.5. The distal end of the

esophagus, on the other hand, remains open to allow emptying into the stomach. Since the pressure term in Equation 4.2 consists of a single derivative with respect to x, it is necessary to specify only one boundary condition for P. The boundary pressure was specified at the distal end which was equal to a typical value of gastric pressure (7 mmHg). Finally, for initial condition, we had zero velocity at all points along x at $t = 0$.

4.3.3. Cross-sectional area of the lower esophageal sphincter

The low spatial resolution of the dynamic MRI poses a problem of accurately identifying the lower esophageal sphincter (LES) cross-section. This is because the LES opening is narrower compared to the esophageal body and does not distend very much because of the greater wall stiffness at the esophagogastric junction (EGJ). Although this could be improved by focusing the MRI only at the LES, the state of the esophagus proximal to the LES cannot be estimated in such a scenario. The LES can be identified in only one or two time instants when the LES has greatly distended due to a bolus flow through it. Figure 4.4 shows the LES at one such time instant. The LES cross-sectional area measured at this time instant can act as a valuable reference to identify the bolus behavior proximal to the LES.

As specified in the previous section, since pressure is specified as a Dirichlet boundary condition at the distal end of the esophagus, the intrabolus pressure prediction depends on the accurate measurement of the LES cross-sectional area. Figure 4.5 shows the intrabolus pressure calculated using the numerical approach described in Halder et al. [**44**] with different LES cross-sectional areas. The pressure shown is non-dimensional and the pressure at the distal end was specified zero as a reference in this case. The total length of

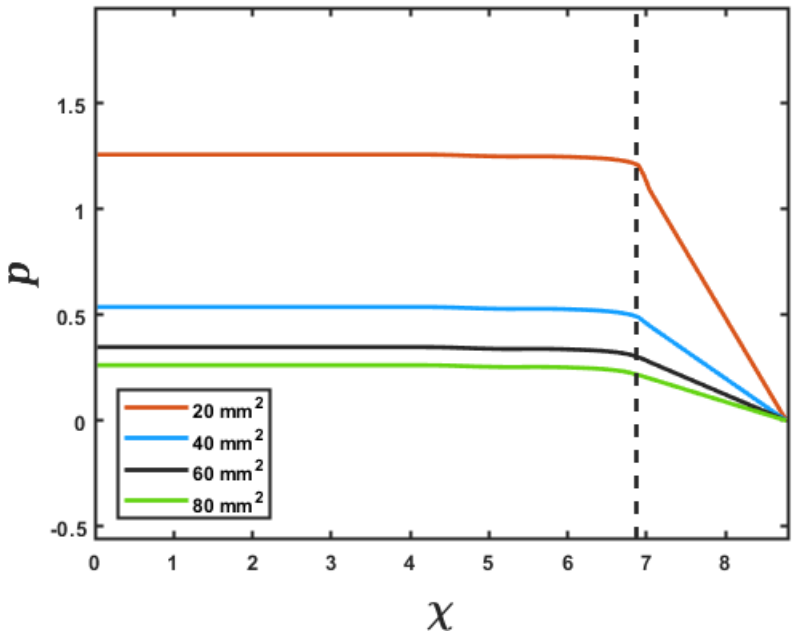

Figure 4.5. The effect of LES cross-sectional area on the prediction of intrabolus pressure. The proximal end of the LES is marked by the vertical dashed line. The inserted legend shows the LES cross-sectional areas used for this simulation. Equations 4.6 and 4.7 were solved using the method described in FluoroMech to calculate the intrabolus pressure. The input for the model was the variation of α observed from the MRI with four reference LES cross-sectional areas. The variation of pressure is shown at a single time instant to illustrate the impact of LES cross-sectional area on pressure prediction.

the esophagus considered here is the sum of the centerline length (9.65 cm) and the LES length (2.78 cm). Thus, the proximal and distal location of the bolus were 9.65 cm and 12.43 cm, respectively. In non-dimensional form, the proximal and distal locations were $\chi_p = 6.87$ and $\chi_L = 8.81$, respectively. The quantities χ_p and χ_L were important locations as described in the next section. As shown in Figure 4.5, the intrabolus pressure proximal to the LES depends on the LES cross-sectional area, so, assuming a constant LES cross-sectional area (measured at one time instant) would lead to an incorrect prediction,

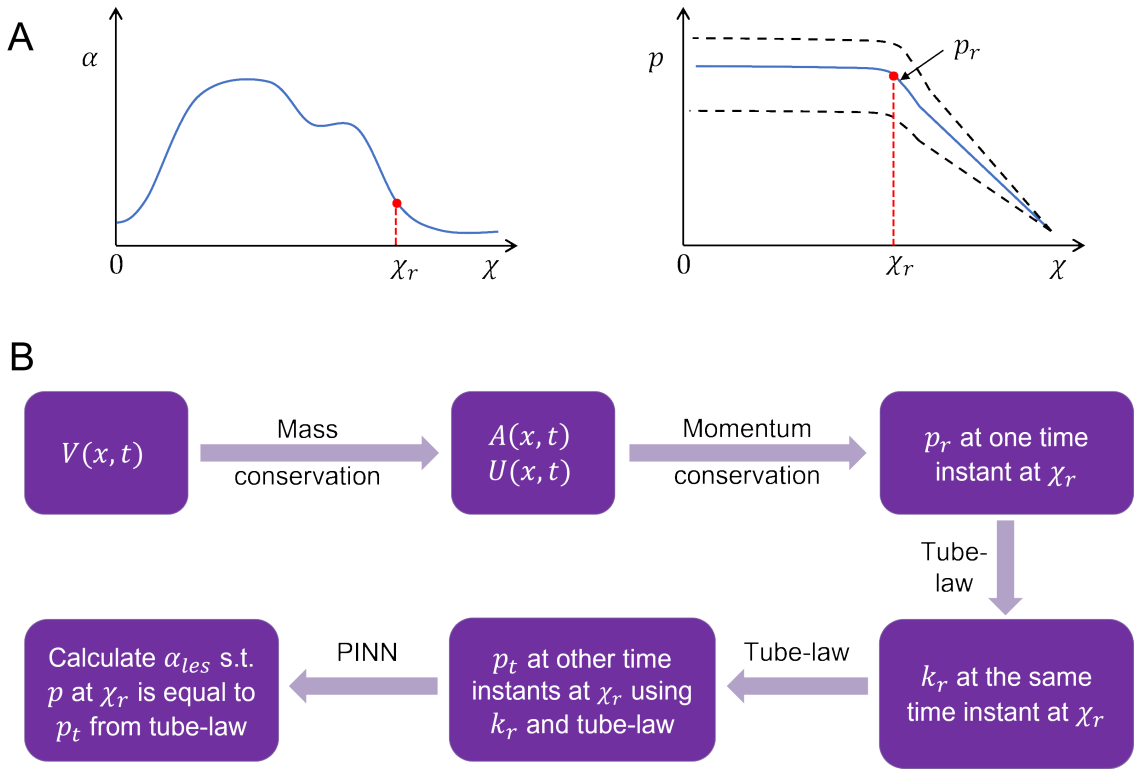

Figure 4.6. Problem definition for the physics informed neural network (PINN) framework. (A) Schematic for the variation of cross-sectional area and pressure at the time instant when the LES cross-section was known. The dashed lines in the pressure variation show what intrabolus pressure would be at other time instants assuming constant LES cross-sectional area. (B) Workflow for the prediction of LES cross-sectional area at other time instants.

making it important to know the instantaneous LES cross-sectional area to accurately predict intrabolus as well as to understand LES functioning during emptying.

4.3.4. Physics-informed neural network

The problem of missing data for the LES cross-sectional area (and consequently obtaining accurate intrabolus pressure values) was solved using a physics-informed neural network (PINN) [**64**]. The problem description is schematically shown in Figure 4.6. The final

interpolated volume $V(x,t)$ was used to calculate $A(x,t)$ and $U(x,t)$ using Equations 4.4 and 4.5, and after non-dimensionalization, $\alpha(\chi,\tau)$ and $u(\chi,\tau)$, respectively. These values of $\alpha(\chi,\tau)$ and $u(\chi,\tau)$ were then used to calculate $p(\chi_r,\tau_r)$ at the specific time instant when the LES cross-section was visible by solving Equation 4.7 using the finite volume method described in Halder et al. [**44**]. The non-dimensional time τ_r corresponds to the time instant when the LES was visible in MRI. The point χ_r was selected near the proximal end of the LES. This point was selected because the pressure at points proximal to χ_r are of similar magnitude as $p(\chi_r,\tau)$ as shown in Figure 4.5. Additionally, χ_r was very close to the LES and hence the effect of active relaxation as observed in the esophageal body was minimal. Note that this was an assumption that we made regarding the active relaxation, and its usefulness will be explained shortly. The values of χ_r and τ_r were 6.76 and 8.57, respectively. The pressure $p(\chi_r,\tau_r)$ was the correct estimate of the intrabolus pressure since the LES cross-sectional area was accurately known. We call this pressure the reference pressure, $p_r = p(\chi_r,\tau_r)$. Using the tube law in Equation 3.7, the stiffness (k_r) at χ_r was calculated as follows:

$$k_r = \frac{p_r}{\left(\frac{\alpha(\chi_r,\tau_r)}{\alpha_o} - 1\right)}. \tag{4.8}$$

Note that there is no θ in Equation 4.8 since we assumed that $\theta = 1$ at χ_r. With the stiffness at χ_r known, we calculated the pressure $p_t = p(\chi_r,\tau)$ at other times with the tube law according to Equation 3.7 as follows:

$$p_t = k_r \left(\frac{\alpha(\chi_r,\tau_r)}{\alpha_o} - 1\right). \tag{4.9}$$

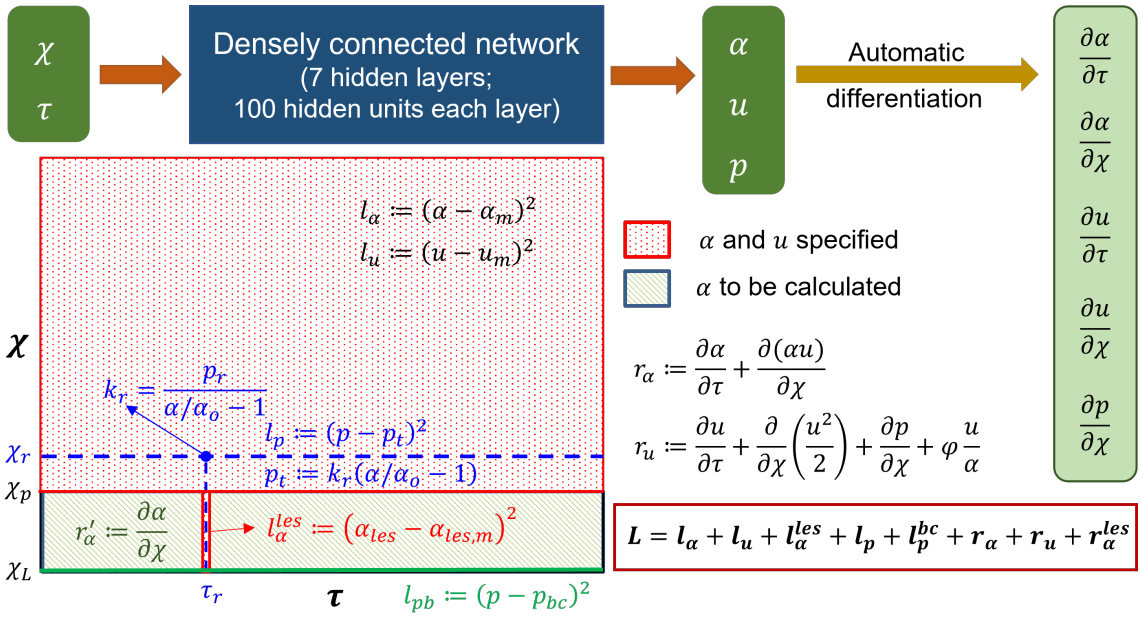

Figure 4.7. Details of the physics-informed neural network (PINN). The input and output of the PINN along with the details of the hidden layers are shown at the top. Automatic differentiation was used to calculate the derivative terms for the residuals. The schematic of the domain is shown below. The schematic describes where the different losses were specified.

The LES cross-sectional area (A_{les}) was calculated using PINN so that the pressure predicted at χ_r matches p_t for all times. An additional constraint is necessary to ensure an unique solution for A_{les} as follows:

$$\frac{\partial \alpha_{les}}{\partial \chi} = 0, \tag{4.10}$$

where $\alpha_{les} = A_{les}/A_s$ is the non-dimensional cross-sectional area of the LES. Equation 4.10 implies that there was no significant variation of LES cross-sectional area along χ. This is physically meaningful since the variation of α_{les} along χ is quite negligible compared to the esophageal body and can be observed in Figure 4.4 as well.

4.3.4.1. Network architecture. The schematic in Figure 4.7 shows the architecture of the PINN. It takes χ and τ as input and predicts α, u, and p. Since the inputs are χ and τ, automatic differentiation can be used effectively to calculate $\frac{\partial \alpha}{\partial \tau}$, $\frac{\partial \alpha}{\partial \chi}$, $\frac{\partial u}{\partial \tau}$, $\frac{\partial u}{\partial \chi}$, and $\frac{\partial p}{\partial \chi}$ which were used for calculating the terms in Equations 4.6 and 4.7. Aside from the input and the output layers, the PINN consisted of 7 hidden layers with 100 hidden units in each layer. We used tanh activation function for every layer.

4.3.4.2. Losses. The losses for the PINN consisted of a combination of measurement losses and residuals of the mass and momentum conservation equations. Minimizing the measurement losses ensures that the solutions are consistent with the measurements, and minimizing the residuals ensures that the governing physics behind the problem is followed. Figure 4.7 shows the locations and time instant at which the different measurement losses and residuals were calculated. As already mentioned in the work-flow, α and u were known at all points proximal to the bolus (marked in red) for all time instants. The measurement losses for α and u for $\chi < \chi_p$ and $0 \leq \tau \leq \tau_T$ were as follows:

$$l_\alpha = \frac{1}{N_1} \sum_{i=1}^{N_1} \left(\alpha^i - \alpha_m^i\right)^2, \tag{4.11}$$

$$l_u = \frac{1}{N_1} \sum_{i=1}^{N_1} \left(u^i - u_m^i\right)^2, \tag{4.12}$$

wherein the quantities with subscript m represent measured quantities. χ_p is the proximal end of the LES and τ_T is the total time (non-dimensional) of bolus transport. Each point i was taken from a Cartesian grid of 99 nodes along τ and 100 nodes along χ, which leads to $N_1 = 9900$. Note that we are calling u_m as a measured quantity for the PINN although we calculate it along with α through the interpolated volume V as

described in the Section 4.1. This is because the PINN minimizes the square of the difference between prediction of α and u from the network with their already known values (which are analogous to measurements for being already known quantities for the PINN). Additionally, the LES cross-sectional area was known at $\tau = \tau_r$ for $\chi_p < \chi \leq \chi_L$ and the corresponding measurement loss was as follows:

$$l_{\alpha}^{les} = \frac{1}{N_2} \sum_{i=1}^{N_2} \left(\alpha_{les}^{i} - \alpha_{les,m}^{i} \right)^2, \tag{4.13}$$

wherein χ_L is the non-dimensional coordinate of the distal end. The points i were taken from a uniform mesh of $N_2 = 28$ points along χ at τ_r. The measurement loss for pressure was calculated at $\chi = \chi_r$ for $\tau \geq 0$ and was defined as follows:

$$l_p = \frac{1}{N_3} \sum_{i=1}^{N_3} \left(p^i - p_t^i \right)^2, \tag{4.14}$$

wherein the points i were selected from a uniform mesh of $N_3 = 98$ along τ at $\chi = \chi_r$. Additionally, the Dirichlet pressure boundary condition was enforced at $\chi = \chi_L$ for $\tau \geq 0$ through the following loss:

$$l_p^{bc} = \frac{1}{N_4} \sum_{i=1}^{N_4} \left(p^i - p_{bc}^i \right)^2, \tag{4.15}$$

wherein p_{bc} is the pressure specified at the distal end of the esophagus and $N_4 = 99$ with i selected from a uniform grid along τ. The residual losses were calculated in the entire

domain for $0 \leq \chi \leq \chi_L$ and $\tau \geq 0$ according to Equations 4.6 and 4.7 as shown below:

$$r_\alpha = \frac{1}{N_5} \sum_{i=1}^{N_5} \left[\frac{\partial \alpha^i}{\partial \tau} + \frac{\partial \left(\alpha^i u^i \right)}{\partial \chi} \right], \tag{4.16}$$

$$r_u = \frac{1}{N_5} \sum_{i=1}^{N_5} \left[\frac{\partial u^i}{\partial \tau} + \frac{\partial}{\partial \chi} \left(\frac{(u^i)^2}{2} \right) + \frac{\partial p^i}{\partial \chi} + \varphi \frac{u^i}{\alpha^i} \right], \tag{4.17}$$

wherein i was randomly sampled from a uniform distribution of points in the entire domain with $N_5 = 50688$. Finally, the constraint as described in Equation 4.10 led to the following residual:

$$r_\alpha^{les} = \frac{1}{N_6} \sum_{i=1}^{N_6} \frac{\partial \alpha_{les}^i}{\partial \chi} = 0, \tag{4.18}$$

wherein i was randomly sampled from a uniform distribution of points in the domain $[\chi_p, \chi_L]$ and $[0, \tau_T]$ with $N_6 = 5544$. The total loss for the PINN was the sum of all the measurement losses and residuals as follows:

$$L = l_\alpha + l_u + l_\alpha^{les} + l_p + l_p^{bc} + r_\alpha + r_u + r_\alpha^{les}. \tag{4.19}$$

To train the network, the inputs χ and τ were normalized with their mean and standard deviation as follows:

$$\chi' = \frac{\chi - \mu_\chi}{\sigma_\chi}, \tag{4.20}$$

$$\tau' = \frac{\tau - \mu_\tau}{\sigma_\tau}, \tag{4.21}$$

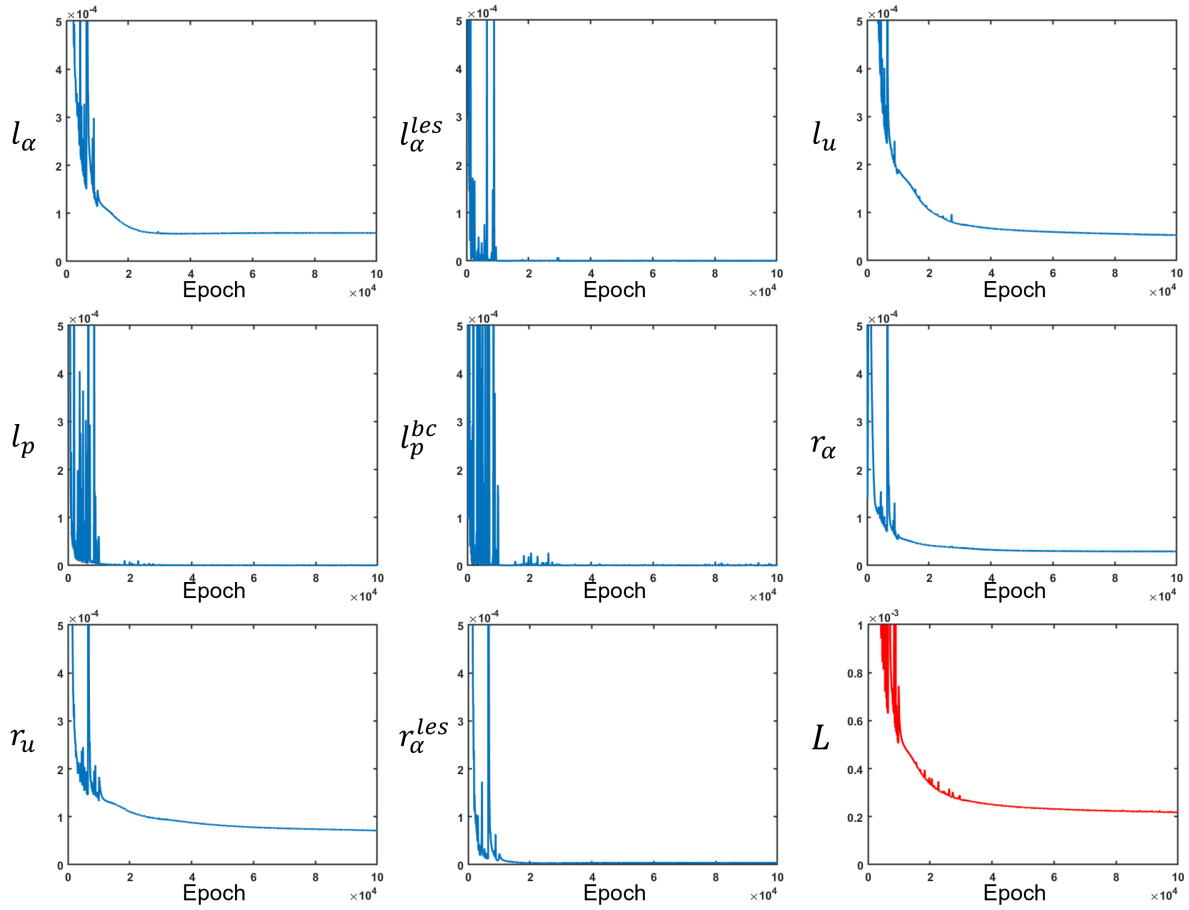

Figure 4.8. Measurement losses and residuals along with the total loss. All loss functions were minimized at different rates. The total loss is depicted in red while the other losses are in blue.

wherein μ and σ are the corresponding mean and standard deviations, respectively for χ and τ. Hence, the derivatives with respect to χ and τ gets modified as follows:

$$\frac{\partial}{\partial \chi}(\cdot) = \frac{1}{\sigma_\chi}\frac{\partial}{\partial \chi'}(\cdot), \tag{4.22}$$

$$\frac{\partial}{\partial \tau}(\cdot) = \frac{1}{\sigma_\tau}\frac{\partial}{\partial \tau'}(\cdot). \tag{4.23}$$

4.3.4.3. Training. The network was trained using Tensorflow [**70**] for 100000 epochs. We used an Adam [**71**] optimizer to minimize the losses. A piecewise constant decayed learning rate was used to minimize the losses efficiently. The learning rate was 0.001 for the first 10000 epochs, 0.0001 for the next 20000 epochs, and 0.00003 for the last 70000 epochs. The final values for l_α, l_u, l_α^{les}, l_p, l_p^{bc}, r_α, r_u, r_α^{les} were 5.9×10^{-5}, 9.8×10^{-7}, 5.3×10^{-5}, 4.0×10^{-7}, 2.7×10^{-7}, 2.9×10^{-5}, 7.2×10^{-5}, and 3.8×10^{-6}, respectively. Figure 4.8 shows the learning curves for the various loss functions. The final total loss was 2.2×10^{-4}.

4.4. Flow variables

The PINN predicts the non-dimensional cross-sectional area, fluid velocity, and fluid pressure by minimizing a set of measurement losses as well as ensuring that the physics of the fluid flow problem is followed throughout. The variation of the predicted cross-sectional area (in its dimensional form) is shown in Figure 4.9a for all values of x and t. The values of the cross-sectional areas inside the bolus proximal to the LES were obtained from measurements and their prediction was based on the minimization the measurement loss as described by Equation 4.11.

The cross-sectional areas proximal to the bolus cannot be visualized in MRI because the fluid contrast media was completely displaced by the peristaltic contraction and the dynamic MR imaging cannot distinguish the esophagus from surrounding tissue. Hence, we assigned the inactive cross-sectional area A_o to the esophagus proximal to the bolus. We found that this assignment does not impact the prediction of any of the physical

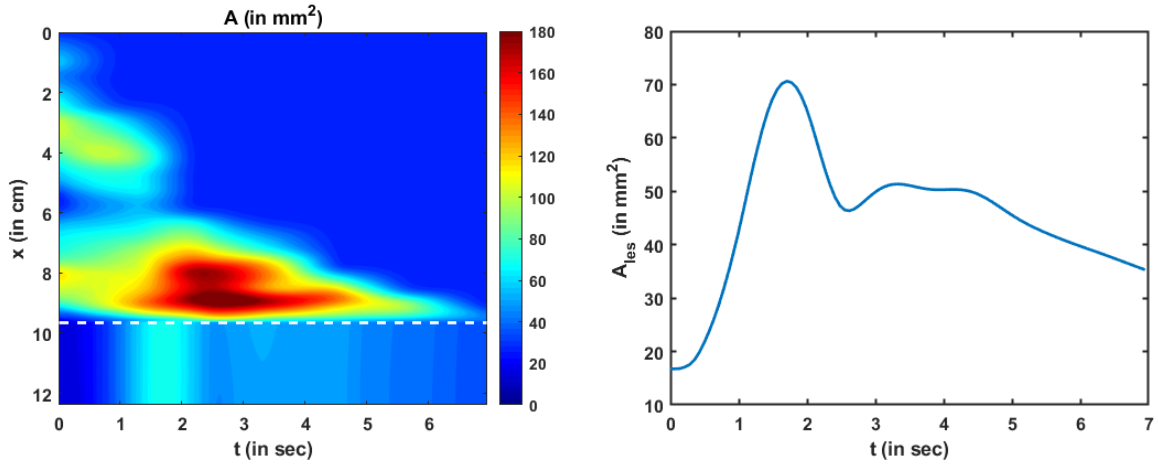

(a) (b)

Figure 4.9. Variation of cross-sectional area as predicted by the PINN. (a) Variation of A as a function of x and t. The dashed white line indicates the proximal end of the LES. The cross-sectional area above the dashed line was known from the MRI and its prediction by the PINN was ensured by minimizing Equation 4.11. There is no variation of A along x within the LES due to the constraint described by Equation 4.10, (b) Variation of the LES cross-sectional area as a function of time. It had the greatest magnitude near the instant that the LES was visible in the MRI.

quantities using PINN. This is because the velocity (and flow rate) proximal to the bolus is automatically predicted as zero (as shown in Figures 4.10a and 4.10b) with this assignment, and since the pressure boundary condition is specified at the distal end, the pressure calculation inside the domain does not depend on the behavior proximal to the bolus. The variation of LES cross-sectional area can be seen below the dashed line in Figure 4.9a. The LES cross-sectional area does not vary along x and only varies along t. This is because we enforced the constraint as described in Equation 4.10.

The variation of the LES cross-sectional area is shown more clearly in Figure 4.9b. The prediction of A_{les} depends on the reference LES cross-sectional area observed at a single time instant, the conservation laws, and the reference pressure prediction at χ_r.

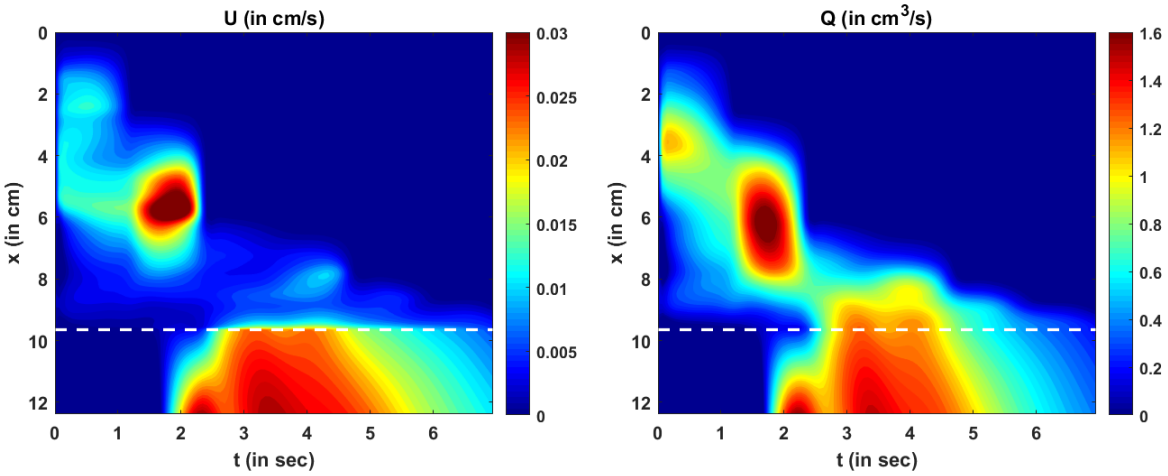

(a) (b)

Figure 4.10. Variation of velocity and flow rate. (a) Variation of U as predicted by the PINN. There are two high velocity zones: one at x 6 cm, $t = 2$ s and the other at the LES for $t > 2$ s. These high velocity zones match the regions of low cross-sectional areas: (b) Variation of the mean flow rate calculated as $Q = AU$. The high flow rate matches the high velocity zones, but there is a smoother transition of Q at the proximal end of the LES compared to U.

A_{les} has the greatest magnitude near the instant when the LES cross-sectional area was observed in the MRI and has lesser values farther away from that instant. This matches our observation from the MRI images that the LES could not be visualized most of the time. Hence, since the effectiveness of esophageal transport essentially depends on how effectively the esophagus empties, the LES cross-sectional area is an important physiomarker of esophageal function. Greater LES cross-sectional area facilitates esophageal emptying while it is becomes unnecessary for the LES to have large cross-sectional area when the bolus has almost completely emptied. Similar LES behavior is evident in Figure 4.9b where it was greater during the emptying process and minimal when bolus emptying was nearly complete.

The variation of bolus fluid velocity and flow rate are shown in Figures 4.10a and 4.10b, respectively. It can be seen that there are two major high-velocity zones. The first high-velocity zone is near $x = 6$ cm and $t = 2$ sec. Comparing this region with the Figure 4.9a it is evident that the cross-sectional area at that location and time was less than at its adjacent regions. The second high-velocity zone was in the LES. This corresponds to low cross-sectional area as well. Thus, the velocities are greater at lower cross-sectional areas which is intuitive for low viscosity fluids. The flow rate is the rate at which the bolus is emptied out of the esophagus and zones with high flow rate are similar to those with high-velocity. However, there is a smoother transition of flow rate from the esophageal body to the LES compared to the velocity field. This is because the LES cross-sectional area was much smaller than that of the esophageal body requiring that the fluid velocity needed to increase more to maintain the same flow rate.

The variation of fluid pressure is shown in Figure 4.11. The pressure gradients along x drives the fluid through the esophagus. On comparing Figures 4.10a and 4.11, we can see that the high-pressure gradients match the high-velocity zones. This is because the high-pressure gradients locally accelerate the fluid. Note that the pressure variations are minimal compared to the magnitudes of the pressure. An intragastric pressure of 7 mmHg was used as a boundary condition for pressure at the distal end which is in the normal range for a healthy subject. The thoracic pressure was assumed to be 0 mmHg. Thus, the intrabolus pressure must be greater than the intragastric pressure to empty into the stomach. The major portion of this pressure ($\sim$7 mmHg) is developed by the elastic distention of the esophageal walls. A small portion of the total intrabolus pressure ($\sim$0.01 mmHg) is attributable to the local acceleration or deceleration of the bolus fluid. Since

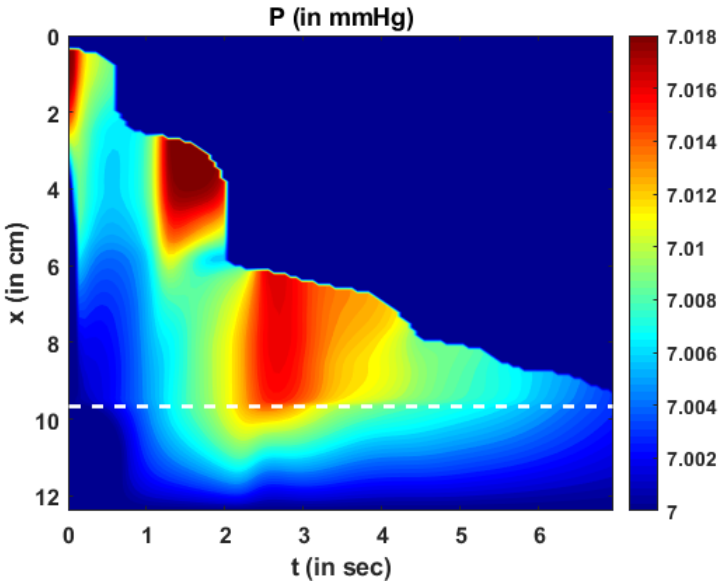

Figure 4.11. Variation of pressure as a function of x and t. Two major high-pressure zones can be identified wherein the fluid locally accelerates, making the corresponding fluid velocity greater in those regions. Note that the magnitude of dynamic pressure variations are minimal compared to the total pressure.

the MRI shows only the movement within an already distended esophagus, the calculated pressure variations are minimal and correspond to local acceleration or deceleration of the fluid. This observation regarding dynamic pressure variations was also observed in mechanics-based analysis of fluoroscopy [**44**].

The total intrabolus pressure as shown in Figure 4.11 is within the normal range according to CCv4.0, leading us to conclude that our specifications of the intragastric pressure and thoracic pressure were valid. The prediction of A_{les} depends on the pressure gradients and not the actual magnitude of pressure. Therefore, the prediction of A_{les} remains the same irrespective of the boundary condition chosen for P. Figures 4.9b, 4.10a, 4.10b, and 4.11 also point at an important feature of the LES. The greatest LES

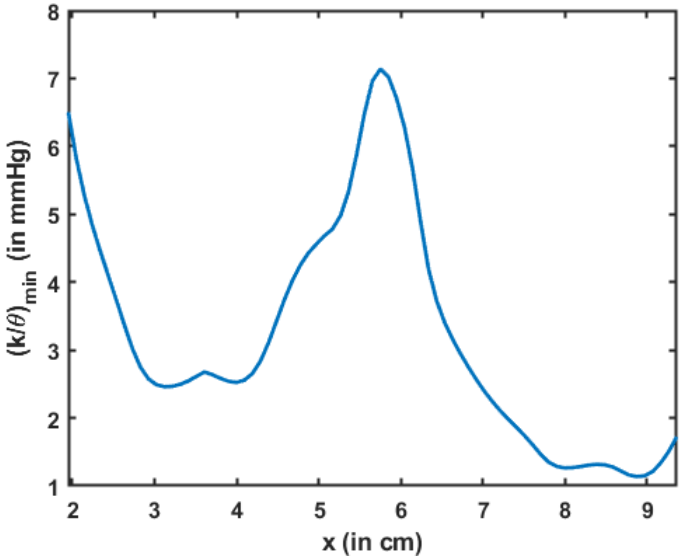

Figure 4.12. Variation of the minimum esophageal wall stiffness along the length of the esophagus. This measure of stiffness accounts for active relaxation and captures the wall characteristics when the esophagus was distended. The stiffness is shown only for the esophageal body proximal to the LES.

cross-sectional area (at approximately 1.8 s) neither match the greatest pressure nor the greatest velocity (or flow rate) across the LES. This demonstrates that the LES opening is not governed passively by intrabolus pressure. If the LES was passively opened by elastic distention due to the intrabolus pressure, then the maximum LES cross-sectional area would coincide with the maximum pressure gradient. Since that is not observed, it can be concluded that the LES cross-sectional area also involves neuromuscular relaxation.

4.5. Wall stiffness and active relaxation

The esophageal wall stiffness and active relaxation were calculated as described in chapter 3. Esophageal wall stiffness (along with the effect of active relaxation) was estimated by the parameter K/θ, which the dimensional form of the quantity k/θ described

by Equation 3.21, where $K = \rho c^2 k$. The minimum value of K/θ corresponds to the lower bound of the effective stiffness of the esophageal walls when distended. Since the cross-sectional area of the esophagus is not visible in MRI, any prediction regarding the stiffness at those locations would be inaccurate. Hence, predictions of wall stiffness can only be made at regions where the esophagus is distended i.e., at the location of the bolus. However, the distended esophageal walls also undergo active relaxation to accommodate an incoming bolus as well as minimize intrabolus pressure. The combined behavior of the passive elastic distention of the esophageal walls and active relaxation is captured by the parameter K/θ. Since K/θ estimates the lower bound of the effective esophageal stiffness, the most accurate estimate of K/θ occurs when the esophageal walls are most distended. The maximum distension corresponds to the minimum value of K/θ, which is shown in Figure 4.12. The minimum K/θ at each x was calculated for all values of t. Note that the high value of $(K/\theta)_{min}$ near $x = 6$ cm in Figure 4.12 matches with the low cross-sectional area region in Figure 4.9a. This makes sense because the esophagus would distend less at locations of greater stiffness. It should be noted that although the stiffness appears high at $x = 6$ cm, it is does not necessarily mean that the esophageal tissue is stiffer at that location. When the esophageal wall comes in contact with surrounding organs, it appears stiffer due to the effect of those organs on the esophagus. Since, all calculations are made using only bolus geometry, it is impossible to distinguish the effect of other organs outside the esophagus. Hence, we hypothesize that the lower values of $(K/\theta)_{min}$ estimate the true stiffness of the esophageal walls and the greater value of $(K/\theta)_{min}$ near $x = 2$ cm is likely a composite measure partly attributable to extrinsic compression. Close to the advancing peristaltic contraction, $\theta < 1$ so, $(K/\theta)_{min}$ takes a greater value and the esophagus seems

to be locally stiffer. Also, note that we have not included the EGJ in Figure 4.12. This is because we did not define the problem with the tube law applied at the EGJ because applying the tube law at the EGJ would not result in a unique solution. The mechanical properties of the esophageal walls have been estimated experimentally in Orvar et al. [**62**], Patel and Rao [**63**], and Kwiatek et al. [**59**]. In those studies, the esophagus was distended and the cross-sectional area and the pressure developed inside were recorded. A straight line was fitted to quantify the linear relationship between cross-sectional area and pressure in an inactive esophagus. The slope of the line measured the quantity A_o/K which was in the range 9.1-11.6 mm^2/mmHg. Using the typical range of A_o as described in Xia et al. [**61**], i.e. $7-59$ mm^2, the stiffness of the esophageal walls was found to lie in the range $0.6-6.5$ mmHg. The effective stiffness as shown in Figure 4.12 lay in the range $1-7$ mmHg, which is of the same order of magnitude as observed in the other studies.

The parameter θ quantifies the amount of active relaxation of the esophageal walls to facilitate distention, and consequently, decrease the local intrabolus pressure and increase the flow rate. The variation of the active relaxation parameter θ is shown in Figure 4.13. As described by Equation 3.18 and comparing Figure 4.13 and 4.9a, it is evident that the locations of the high values of θ match the location of the high values of A, and, similarly lower values of θ match the lower values of A. Note that θ quantifies the active relaxation in the esophageal body and not the LES. Comparing Figures 4.12 and 4.13 shows that locations of greater stiffness correspond to locations of lower active relaxation and vice-versa. Similar to $(K/\theta)_{min}$ as described above, the impact of tissues and organs outside the esophagus impacts the prediction of θ as well. Hence, the low value of θ near $x = 6$ cm does not necessarily mean a lack of active relaxation, but most likely the influence of

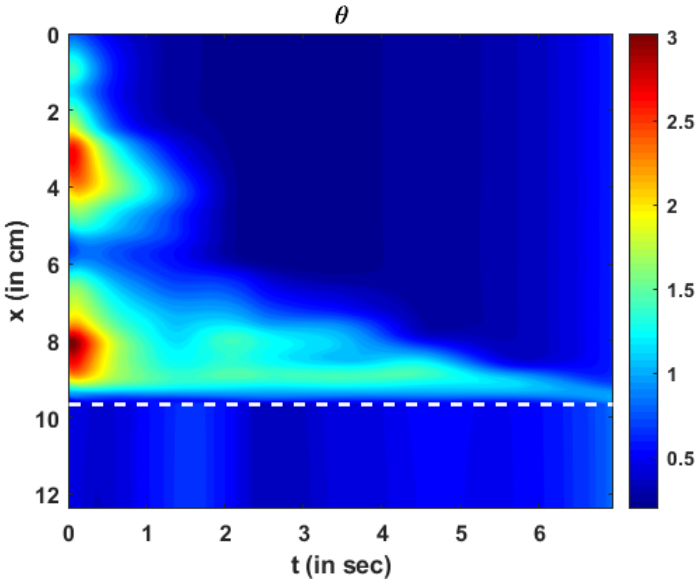

Figure 4.13. Variation of active relaxation as a function of x and t. The dashed line corresponds to the proximal end of the LES. Since the tube law was not specified at the LES, the active relaxation is meaningful only in the esophageal body (above the dashed line).

structures outside the esophagus. Hence, we hypothesize that the greater values of active relaxation are closer to the actual active relaxation of the esophageal walls.

Although MRI-MECH provides valuable insights about the nature of transport and the mechanical state of the esophagus, it has limitations. Currently, manual segmentation of the bolus geometry is more accurate and is reasonable for a low temporal resolution of the dynamic MRI, but can become tedious with improved temporal resolution. Automatic segmentation using deep learning techniques might be helpful in that aspect, but also increases the risk of inaccurate segmentation without a large training dataset. Bolus transport as visualized in MRI provides no information proximal to the bolus (a similar problem occurs in fluoroscopy as well). Hence, the MRI-MECH cannot predict anything meaningful proximal to the bolus. Thus, MRI-MECH cannot be used to estimate the

contraction strength, for which other diagnostic techniques should be used such as HRM or FLIP. The esophageal wall properties and neurally-activated relaxation were estimated solely through the bolus shape and movement. But the bolus shape and movement depend not only on the esophageal walls but also on the impact of organs surrounding the esophagus. This is a limitation of the MRI-MECH framework in the predicting the state and functioning of the esophagus due to lack of information about the impact of the surrounding organs. Finally, the prediction of intrabolus pressure and the esophageal wall stiffness depends on the specification of the correct intragastric pressure. This becomes a limitation for MRI-MECH since the intragastric pressure is not known in the MRI, and so, we used a reference value from literature. Accurate measurement of the intragastric pressure through other diagnostic techniques such as HRM will increase the accuracy of the MRI-MECH predictions of intrabolus pressure and wall stiffness.

4.6. Conclusion

We presented a framework called MRI-MECH that uses dynamic MRI of a swallowed fluid to quantitatively estimate the mechanical health of the esophagus. The bolus geometry, which tracks the inner cross-section of the esophagus, was extracted through manual segmentation of the MR image sequence and was used as input to the MRI-MECH framework. MRI-MECH modeled the esophagus as a one-dimensional flexible tube and used a physics-informed neural network (PINN) to predict the fluid velocity, intrabolus pressure, esophageal wall stiffness, and active relaxation. The PINN minimized a set of measurement losses to ensure that the predicted quantities matched the measured quantities, and a set of residuals to ensure that the physics of the fluid flow problem was followed,

specifically, the mass and momentum conservation equation in one-dimension. The LES cross-sectional area is very difficult to visualize in MRI because it is significantly smaller than the cross-sectional area at the esophageal body. In this regard, MRI-MECH enhances the capability of the dynamic MRI by calculating the LES cross-sectional area during the esophageal emptying. We found that our predictions of the intrabolus pressure and the esophageal wall stiffness match those reported in other experimental studies. Additionally, we showed that the dynamic pressure variations that occur because of local acceleration/deceleration of the fluid were negligible compared to the total intrabolus pressure, whose main contribution was the elastic deformation of the esophageal walls. The mechanics-based analysis with detailed three-dimensional visualization of the bolus in MRI leads to significantly better prediction of the state of the esophagus compared to two-dimensional X-ray imaging such as esophagram and fluoroscopy, and can be easily extended to other medical imaging techniques such as computerized tomography (CT). Thus, MRI-MECH provides a new direction in mechanics-based non-invasive diagnostics that can potentially lead to improved clinical diagnosis.

CHAPTER 5

Virtual disease landscape using mechanics-informed variational autoencoder: application to esophageal disorders

High resolution manometry (HRM) widely used test for evaluating esophageal dysphagia is high-resolution manometry [**6, 7, 9, 8, 10**]. HRM measures swallow-induced pressures at multiple sites within the esophageal lumen including the esophagogastric junction (EGJ) to make clinical diagnoses according to the Chicago Classification v4.0 (CCv4.0) [**13**], the current worldwide standard classification of esophageal motility disorders. A newer technology for investigating esophageal motility is the functional luminal imaging probe (FLIP) [**11, 12**] which assesses the response of the esophagus to distention. Figure 5.1 is a schematic diagram of the FLIP probe incorporating 16 impedance planimetry sensors to measure esophageal luminal cross-sectional area and a pressure sensor at its distal end. The sensors are housed within a compliant bag that is incrementally filled with saline. During measurements, the FLIP probe is passed trans-orally and positioned across the EGJ. Distending the esophagus with the FLIP bag normally induces a contractile response including periods of repetitive antegrade contractions (RACs), but alternative patterns (or no contractile response) can be seen in patients with esophageal motility disorders or other disease states [**14**]. Compared to HRM, which evaluates primary peristalsis, FLIP evaluates secondary peristalsis which is physiologically different. Carlson et al. [**72**] have shown that subjects with normal esophageal motility on HRM

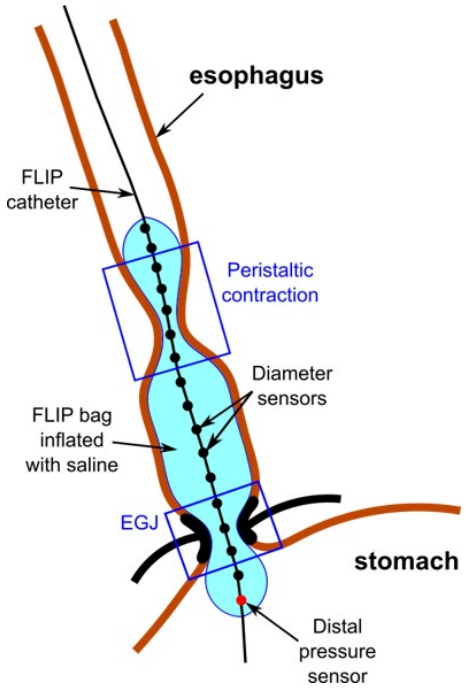

Figure 5.1. Schematic diagram of the FLIP probe. The secondary peristaltic contraction and EGJ tone are evident inside the blue boxes. EGJ tone results from a complex interaction between the lower esophageal sphincter and the crural diaphragm.

exhibit abnormal EGJ opening with FLIP. Other studies [**62, 59**] have also shown that, unlike other diagnostic tests, FLIP can be used to estimate the in-vivo mechanical properties of the esophageal wall. Savarino et al. [**73**] and Carlson [**74**] have published reviews of the clinical applicability of FLIP. Additionally, FLIP has been shown to be used intraoperatively [**75, 76**] during endoscopic or laparoscopic myotomy to calibrate the procedure.

In this chapter, we present a framework that works with FLIP measurements to characterize esophageal function. We used the pressure and diameter data obtained from FLIP to calculate mechanics-based parameters such as esophageal wall properties, muscle contraction strength, EGJ tone, and active relaxation of the esophageal musculature. Esophageal

biomechanics have been extensively studied using both experimental [**14, 16, 18, 15, 36**] and computational [**23, 19, 22, 4, 5, 44, 20, 21, 36, 77**] approaches. For this analysis, we used the mathematical framework as described in Halder et. al. [**44**] to calculate the mechanics-based parameters since it worked with clinical fluoroscopy data obtained from the esophagus and makes rapid predictions with limited computational resources.

The mechanics-based parameters estimate the mechanical "health" of the esophagus in a patient-specific manner. However, identifying unique patterns in these parameters for specific esophageal disorders is challenging, especially with parameters that are functions of both time and location along the esophagus. It is also important that the methodology adjust to errors in the FLIP device operation such as probe positioning and potential discrepancies introduced by human input such as manually specifying values for mechanics-based parameters. This is analogous to manually identifying landmarks on pressure topography plots during the interpretation of HRM studies. This challenging task is tackled using machine learning which has been widely applied in medical diagnosis [**78, 79, 80, 81, 82, 83, 84, 85, 86**]. Machine learning techniques have been used both for medical image analysis and raw patient data analysis. In gastroenterology, machine learning has been used mainly for image segmentation and classification tasks [**87, 87, 88, 89**]. The exception is a recent study [**90**] demonstrating the use of a variational autoencoder (VAE) [**91**] to identify contractility patterns from raw HRM data. The clusters generated in the latent space of the VAE categorized the raw HRM data into patient groups corresponding to specific motility disorders. However, although the data clusters were beneficial for diagnosis, they do not have a discrete physical meaning. In this work, we present a novel framework, called mechanics-informed variational autoencoder

(MI-VAE), which forms clusters in a parameter space corresponding to specific esophageal disorders and these clusters do have physical meaning because they were generated from mechanics-based parameters. We call this parameter space the Virtual Disease Landscape (VDL).

5.1. Mechanics model

Distention of the FLIP probe usually elicits esophageal contractions that its sensors characterize by variations of cross-sectional area along the distal 10-13 cm of the esophagus (including the EGJ) and pressure within the probe measured at its distal end. Using these outputs, we estimated the mechanical "health" of the esophagus and identified patterns of output observed with esophageal motility disorders and other esophageal diseases. This was done in two steps: 1) using an inverse model to estimate the mechanical "health" of the esophagus by calculating parameters such as esophageal wall properties, contraction strength, and active relaxation and 2) using the calculated mechanics-based parameters as input to a VAE which generates the VDL in the form of its latent space. The next two sections discuss these steps in details.

Figure 5.2 illustrates output from a normal FLIP study during a period of RACs as the distention volume is incrementally increased at about 30 second intervals. With a RAC pattern, repetitive antegrade contractions are observed at a frequency of 6 ± 3 per minute. Each antegrade contraction leads to a rise in bag pressure (red tracing in Figure 5.2a). Output from the 16 impedance planimetry sensors are displayed as an iso-area topography plot in Figure 5.2b by interpolating data between sensors. The deep red band

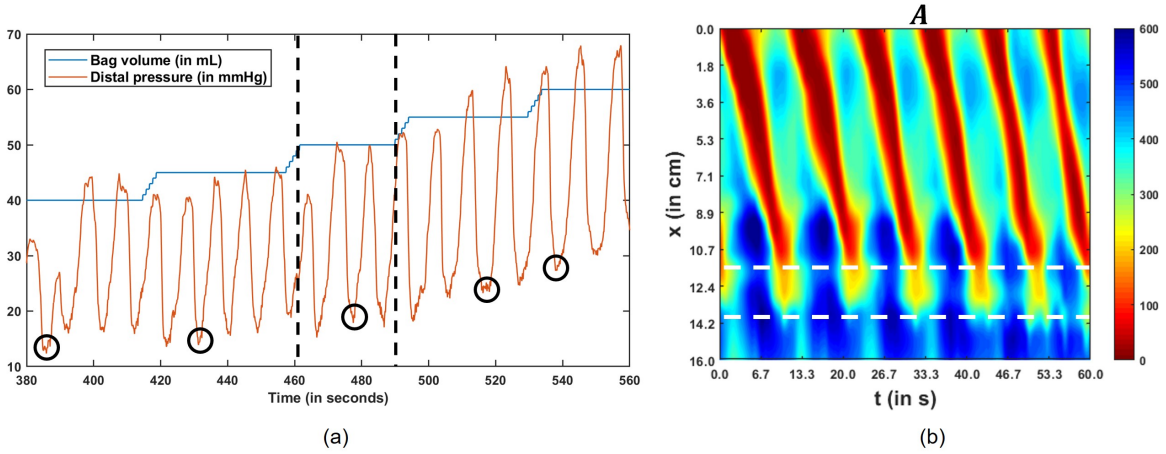

Figure 5.2. Example of graphical output from a normal FLIP study. (a) Bag volume and pressure in the FLIP probe. The pressure variations are caused by antegrade contractions. The black circles indicate minimum distal pressure at each fill volume. These low-pressure points are assumed to correspond to $\theta \sim 1$, (b) Iso-area contour plot of cross-sectional area data for the time interval delineated by the dashed lines in (a). The EGJ is located between the dashed white lines. It is seen to distend as the contraction moves from the proximal to the distal end of the FLIP probe.

in Figure 5.2b is an antegrade contraction which is associated with an increase in cross-sectional area at the EGJ shown by the blue region near the distal end. Note that since FLIP output is of cross-sectional area there is no information regarding the actual three-dimensional geometry of the esophageal lumen. Hence, for simplicity and to conserve computational resources we modeled the FLIP as a one-dimensional flexible tube.

5.1.1. Governing equations

The flow inside the FLIP (modeled as a one-dimensional flexible tube) followed the mass and momentum conservation equation as described by Equations 4.1 and 4.2, respectively. We also used the pressure tube law described by Equation 3.3 since the fluid pressure inside the esophagus has been found to be linearly proportional to its cross-sectional area

[**62, 59**]. Equations 4.1 and 4.2 were non-dimensionalized as follows:

$$\frac{\partial \alpha}{\partial \tau} + \frac{\partial q}{\partial \chi} = 0, \tag{5.1}$$

$$\frac{\partial q}{\partial \tau} + \frac{\partial}{\partial \chi}\left(\frac{q^2}{2}\right) + \alpha \frac{\partial}{\partial \chi}\left(\frac{\alpha}{\theta}\right) + \varphi \frac{q}{\alpha} = 0, \tag{5.2}$$

wherein $\chi = x/L$, $\tau = ct/L$, $q = Q/A_s c$, $p = P/K$, $A_s = \rho c^2 A_o/K$, and $\varphi = 8\pi\mu LK/\rho^2 c^3 A_o$. Equation 3.3 was used to replace P in Equation 4.2 and non-dimensionalized to obtain Equation 5.2. The velocity scale c was taken to be 3 cm /s which is typically the speed of a peristaltic contraction. The ratio K/A_o can be considered as a measure of the stiffness of the esophageal walls.

Since the FLIP is closed at its two ends, it is necessary to enforce zero flow rate boundary conditions at $\chi = 0$ and $\chi = 1$. Since Equation 5.1 requires only one boundary condition for q, we differentiate it with respect to χ to obtain a second order form as follows:

$$\frac{\partial^2 \alpha}{\partial \tau \partial \chi} + \frac{\partial^2 q}{\partial \chi^2} = 0. \tag{5.3}$$

We do the same for Equation 5.2 to specify a Dirichlet boundary condition for pressure at the distal end (as measured by the pressure sensor) and zero pressure gradient at the proximal end as typically observed in practice. Equation 5.2 takes the following form after differentiating with respect to χ:

$$\frac{\partial^2 q}{\partial \tau \partial \chi} + \frac{\partial^2}{\partial \chi^2}\left(\frac{q^2}{\alpha}\right) + \frac{\partial}{\partial \chi}\left(\alpha \frac{\partial}{\partial \chi}\left(\frac{\alpha}{\theta}\right)\right) + \frac{\partial}{\partial \chi}\left(\varphi \frac{q}{\alpha}\right) = 0. \tag{5.4}$$

Equations 5.3 and 5.4 are solved using the finite volume method as described in chapter 2 to solve for q and α/θ. Note that α and θ were grouped here for simplicity. Onceα/θ is known, calculating θ is straightforward with the known values of α. During operation, the FLIP probe is a flexible tube closed at both ends. Since Equations 5.3 and 5.4 are second-order in χ, we need two boundary conditions for q and α/θ at $\chi = 0$ and $\chi = 1$. Additionally, we need one initial condition for q since Equation 5.4 is first-order in τ. At $\tau = 0$, we specified $q = 0$ for all χ. Since the two ends of the FLIP bag are closed, $q = 0$ at $\chi = 0$ and $\chi = 1$. Additionally, with the distal pressure (P_d), $P = P_d(t)$ at $\chi = 1$. Therefore at $\chi = 1$, the corresponding value of α/θ is $(P_d - (P_o - K))/(\rho c^2)$. At $\chi = 0$, we specified $\frac{\partial}{\partial \chi}\left(\frac{\alpha}{\theta}\right) = 0$. This follows directly from Equation 5.2 since $q = 0$ at $\chi = 0$ for all values of τ.

5.1.2. Calculation of mechanics-based parameters

Solving Equations 5.3 and 5.4 requires the knowledge of the parameters K/A_o and $P_o - K$ in a patient-specific manner. They were calculated using the approach as described in Acharya et al. [**77**]. As described in Equation 3.3, P and A are linearly proportional to each other. Thus, in a scenario where the esophagus is inactive (which corresponds to $\theta = 1$) and distended, a plot of P vs. A should be a straight line with its slope and intercept as K/A_o and $P_o - K$, respectively. This inactive but distended esophagus would take the shape of a cylinder with a reference cross-sectional area A_r as follows:

$$A_r = \frac{V}{L}, \tag{5.5}$$

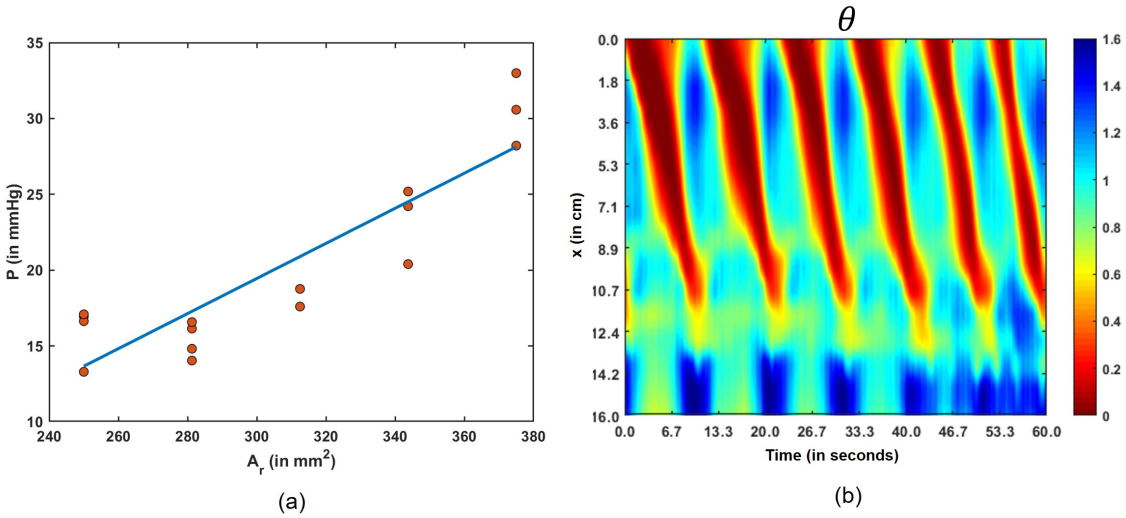

Figure 5.3. Mechanics-based parameters. (a) The variation FLIP pressure with the reference cross-sectional area. The slope and y-intercept of the fitted line yield K/A_o and $P_o - K$, respectively. (b) Variation of the activation parameter corresponding to the cross-sectional area variation shown in Figure 5.2(b).

wherein V is the FLIP bag volume and L is the length of the FLIP. A_r is the cross-sectional area of the FLIP bag when it takes the shape of a perfect cylinder. However, identifying the corresponding pressure inside the esophagus may not be as straightforward. Usually, the time instants at which the distal pressure (P_d) readings are the lowest values for every bag volume, correspond to the time instants when it is reasonable to assume $\theta \sim 1$ as shown in Figure 5.2(a). We selected these pressures readings and the corresponding reference cross-sectional areas A_r and fitted a straight line between them, and the slope and intercept of this line estimated K/A_o and $P_o - K$, respectively as shown by Figure 5.3(a). Note that there is only one value for A_r for each bag volume but multiple pressure readings based on the time instant at which the pressure was considered. This is why there is a vertical spread of data in Figure 5.3(a) for each value of A_r. With K/A_o known, we

calculated the scaling cross-sectional area A_s and the viscosity parameter φ in Equation 5.4. With $(P_o - K)$ known, and P_d known at the distal end, we calculated the boundary condition for α/θ as described above.

5.1.3. Physical significance of the mechanics-based parameters

In summary, there are seven primary mechanics-based parameters: a measure of stiffness (K/A_o), an estimate of the external pressure $(P_o - K)$, the maximum distal pressure recorded during the selected time interval of interest (P_{max}), the time duration of measuremet at constant volumetric distention (T), FLIP bag volume (V), and the contraction and relaxation pattern described through the activation parameter $(\theta(x,t))$. The parameters K/A_o and $P_o - K$ were calculated in a patient-specific manner and had a single value for each patient, while the other parameters had different values for each patient based on the time interval of data considered. The parameter K/A_o estimates the mechanical properties of the esophagus and helps in identifying the relation between the wall properties with the esophageal function. The parameter $P_o - K$ quantifies the state outside the esophagus. The maximum distal pressure P_{max} is the net effect of the contraction strength and EGJ tone, and hence is an important parameter in estimating esophageal motility. The parameter T indirectly estimates the repetitive nature of antegrade contractions since the number of antegrade contractions will be lower for low T and vice-versa, thus estimating an important feature of the esophageal function. The bag volume V controls the extent to which the esophagus is distended which impacts on the passive behavior of the esophageal walls. The activation parameter estimates the contraction strength and pattern, the EGJ tone, and the active relaxation of the esophageal walls.

The activation parameter essentially drives the mechanics of esophageal transport and in the context of the FLIP, it helps estimate esophageal contractility. Active relaxation can be estimated through the maximum value of θ, θ_{max}, which was considered as another primary mechanics-based parameter because active relaxation aids in bolus transport and EGJ relaxation. We call these parameters primary since they completely define the mechanical state of the esophagus, and other mechanics-based parameters can be calculated using combinations of them.

5.2. Mechanics-informed variational autoencoder

The mechanics-based parameters calculated by the 1D inverse model yield a quantitative estimate of the mechanical "health" of the esophagus through the wall mechanical properties and esophageal contractility. Identifying similarities and dissimilarities of these parameters across patient groups is a crucial step in the development of the VDL. This was done in an unsupervised manner with the help of a VAE. Since this neural network works entirely on the mechanics-based parameters, we call it the mechanics informed variational autoencoder (MI-VAE).

5.2.1. Network Architecture

The mechanics-based parameters are as follows: $\theta(x,t)$, K/A_o, $P_o - K$, $P_{\max}$, T, V, and $\theta_{\max}$. These are all scalar values except θ, which varies with x and t so simple statistics can be used to identify patterns of these quantities. However, identifying patterns quantitatively with the activation parameter θ, which describes the esophageal contractility, requires a different approach. Since the variation of θ takes the form of a matrix, as shown

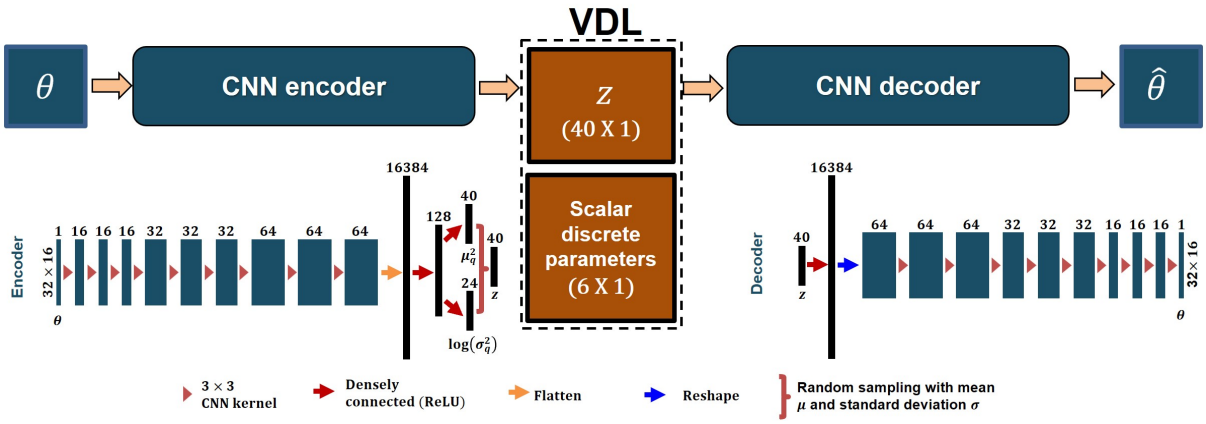

Figure 5.4. Network architecture of the mechanics-informed variational autoencoder. The numbers on the top of the boxes represent the number of channels; the numbers and the output size are represented on the side.

in Figure 5.3b, we used a convolutional neural network-based VAE to identify the unique patterns of disordered contractility through the generated latent space.

We used a latent space of 40 dimensions in order to generate the input with reasonable accuracy. We used ReLU as the activation function for all layers of the MI-VAE. Additionally, we merged a 6-dimensional vector consisting of a set of discrete parameters to the 40-dimensional vectors generated in the latent space. Combined, these 46-dimensional vectors populate a parameter space that forms the VDL. The details of the network architecture are shown in Figure 5.4.

5.2.2. Data

FLIP data used to train the MI-VAE were collected from a cohort of 740 volunteer subjects and patients, the details of which are provided in Table 1. 721 of these subjects underwent both FLIP and manometry. These subjects were classified into 4 groups according to the FLIP-based classification [**92**] which are normal, weak, obstruction, and spastic-reactive

Table 5.1. Details of subjects used to train the MI-VAE

FLIP motility classification	
Category	**Number of subjects**
Normal	221
Weak	51
Obstruction	245
Spastic-reactive	77
Inconclusive	146
Chicago classification v4.0	
Category	**Number of subjects**
Type I achalasia	55
Type II achalasia	129
Type III achalasia	40
EGJ outflow obstruction (EGJOO)	19
Hypercontractile esophagus (HC)	13
Distal esophageal spasm (DES)	12
Ineffective esophageal motility (IEM)	50
Absent contractility (AC)	135
Normal	251
Inconclusive	135

based on the contractile response and EGJ opening. The normal group exhibits distinct antegrade contractions (ideally ≥ 6 consecutive antegrade contractions per minute) and normal EGJ opening. The weak group exhibits non-distinct antegrade contractions or absent contractile activity and normal EGJ opening while the obstruction group exhibit non-distinct antegrade contractions or absent contractile activity and reduced EGJ opening. Spastic-reactive is a broad group that exhibits sustained occluding contractions or

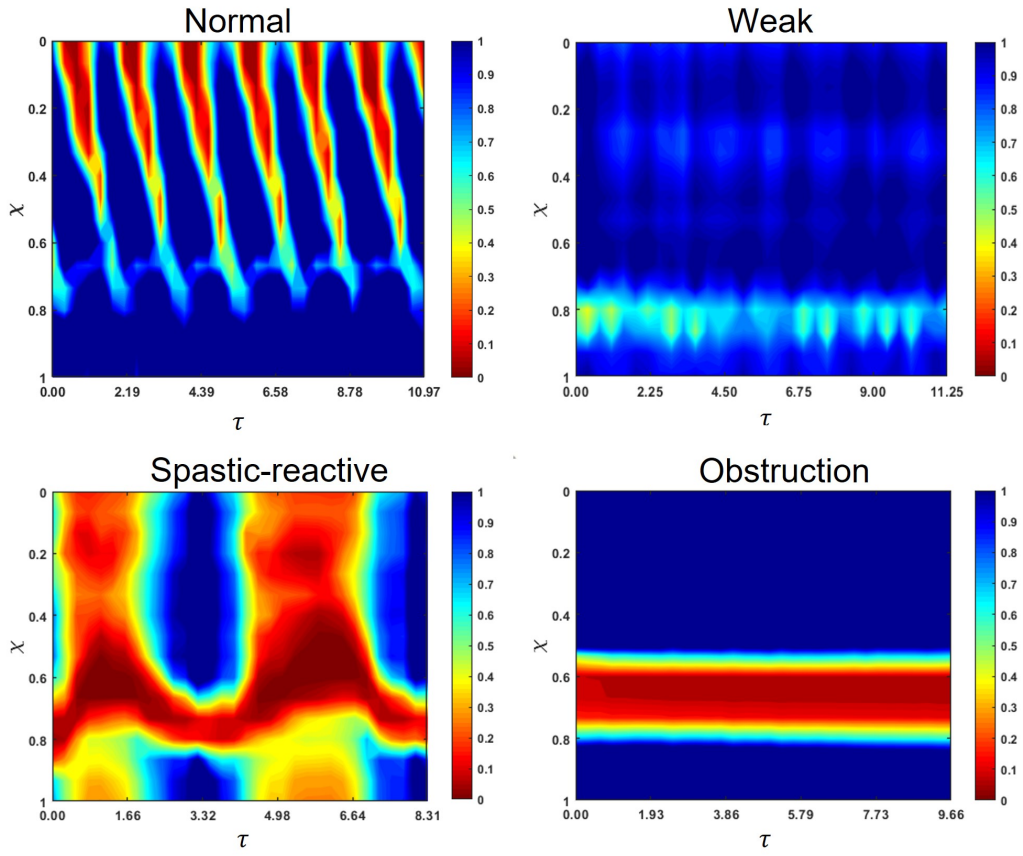

Figure 5.5. Examples of the variation of the activation parameter θ for each of the four groups according to FLIP-based motility classification: normal, weak, obstruction, and spastic-reactive.

sustained LES contractions or repetitive retrograde contractions. Figure 5.5 shows a typical example for each of the four groups. The distribution of the subjects in each of the 4 FLIP-based classification groups is shown in Table 5.1. The distribution of these subjects according to the Chicago Classification based on the manometry tests is also shown in Table 2. This set of FLIP data was used in the mechanics-based analysis for 50 ml and 60 ml FLIP distension and the corresponding calculated mechanics-based parameters were used for training the MI-VAE. Within this cohort, there were 24 achalasia patients with

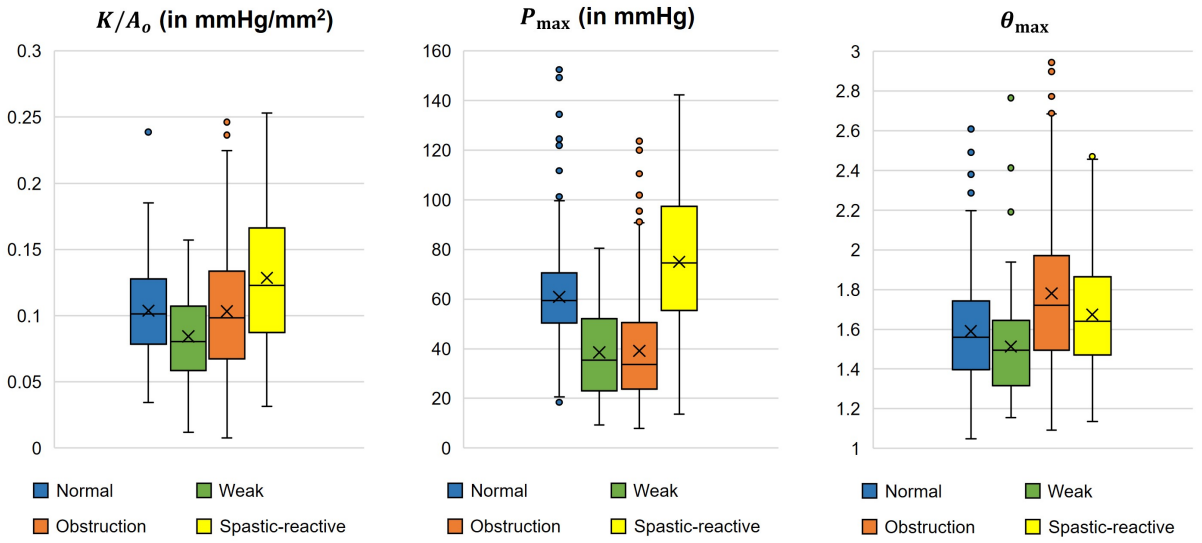

Figure 5.6. Box plots showing the distribution of the 3 mechanics-based parameters: K/A_o, $P_{\max}$, and $\theta_{\max}$.

data available before and after treatment with pneumatic dilation [**93, 94, 95**], laparoscopic Heller myotomy (LHM) [**96, 97**] or peroral endoscopic myotomy (POEM) [**98, 99**]. Additionally, there was one achalasia patient for whom post-POEM data were available for tracking (years 1, 2, 4, and 7).

The distributions 3 important scalar mechanics-based parameters according to the FLIP-based motility classification is shown in Figure 5.6. The patient cohort generated a total dataset of size 1480 since two FLIP bag volumes were used for measurements (50ml and 60ml). This was augmented to generate a larger dataset of 112,480. The parameters K/A_o, $P_o - K$, and P_d were augmented by multiplying with a factor f calculated as follows:

$$f = 1 + 0.05\mathcal{N}, \tag{5.6}$$

Table 5.2. Augmentation details for cross-sectional area

Augmentation type	**Albumentations parameters**
Grid distortion	p=0.9, num_steps=4, distort_limit = (-0.2,0.2)
Elastic transformation	p=0.8, alpha=5.0, sigma=100, alpha_affine = 2.0
Motion blur	p=0.7, blur_limit = (3,6)

wherein $\mathcal{N}$ is a random sampling from a normal distribution with its magnitude less than 2. The raw cross-sectional area variation $A(x,t)$ was augmented using a combination of grid distortional, elastic transformation, and motion blur available in the opensource Python library Albumentations [**100**], the details of which are provided in Table 5.2. Using the augmented cross-sectional areas and the augmented values for K/A_o, $P_o - K$, P_d and T, we solved equations 5.3 and 5.4 to obtain $\theta(\chi,\tau)$. Finally, the corresponding $P_{\max}$ and $\theta_{\max}$ were calculated by taking the maximum of P_d and θ, respectively.

5.2.3. Training and prediction

The final form of the loss function used for the MI-VAE is as follows:

$$L := \frac{1}{2M}\sum_{i}^{M}\left[1 + \log\sigma_{q,i}^2 - \sigma_{q,i}^2 - \mu_{q,i}^2\right] + \frac{\beta}{N}\sum_{j}^{N}\left(\theta_j - \hat{\theta}_j\right)^2, \tag{5.7}$$

wherein i represents each component of the latent space and j represents each component of the matrices θ and $\hat{\theta}$. M is the dimension of the latent space and N is the product of the two spatial dimensions of the input and generated output. In this case, $M = 40$ and N=512. The first term is the Kullback-Leibler divergence (KLD), and the second term is the reconstruction loss. Here $q(z|\theta)$ is the approximate posterior distribution which is a Gaussian distribution with a mean and standard deviation of μ_q and σ_q, respectively. The details of the derivation of the KLD term are provided in the Appendix C. β is a

scaling parameter used to balance the magnitudes of the reconstruction loss and the KLD for proper training of the MI-VAE. We found that $\beta = 1000$ resulted in a good balance between the two losses. The loss function shown in Equation 5.7 is described for each input. While training, we defined the total loss as the mean of L calculated over the mini-batch dataset. The input of the MI-VAE i.e., θ, was scaled to lie between 0 and 1, and then subtracted from 1 so that the lesser values at the contraction zones would have greater values instead. Thus, the MI-VAE focusses on minimizing the reconstruction error at the contraction zones since they have the most impact in the variation of θ. Of the 112,480 mechanics-based parameters, 112,392 were used for training and the remainder for testing. MI-VAE was trained for 250 epochs. We used a learning rate of 1×10^{-4} for the first 180 epochs and 3.3×10^{-5} for the final 70 epochs. Adam [**71**] was used as the optimizer. The network achieved an average mean-squared error between input and generated output as 1.77×10^{-3} and a KLD loss of 1.52. We used TensorFlow [**70**] to train the MI-VAE.

5.2.4. Post-processing

The 46-dimensional VDL was reduced to 3 dimensions for visualization. This dimensional reduction was done using linear discriminant analysis (LDA). This dimensional reduction was done using two methods: linear discriminant analysis (LDA) and principal component analysis (PCA). LDA is a supervised approach whereby the FLIP-based classification was used. LDA minimizes the distance between VDL points with the same four FLIP groups and maximizes the distance between points with different diagnoses. This was done by finding directions in the high-dimensional space that most effectively separated the data

into groups. Alternatively, PCA is an unsupervised approach that reduces dimensions by projecting the 46-dimensional VDL vectors onto 3 vectors with the greatest variances in data. We used an open source Python library Scikit-learn [**101**] to perform dimension reduction using LDA and PCA. Note that when we used LDA for the dimension reduction, we did not use the 'inconclusive' label for training, but only the conclusive diagnoses on FLIP. Thus, the inconclusive data labels did not add noise to our analysis.

LDA and PCA are both based on linear models to find optimal projection from high-dimensional space to low-dimensional space, in which the former aims to maximize the cross-class variation constrained by in-class variation, and the latter aims to maximize the variation without class information (i.e., unsupervised). Singular value decomposition (SVD) on covariance matrix will be identical to PCA. Compared with other techniques such as t-distributed stochastic neighbor embedding (t-SNE) and uniform manifold approximation and projection (UMAP), which involve nonlinear projection (or dimension reduction), LDA and PCA are simpler and more easily explained. Moreover, the current projection starts from latent space after data transformation by encoder model. The entire transformation from raw data to projected space is actual a composite mapping, consisting of an encoder mapping followed by projection mapping. With a well-trained sophisticated encoder model, nonlinear transformation, by t-SNE or UMAP is unnecessary, although they may be more useful when directly projecting the raw data. Also, t-SNE and UMAP creates a low-dimensional visualization of the high-dimensional data through a process of iteration. This leads to not only a general increase in computational time, but also necessitates the search and selection of the maximum number of iterations. These two methods have additional parameters including perplexity (in the

case of t-SNE) and number of neighbors (UMAP), which require interpretation by the user and tuning. The resulting visualizations may differ based on the parameters. It is also worth noting that the initialization of t-SNE is random, causing potential issues with robustness/repeatability. Last but not the least, we used LDA and PCA just to have a simple visualization tool after the latent space is generated using the MI-VAE. The actual VDL and its application is in the higher dimension of 46 and does not change based on how the data are visualized.

5.3. Virtual disease landscape in reduced dimensions

The VDL was populated with points corresponding to the original dataset rather than the augmented data since only their diagnoses were known. Figure 5.7 shows the dimension reduced VDL generated by LDA and PCA. The patient groups clustered into different regions of the VDL, but these clusters also overlapped. As shown in Figure 5.7a with the dimension reduced VDL using LDA (ldaVDL), most of the normal subjects lay on the right side of the VDL, whereas the patients with EGJ obstruction lay on the left side. The other two groups were distributed between the extremes. The overlap and separation among groups mirrored the similarity of their contractile responses on FLIP testing. For instance, normal subjects usually have FLIP patterns exhibiting antegrade contractions and normal EGJ opening. On the other hand, patients with obstruction at EGJ show no antegrade contractions and reduced EGJ opening. The other patient groups exhibit varied contractile behavior ranging from weak antegrade contractions to an irregular contractile response along with normal or borderline EGJ opening. Similar behavior was observed in the dimension reduced VDL using PCA (pcaVDL) shown in Figure 5.7b. However,

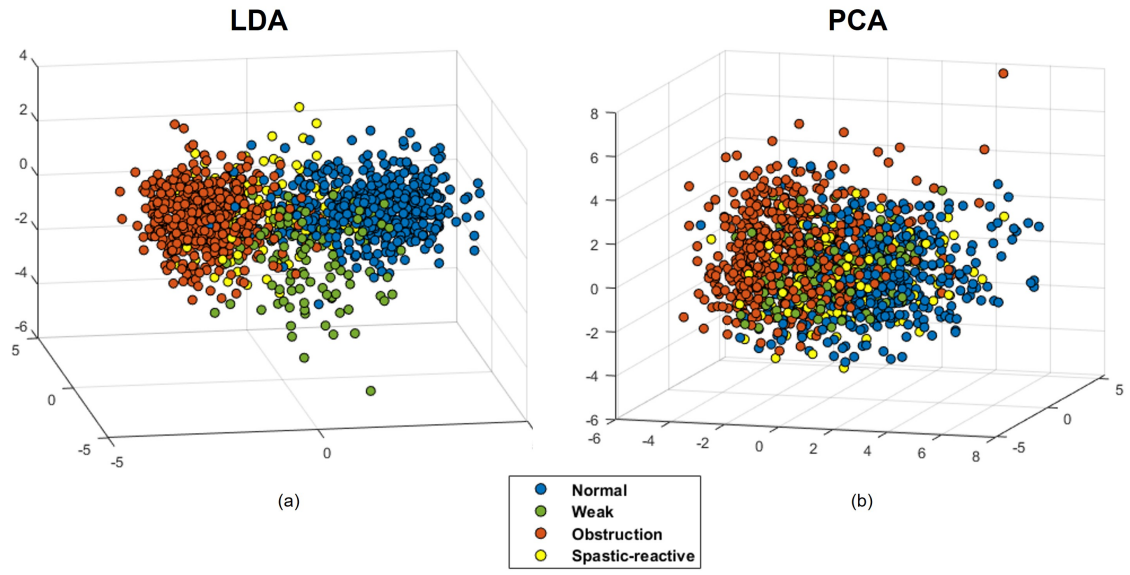

Figure 5.7. Dimension-reduced VDL using a) LDA and b) PCA. The four patient groups are shown with different colors.

the overlap among patient groups in pcaVDL was greater compared to that of ldaVDL. This is visualized more quantitatively in the distance matrix heatmaps of Figure 5.8. An element in the i-th row and j-th column of the distance matrix is the median distance between the points of the j-th cluster and the centroid of the i-th cluster. Thus, for a good separation between clusters, the diagonal elements should have lesser values compared to the off-diagonal elements. As shown in Figure 5.8, the diagonal elements of distance matrix for ldaVDL were less than those of pcaVDL. Also, the off-diagonal elements of the distance matrix for ldaVDL were greater compared to those of pcaVDL. Hence, the LDA better segregated the patient groups consistent with it being based on a supervised approach of labeling points. However, it should be noted that the 46-dimensional VDL was generated in an unsupervised manner. This high-dimensional VDL captures the similar and dissimilar features of the input corresponding to the patient groups. Thus, dimension

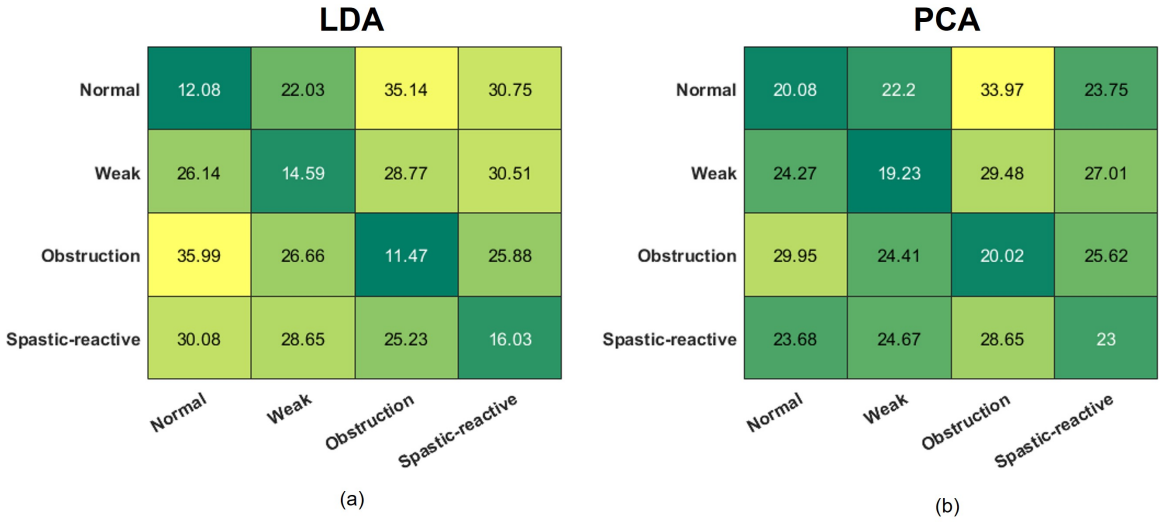

Figure 5.8. Distance matrix showing the median distance between points of each patient group specified by columns with the centroid of disease cluster specified by the rows. Each row has been normalized to represent distances as percentage and so each row adds up to 100.

reduction based on the variance of the data in an unsupervised manner as done in PCA provides insight into the structure of the 46-dimensional VDL. The clusters still observable after PCA demonstrated that the VDL successfully identified features distinguishing among these esophageal disorders. The choice between ldaVDL and pcaVDL depends on the application; pcaVDL should be chosen if there is low confidence in diagnostic distinctions within the data.

The availability of the data for the various disease groups determined the simple sizes. The main purpose for the MI-VAE is to generate the VDL and not predictive analysis. Thus, the diseases with smaller sample sizes appear as smaller clusters on the VDL and their location with respect to the other groups is determined by their contraction pattern. Additionally, the most distinct responses to FLIP distention occurs for normal subjects and obstruction groups. Both groups are of comparable sizes (normal: 221, obstruction:

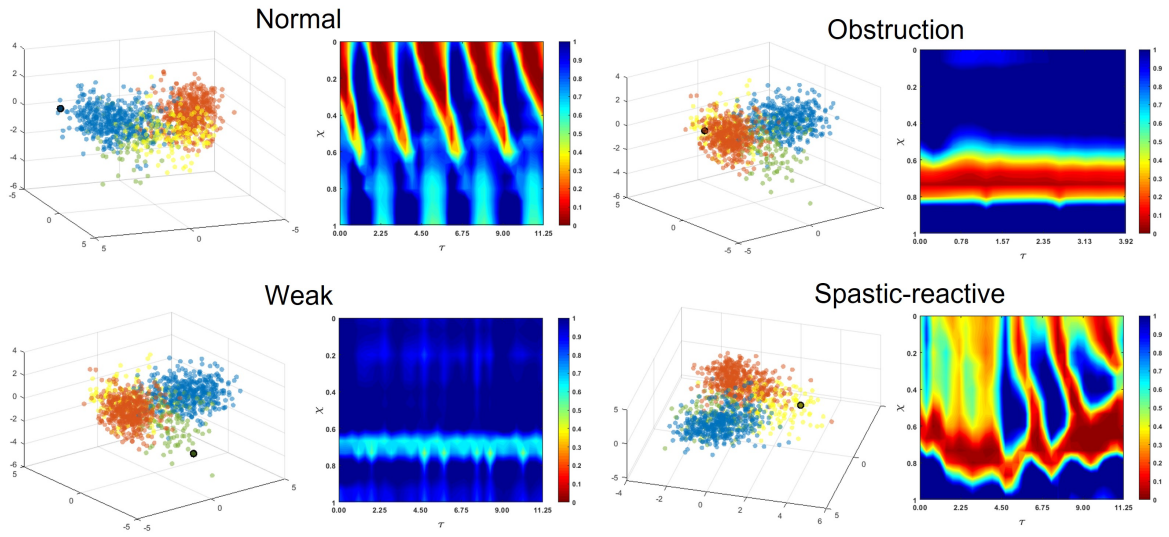

Figure 5.9. Variation of θ corresponding to the extreme points from the four groups on the ldaVDL.

245). Rest of the diseases lie somewhere between these two groups and often have very similar FLIP responses in terms of their contraction pattern as shown in Figure5.7. Since no labels were used in training the MI-VAE, this proves the accurate representation of the diseases through the VDL by the MI-VAE. Augmenting the dataset also makes the MI-VAE more generalizable. Thus, a high training and validation accuracy (or low values of losses) ensures that all the diseases are accurately represented on the VDL (through the MI-VAE's latent space).

Figure 5.9 shows the contraction patterns corresponding to four points chosen from the extremes of the 4 clusters on the VDL to add intuition of the four cluster distribution on the VDL. Indeed, the contraction patterns are significantly different from each other, thus providing further insight into the nature of clustering. These four contraction patterns capture the distinctive signature of the 4 groups. The normal contraction pattern shows regular RACs, weak contraction pattern shows almost not contraction with

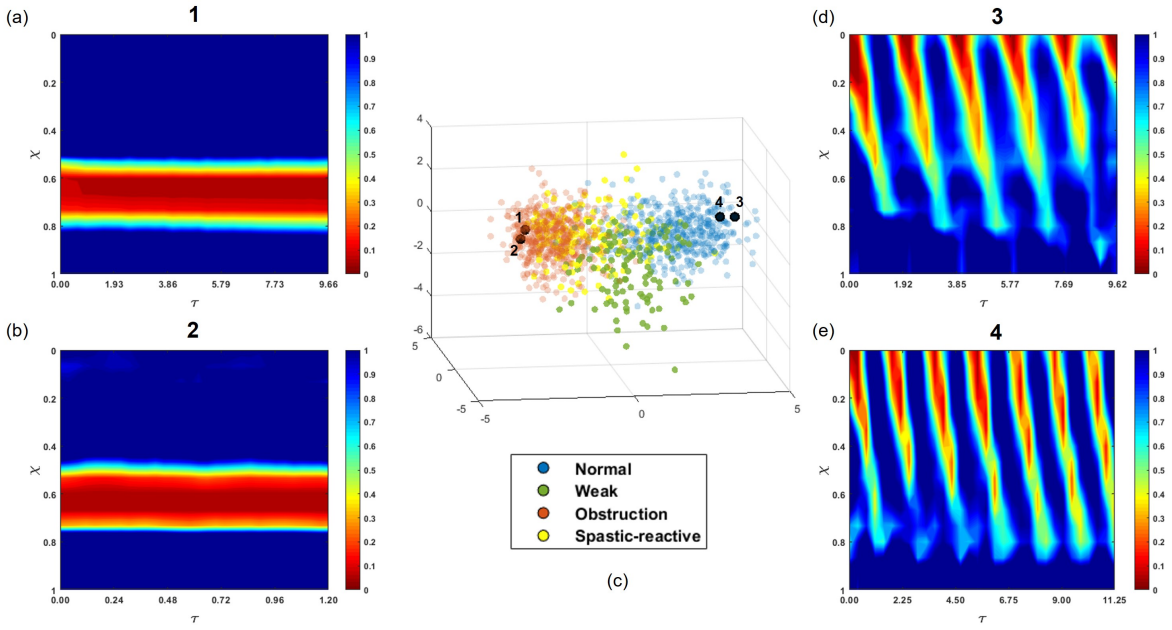

Figure 5.10. The continuous behavior of the VDL is shown through points selected from its two extremes: Normal subjects and obstruction patients. (a) and (b) show the characteristics of typical obstruction patients with no contraction at the esophageal body and a strong tone at the EGJ marked by the horizontal red zone. (d) and (e) show a typical contraction pattern in normal subjects with strong antegrade contractions and relaxed EGJ. (c) VDL represents of the contraction patterns 1-4.

EGJ relaxation, obstruction shows a strong unrelaxed EGJ tone with no contraction, and spastic-reactive contraction contractile pattern shows retrograde/spastic contractile response.

5.4. Properties of the VDL

5.4.1. Continuous behavior of the VDL

The ability of the VDL to identify the similarities and dissimilarities among patient groups is further illustrated in Figure 5.10. Two points in close proximity were selected from the extreme right end of the normal subjects and two from the extreme left end of the

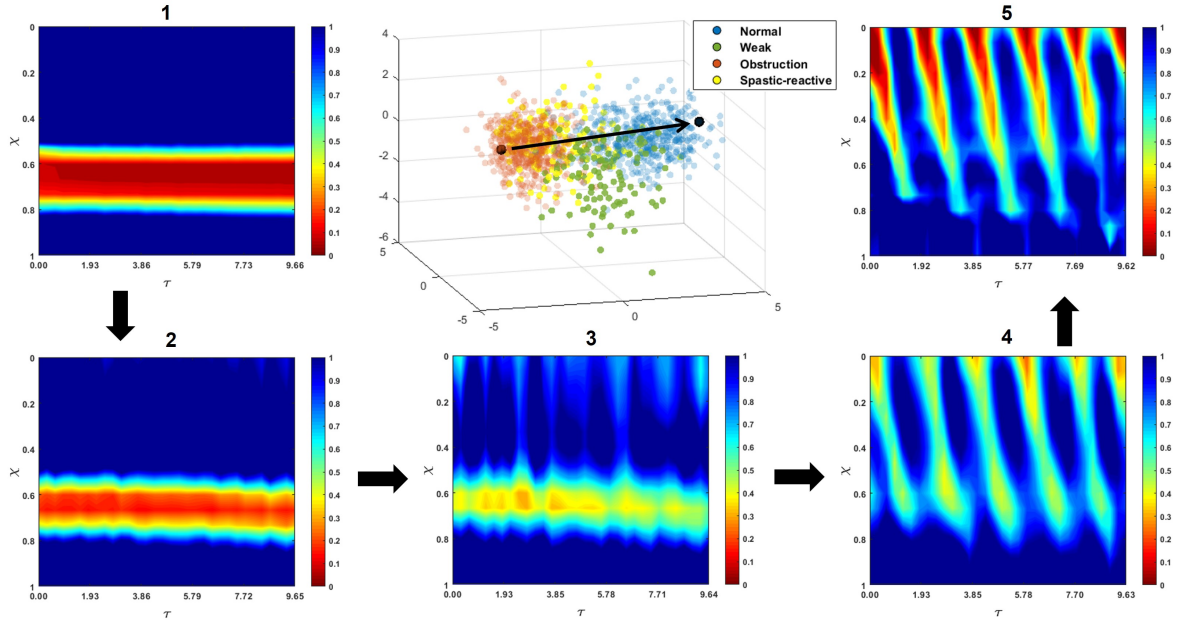

Figure 5.11. Example to describe the generative nature of the VDL. Points 1 and 5 are chosen at the extremes of obstruction patients and normal subjects , respectively. Points 2-4 are equi-spaced along the vector joining 1 and 5. The θ variations generated for 2-4 show the transition from obstruction to normal characteristics.

obstruction patients. The normal subjects both showed normal antegrade contractions (oblique red bands) and a relaxed EGJ (blue region ahead of the contraction). Similarly, the two points of obstruction showed similar variation of the activation parameter; both exhibited no contraction and the EGJ remained closed as evident by the horizontal red band at the distal esophagus. The large separation between points 1 and 2 from points 3 and 4 indicates that they displayed completely different behavior.

5.4.2. Generative property of the MI-VAE

An important feature of the MI-VAE is its generative capability. Due to the continuous nature of the VDL, new vectors from the VDL i.e., those which were not present in the

training set can generate meaningful representations of the mechanics-based parameters. Figure 5.11 illustrates the transition from a point at the extreme of the obstruction cohort to another point at the extreme of normal. A 46-dimensional vector was calculated between these points and 3 equispaced intermediate points along this vector. Thus, the 2 endpoints were known but the 3 intermediate points were new and generated mechanics-based parameters not known before. As the transition occurs between the extremes, we see that the antegrade contraction progressively strengthens and EGJ tone relaxes. Note that the vector (or line) shown in Figure 5.11 does not represent an actual case, but a hypothetical one to demonstrate the capability of the VDL. In an actual scenario, the disease progression or motility improvement won't necessarily be linear as suggested in Figure 5.11. However, if the disease remains stable or progresses or improves in an irregular manner, we can still use the VDL to extrapolate to the likely future 'mechanical' state in an average sense based on the pattern of past data.

Additionally, we can retrieve the other mechanics-based parameters apart from the θ variation, i.e., K/A_o, $P_{\max}$, T, and $\theta_{\max}$. This was the main reason for choosing mechanics-based parameters as the input of the MI-VAE rather than the raw distal pressure and cross-sectional area variations. The generated parameters reflect on the mechanical health of the organ unlike the raw data generated from FLIP. Additionally, with the application of mechanics, the two distributed measurements (cross-sectional area, $A(x,t)$, and distal pressure $P_d(t)$) were combined into one activation parameter $\theta(x,t)$, which not only simplified application of the MI-VAE, but also has physical meaning since it estimates esophageal muscle contraction.

5.5. Comparison with HRM

The VDL offers a unique framework for comparing HRM and FLIP response among patients with motility disorders and normal subjects. Figure 5.12 shows the distribution of the HRM diagnosis on the ldaVDL based on FLIP response. To clarify, the positions of the points in the VDL is the same as Figure 5.12 (generated through LDA on 46-dimensional VDL using FLIP classification labels), but the colors are assigned based on manometry diagnosis. There is a clear clustering of the HRM groups with abnormal EGJ opening (Type I, II, III achalasia and EGJOO) and those related to contractile patterns but better EGJ opening (normal, absent contractility, ineffective esophageal motility, and distal esophageal spasm). This is seen more quantitatively through the distance matrix in Figure 5.12. Two clear blocks can be seen. From rows 1-4, we see that type I, II, III achalasia, and EGJOO have relatively similar values but much lower than the other groups. The same trend can be seen for normal, absent contractility, ineffective esophageal motility, and distal esophageal spasm in rows 6-9. This indicates that these two subgroups cluster separately and have different FLIP response compared to each other.

An important feature of LDA is that it not only serves as a dimension reduction framework, but also a classifier. Thus, every point on the ldaVDL has an associated probability for the four FLIP classification groups. This feature can be used as well to compare CCv4.0 with the FLIP motility classification. The box plots in Figure 5.13 show how the various CCv4.0 diagnosis is distributed over the four FLIP classification groups. Type I, II achalasia and EGJOO very clearly appear as obstruction on FLIP due to their strong EGJ tone and lack of any contractile behavior. Normal on HRM also appear mostly normal on FLIP but has a huge variability. Type III achalasia and hypercontractile esophagus are

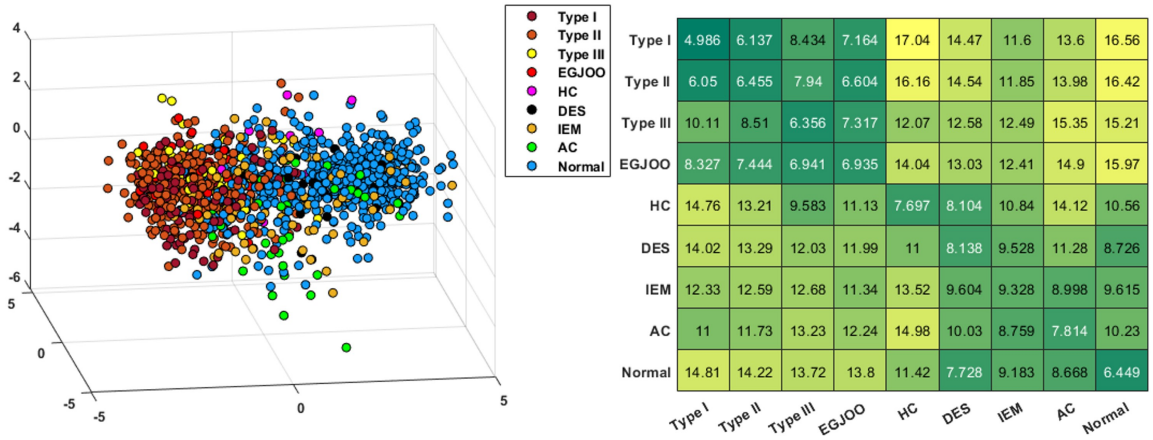

Figure 5.12. Comparison of FLIP-based classification with HRM based CCv4.0 using the ldaVDL and distance matrix.

distributed almost equally between obstruction and spastic-reactive. Absent contractility, which exhibit EGJ relaxation but poor contractile response, are distributed between weak and normal by FLIP classification. IEM and DES are distributed between normal and obstruction groups on FLIP (DES more so than IEM). This is mainly because they both exhibit contractile response but without effective transport. Since DES has a much smaller sample size in the dataset, the trends do not provide a strong consolidation of comparison between HRM and FLIP as IEM does.

Note that this is not just a comparison of the classification schemes based on HRM and FLIP or even a comparison between the two modalities of estimating esophageal function. The physiological response to HRM and FLIP is very different. HRM is associated with primary peristalsis which is triggered when the upper esophageal sphincter (UES) opens to allow the swallowed bolus to enter the esophagus. FLIP, on the other hand, measures the response of the esophagus to distension which leads to secondary peristalsis. Unlike primary peristalsis, secondary peristalsis do not get triggered by UES opening, but by

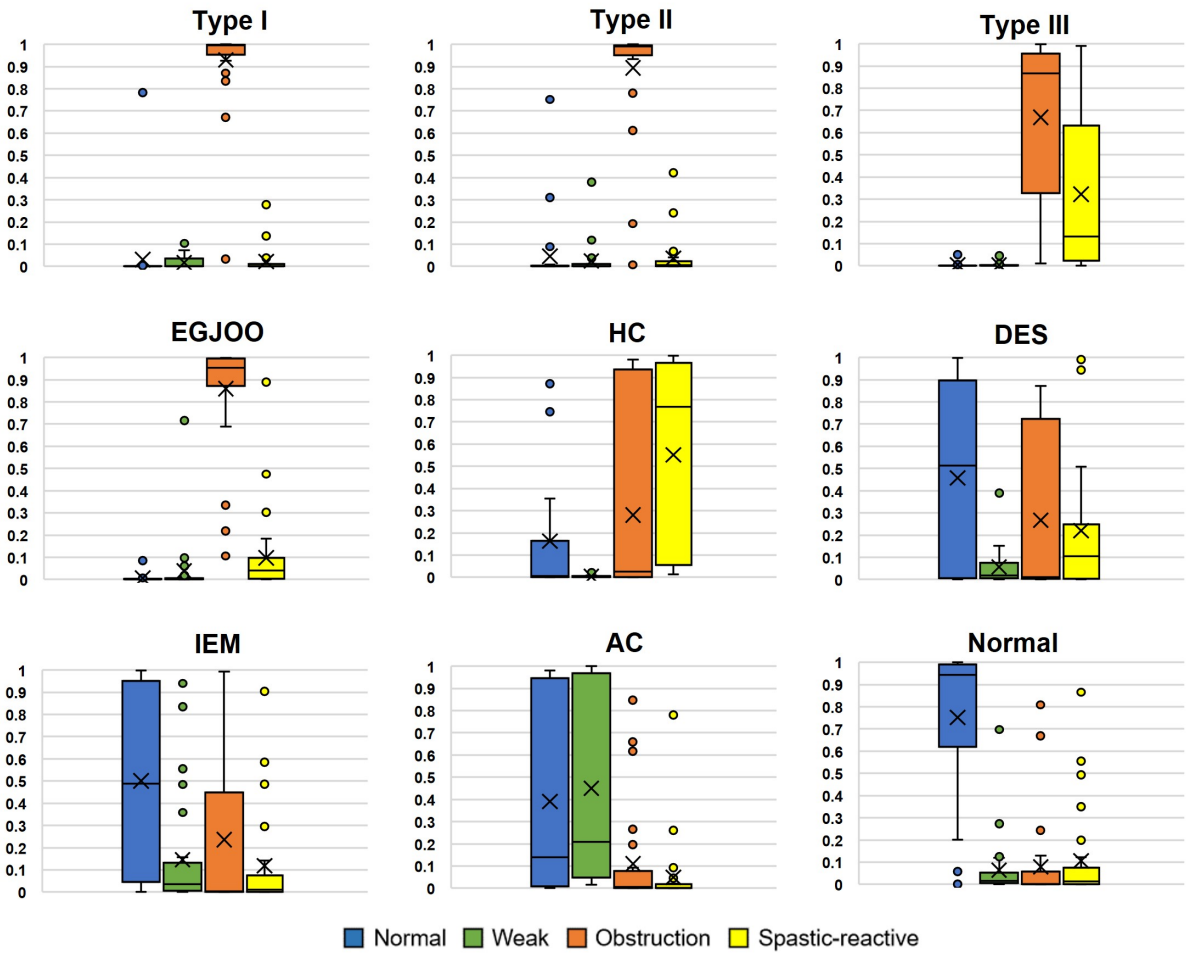

Figure 5.13. Comparison of FLIP-based classification with HRM using the probabilities assigned by the fitted LDA classifier on every point on the ldaVDL.

distention. In addition, the sustained distention by FLIP leads to a unique secondary peristaltic response called repetitive antegrade contractions (RACs) which is completely different from primary peristalsis. FLIP has been shown to identify various esophageal disorders in some cases that appeared normal on HRM and other diagnostic tests. Therefore, this comparison of HRM with FLIP using the VDL, provides a formal approach towards a complete picture of esophageal function under all scenarios. Additionally, it also points

out the limitations of each of the two modalities and their classification capabilities on a finer level, thus aiding in future reclassification approaches.

5.6. Estimating effectiveness of treatment

Treatment strategy varies depending on the mechanical 'health' of the esophagus. For example, achalasia shows a θ variation with a strong tone (low values of θ) at the EGJ that does not relax, and the severity of the scenario is greater with progressively lower values of θ. Less 'potent' treatment with pneumatic dilation could suffice for less severe cases while using laparoscopic Heller myotomy (LHM) myotomy, or peroral endoscopic myotomy (POEM) for severe cases. We hypothesize that our framework could be used to guide the need for treatment by quantifying the severity as well as aid in early discovery of the disorders. FLIP studies can be obtained before and after these procedures to evaluate the effectiveness of a treatment as well as for tracking the esophageal condition for years after treatment. In the next two subsections, we discuss two such scenarios where the MI-VAE framework can be applied to aid FLIP diagnosis.

5.6.1. Pre- and post-treatment state of the esophagus in achalasia patients

With a myotomy, the circular muscle fibers of the lower esophageal sphincter are cut to weaken the inherent tone at the EGJ making it easier for swallowed food and fluid to empty from the esophagus. POEM is an endoscopic myotomy wherein the circular muscle fibers of the lower esophageal sphincter $\pm$ the distal esophagus are cut. Using the MI-VAE framework, we present a quantitative approach for assessing the effectiveness of a POEM procedure. We tested this on three achalasia patients, one for each achalasia

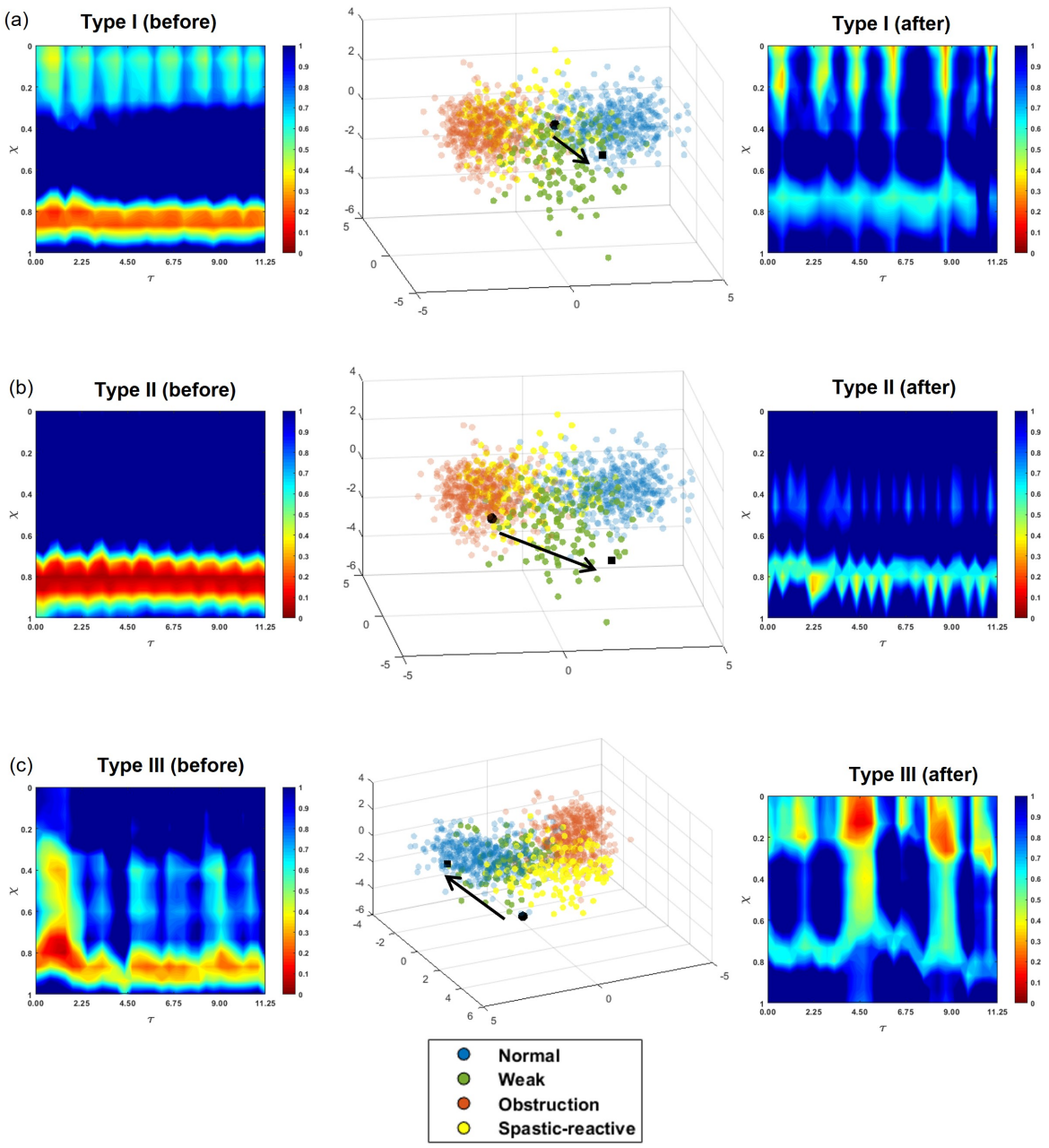

Figure 5.14. Estimating the effectiveness of a POEM procedure on achalasia patients using MI-VAE. (a)-(c) show the θ variation before and after treatment in achalasia types I, II, and III, respectively.

subtype. Figure 5.14 illustrates the contraction patterns before and after POEM along with their placement on the VDL. We selected the "typical" θ variation for each case by identifying the most effective contraction and the least EGJ tone observed at the same 50 mL FLIP bag volume. In Figure 5.14a, it is evident that after POEM, the EGJ tone had decreased significantly with improvement in contraction strength and pattern. On the VDL, this corresponded to the movement from the right end of the obstruction zone toward the normal subjects near the weak group. For the type II patient shown in Figure 5.14b, lower esophageal sphincter tone was clearly diminished by treatment but there was minimal recovery of the esophageal contraction and movement on the VDL is toward the weak contraction group. In Figure 5.14c, we see that for the type III patient, the contraction strength improved significantly after POEM (albeit not antegrade) and EGJ tone was reduced such that the corresponding point in the VDL lay more in the normal cohort zone moving from the spastic-reactive zone. The improvement after treatment can be estimated quantitatively by the magnitude of the vector drawn from the initial to the final point in the VDL. The direction of the vector quantitatively estimates the direction of improvement. This vector corresponds not only to the θ variation, but also to the discrete mechanics-based parameters adding physical meaning to the quantitative assessment to treatment effectiveness.

5.6.2. Post-treatment tracking

After treatment, it is often necessary to periodically re-evaluate patients over time. We tested our MI-VAE framework by tracking the condition of one patient who had undergone POEM and had FLIP data was available for years 1, 2, 4, and 7 after POEM. The

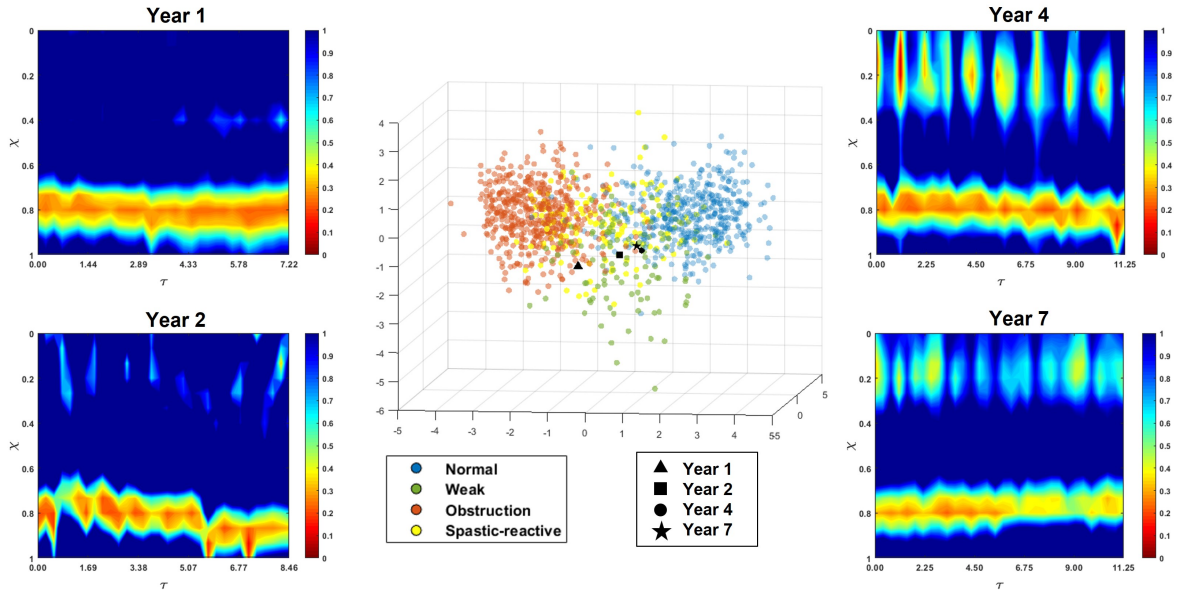

Figure 5.15. Tracking the state and motility of the esophagus after POEM for 7 years. Four θ variations are shown as observed in the 1st, 2nd, 4th, and 7th year after POEM.

θ variations for each of these four years are shown in Figure 5.15 and a gradual improvement can be seen over the years that has settled at a specific location on the VDL.The improvement can be seen specifically with the contraction strength and pattern, and more quantitatively through the VDL. This example shows how the MI-VAE framework can be used for post-POEM tracking of patient condition but can be applied very easily to other treatment procedures as well.

5.7. Limitations

The MI-VAE framework provides a technique to map esophageal disorders onto a parameter space called the VDL based on their mechanical characteristics estimating the mechanical 'health' of the esophagus thereby aiding in diagnosis and directing treatment.

However, the VDL also has limitations. First, the FLIP device has some technical limitations. It has an upper measurement limit for diameter which corresponds to the maximum distension of the FLIP bag. Strong contractions might sometimes lead to the bag distending greater that this upper limit and cause incorrect readings. It also has a lower limit for its measurements owing to the catheter diameter onto which the bag is mounted. Again, strong contractions might cause full collapse of the FLIP bag on the catheter leading to incorrect readings. Additionally, it is sometimes observed that the bag volume calculated using the diameter readings might not be equal to the actual recorded bag volume. These factors might cause errors in the prediction of MI-VAE. Second, all esophageal disorders are not well represented in the dataset and there is a wide range of sample sizes. The characteristics of the disorders represented by a smaller dataset (like DES and HC) might not be learned properly by the MI-VAE. Therefore, the relative placement of the points on the VDL through LDA might not be as accurate as the disorders represented by a larger dataset. Third, reduction of the VDL dimensions using LDA and PCA for visualization might lead to loss to important features that define the state and functioning of the esophagus. Fifth, as described earlier, the labels used for dimension reduction using LDA is patient-specific, and not specific to the mechanics-based parameters. For instance, some θ variations of normal subjects might not exhibit RACs. This might introduce some errors in the prediction of MI-VAE.

5.8. Conclusion

In this work, we presented a framework called mechanics-informed variational autoencoder (MI-VAE) that quantitatively identified and distinguished among esophageal

disorders based on their physical characteristics through a parameter space called the virtual disease landscape (VDL). The physical characteristics were estimated through a set of physical parameters such as esophageal wall stiffness, contraction pattern, active relaxation of the esophageal wall muscles, and work metrics estimating EGJ behavior. These parameters were solved in a patient-specific manner from FLIP data using a one-dimensional mechanics-based inverse model. The VDL identified similarities and dissimilarities among the esophageal disorders as well as classified them based on their contractile characteristics. We also described how the generative property of the MI-VAE gives it the capability to predict disease progression in time. Furthermore, we demonstrated through clinical applications that the MI-VAE can estimate the effectiveness and stability of a treatment over time. Finally, since the MI-VAE framework uses mechanics-based predictions of physiomarkers to develop a VDL, it can be extended to be used with other diagnostic technologies (and organs) as long as mechanics-based physiomarkers can be derived with them. For instance, a similar MI-VAE can be developed using high resolution impedance manometry (HRIM) data using the same governing equations with pressure and cross-sectional area measured from the HRIM catheter. Additionally, mechanics-based analysis has been shown to be applied to fluoroscopy [**44**] to predict physiomarkers which can also be used as described in this chapter.

CHAPTER 6

Concluding remarks and future scope

In the last four chapters, we have seen how mechanics can be used in unique ways for esophageal diagnosis and treatment planning. In chapter 2, we have discussed the application of an in-silico model of the esophagus (vEsophagus) to understand the impact of various myotomy parameters in the formation of a complication called blown-out myotomy (BOM). With this analysis, we were able to identify the safest approaches for myotomy the minimizes the risk for BOM formation. In chapter 3 and 4, we have discussed how important physiomarkers can be estimated in a patient-specific manner using measurements from fluoroscopy and MRI, respectively. These frameworks not only increase the capabilities of the diagnostic technologies, but also predict underlying factors associated with various esophageal diseases. Finally, in chapter 5, we have described how the mechanics-based physiomarkers can be mapped onto a parameter space called virtual disease landscape (VDL) to identify the underlying similarities between various esophageal diseases based on their mechanical behavior.

Although these frameworks quantify unique and specific characteristics of esophageal state and function, they are not independent of each other. Together, they provide a unified approach for using mechanics in a meaningful and structured manner for esophageal research that has the potential for significant impact. Figure 6.1 shows the connections between these frameworks and how they fit into the current picture of medical diagnosis. At the very center, the current steps for medical diagnosis and treatment planning is shown

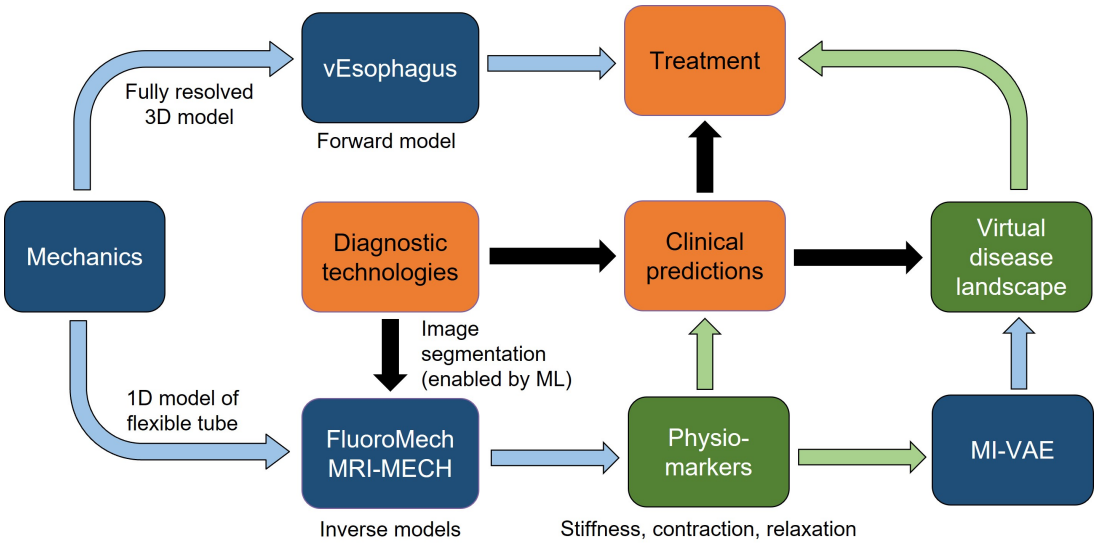

Figure 6.1. Relationships between the various focus areas.

in orange boxes and connected by black arrows. As described above, trends in the physical variables such as pressure and cross-sectional areas are directly used for clinical predictions following which treatment planning is performed. In this current picture, mechanics provides two pathways. The first path is using forward model, such as the vEsophagus, to investigate the impact of different anatomical components and changes made to them during surgery to predict post-surgery outcomes and thus, help in treatment planning. This pathway is not patient-specific but uses general information about the esophagus for a parametric study of the impact of various surgery parameters. The second path is the use of inverse models, such as FluoroMech and MRI-MECH, to estimate esophageal state and function in a patient-specific manner through mechanics-based physiomarkers such as wall stiffness and contraction pattern. These physiomarkers potentially lead to a more accurate clinical diagnosis. The physio-markers predicted by the inverse models are also used by the MI-VAE to identify the similarities and differences between the various

esophageal diseases by generating the virtual disease landscape (VDL). The clinical diagnosis is also used for identifying clusters on the VDL. The MI-VAE also has generative property by which new contraction patterns can be generated to help in better treatment planning.

The approaches described in this thesis provide an overview of how mechanics can be applied in various aspects of esophageal diagnosis and treatment planning. But this work is far from the complete scope of the application of mechanics to esophageal research. There is a huge potential for extending the application of this work to other organs. Several improvements can also be made in the frameworks discussed in this thesis to increase their scope and accuracy. Some of the avenues of future research are as follows.

The material properties used in the vEsophagus simulations were taken from experimental studies on porcine esophagus. The accuracy of the vEsophagus predictions can be potentially improved with material constants calculated through experiments performed on human esophagus. Furthermore, there is a necessity to map the wall stiffness predicted by the inverse models using data from FLIP, HRM and fluoroscopy to the hyperelastic material constants of the vEsophagus. This would increase the scope of the vEsophagus to be applied for treatment planning such as bariatric surgeries in a patient-specific manner.

The inverse models work with various diagnostic technologies for patient-specific analysis of esophageal transport and predict mechanics-based parameters that estimate esophageal health. But the measurements of various esophageal diagnostic devices are largely different. For instance, HRM measures primary peristalsis whereas FLIP measures secondary peristalsis. Fluoroscopy provides only a two-dimensional visualization of the esophageal lumen and is primarily used to estimate bolus clearance and identify irregularities in the

esophageal cross-section such as diverticulum. These differences in each of these technologies require the development of the inverse model specific to each of the diagnostic tests. In order to obtain a complete understanding of the source of an esophageal disorder, it is necessary to develop a unified framework that takes into consideration the measurements from a variety of these diagnostic tests and uses the physical laws of mass and momentum conservation to estimate the complete health of the esophagus.

The MI-VAE provides a novel framework to estimate the differences between various esophageal diseases based on their mechanical behavior using the virtual disease landscape (VDL). As discussed in chapter 5, the VDL can be used for tracking the patient condition over time. This idea can be extended very easily to identify how various disease progress from early to late stages. This was not possible to accomplish in this thesis because of the lack of availability of time-series patient data. In the future, if patient data becomes available with disease progression, then the VDL can be immediately applied, without any major modification, to understand how various diseases progress over time. This has an immense potential for treatment planning. In chapter 5, we have compared the FLIP-based motility classification with the Chicago Classification v4.0 using the VDL generated from FLIP data. Although this revealed important characteristics of esophageal response in terms of primary and secondary peristalsis, more insights can potentially be obtained if a new VDL is also created with HRM data. This would allow direct comparison of the two important physiological responses (primary and secondary peristalsis) through the VDL. There is also a huge scope of using the VDL for development of mechanics-based physiomarkers. Recall that the axes of the VDL are abstract quantities and have no physical meaning. But they do have an important characteristic which is to identify the

differences between various esophageal diseases purely based on the wall mechanics. Thus, any novel mechanics-based metrics need to correlate well with the axes of the VDL which separate certain diseases well. Therefore, the VDL works as a great testing and validation framework for the development of novel mechanics-based physiomarkers for esophageal diseases. Finally, there has also been active cardiovascular [**102**] and respiratory [**103**] research to develop physiomarkers for quantifying the course of diseases such as aortic aneurysms through wall shear stress, or the effectiveness of drug delivery in the lungs [**104**]. These mechanics-based physiomarkers could be used to develop a VDL for these organs.

References

[1] Hashem B El-Serag, Stephen Sweet, Christopher C Winchester, and John Dent. Update on the epidemiology of gastro-oesophageal reflux disease: a systematic review. *Gut*, 63(6):871–880, 2014.

[2] Takahisa Yamasaki, Colin Hemond, Mohamed Eisa, Stephen Ganocy, and Ronnie Fass. The changing epidemiology of gastroesophageal reflux disease: Are patients getting younger? *Journal of neurogastroenterology and motility*, 24(4):559–569, 2018. PMID: 30347935.

[3] Neil Bhattacharyya. The prevalence of dysphagia among adults in the united states. *Otolaryngology–Head and Neck Surgery*, 151(5):765–769, 2014. PMID: 25193514.

[4] Wenjun Kou, Amneet Pal Singh Bhalla, Boyce E. Griffith, John E. Pandolfino, Peter J. Kahrilas, and Neelesh A. Patankar. A fully resolved active musculo-mechanical model for esophageal transport. *Journal of Computational Physics*, 298:446–465, 2015.

[5] Wenjun Kou, Boyce E. Griffith, John E. Pandolfino, Peter J. Kahrilas, and Neelesh A. Patankar. A continuum mechanics-based musculo-mechanical model for esophageal transport. *Journal of Computational Physics*, 348:433–459, 2017.

[6] M. Fox, G. Hebbard, P. Janiak, J. G. Brasseur, S. Ghosh, M. Thumshirn, M. Fried, and W. Schwizer. High-resolution manometry predicts the success of oesophageal bolus transport and identifies clinically important abnormalities not detected by conventional manometry. *Neurogastroenterology and motility : the official journal of the European Gastrointestinal Motility Society*, 16(5):533–542, 2004.

[7] Pandolfino JE, Kim H, Ghosh SK, Clarke JO, Zhang Q, and Kahrilas PJ. High-resolution manometry of the egj: an analysis of crural diaphragm function in gerd. *The American journal of gastroenterology*, 102(5):1056–1063, 2007.

[8] Pandolfino JE, Kwiatek MA, Nealis T, Bulsiewicz W, Post J, and Kahrilas PJ. Achalasia: a new clinically relevant classification by high-resolution manometry. *Gastroenterology*, 135(5):1526–1533, 2008.

[9] M R Fox and A J Bredenoord. Oesophageal high-resolution manometry: moving from research into clinical practice. *Gut*, 57(3):405–423, 2008.

[10] J. E. Pandolfino, M. R. Fox, A. J. Bredenoord, and P. J. Kahrilas. High-resolution manometry in clinical practice: utilizing pressure topography to classify oesophageal motility abnormalities. *Neurogastroenterology & Motility*, 21(8):796–806, 2009.

[11] C. P. Gyawali, A. J. Bredenoord, J. L. Conklin, M. Fox, J. E. Pandolfino, J. H. Peters, S. Roman, A. Staiano, and M. F. Vaezi. Evaluation of esophageal motor function in clinical practice. *Neurogastroenterology & Motility*, 25(2):99–133, 2013.

[12] D. A. Carlson, P. J. Kahrilas, Z. Lin, I. Hirano, N. Gonsalves, Z. Listernick, K. Ritter, M. Tye, F. A. Ponds, I. Wong, and J. E. Pandolfino. Evaluation of esophageal motility utilizing the functional lumen imaging probe. *The American journal of gastroenterology*, 111(12):1726—-1735, 2016.

[13] Rena Yadlapati, Peter J. Kahrilas, Mark R. Fox, Albert J. Bredenoord, C. Prakash Gyawali, Sabine Roman, Arash Babaei, Ravinder K. Mittal, Nathalie Rommel, Edoardo Savarino, Daniel Sifrim, André Smout, Michael F. Vaezi, Frank Zerbib, Junichi Akiyama, Shobna Bhatia, Serhat Bor, Dustin A. Carlson, Joan W. Chen, Daniel Cisternas, Charles Cock, Enrique Coss-Adame, Nicola de Bortoli, Claudia Defilippi, Ronnie Fass, Uday C. Ghoshal, Sutep Gonlachanvit, Albis Hani, Geoffrey S. Hebbard, Kee Wook Jung, Philip Katz, David A. Katzka, Abraham Khan, Geoffrey Paul Kohn, Adriana Lazarescu, Johannes Lengliner, Sumeet K. Mittal, Taher Omari, Moo In Park, Roberto Penagini, Daniel Pohl, Joel E. Richter, Jordi Serra, Rami Sweis, Jan Tack, Roger P. Tatum, Radu Tutuian, Marcelo F. Vela, Reuben K. Wong, Justin C. Wu, Yinglian Xiao, and John E. Pandolfino. Esophageal motility disorders on high-resolution manometry: Chicago classification version 4.0©. *Neurogastroenterology & Motility*, 33(1):e14058, 2021.

[14] Y. Fan, H. Gregersen, and G.S. Kassab. A two-layered mechanical model of the rat esophagus. experiment and theory. *BioMedical Engineering OnLine*, 3, 2004.

[15] W. Yang, T. C. Fung, K. S. Chian, and C. K. Chong. 3D Mechanical Properties of the Layered Esophagus: Experiment and Constitutive Model. *Journal of Biomechanical Engineering*, 128(6):899–908, 05 2006.

[16] Arturo N. Natali, Emanuele L. Carniel, and Hans Gregersen. Biomechanical behaviour of oesophageal tissues: Material and structural configuration, experimental data and constitutive analysis. *Medical Engineering & Physics*, 31(9):1056–1062, 2009.

[17] Eleni A. Stavropoulou, Yannis F. Dafalias, and Dimitrios P. Sokolis. Biomechanical and histological characteristics of passive esophagus: Experimental investigation and comparative constitutive modeling. *Journal of Biomechanics*, 42(16):2654–2663, 2009.

[18] Dimitrios P. Sokolis. Structurally-motivated characterization of the passive pseudoelastic response of esophagus and its layers. *Computers in Biology and Medicine*, 43(9):1273–1285, 2013.

[19] Brasseur J. G. A fluid mechanical perspective on esophageal bolus transport. *Dysphagia*, 2(1):32–39, 1987.

[20] Meijing Li and James G. Brasseur. Non-steady peristaltic transport in finite-length tubes. *Journal of Fluid Mechanics*, 248:129–151, 1993.

[21] M. Li, J. G. Brasseur, and W. J. Dodds. Analyses of normal and abnormal esophageal transport using computer simulations. *American Journal of Physiology-Gastrointestinal and Liver Physiology*, 266(4):G525–G543, 1994. PMID: 8178991.

[22] Sudip K. Ghosh, Peter J. Kahrilas, Tamer Zaki, John E. Pandolfino, Raymond J. Joehl, and James G. Brasseur. The mechanical basis of impaired esophageal emptying postfundoplication. *American Journal of Physiology-Gastrointestinal and Liver Physiology*, 289(1):G21–G35, 2005. PMID: 15691873.

[23] Shashank Acharya, Wenjun Kou, Sourav Halder, Dustin A. Carlson, Peter J. Kahrilas, John E. Pandolfino, and Neelesh A. Patankar. Pumping Patterns and Work Done During Peristalsis in Finite-Length Elastic Tubes. *Journal of Biomechanical Engineering*, 143(7), 03 2021. 071001.

[24] P. J. Kahrilas, A. J. Bredenoord, M. Fox, C. P. Gyawali, S. Roman, A. J. P. M. Smout, J. E. Pandolfino, and International High Resolution Manometry Working Group. The chicago classification of esophageal motility disorders, v3.0. *Neurogastroenterology & Motility*, 27(2):160–174, 2015.

[25] Salih Samo, Dustin A. Carlson, Dyanna L. Gregory, Susan H. Gawel, John E. Pandolfino, and Peter J. Kahrilas. Incidence and prevalence of achalasia in central chicago, 2004–2014, since the widespread use of high-resolution manometry. *Clinical Gastroenterology and Hepatology*, 15(3):366–373, 2017.

[26] G. Triadafilopoulos, G. E. Boeckxstaens, R. Gullo, M. G. Patti, J. E. Pandolfino, P. J. Kahrilas, A. Duranceau, G. Jamieson, and G. Zaninotto. The Kagoshima consensus on esophageal achalasia. *Diseases of the Esophagus*, 25(4):337–348, 05 2012.

[27] Guilherme M. Campos, Eric Vittinghoff, Charlotte Rabl, Mark MD Takata, Michael MD Gadenstätter, Feng Lin, and Ruxandra. Ciovica. Endoscopic and surgical treatments for achalasia: A systematic review and meta-analysis. *Annals of Surgery*, 249(1):45–57, 2009.

[28] Joseph R. Triggs, Amanda J. Krause, Dustin A. Carlson, Erica N. Donnan, Ryan A.J. Campagna, Anand S. Jain, Peter J. Kahrilas, Eric S. Hungness, and John E. Pandolfino. Blown-out myotomy: an adverse event of laparoscopic heller myotomy and peroral endoscopic myotomy for achalasia. *Gastrointestinal Endoscopy*, 93(4):861–868.e1, 2021.

[29] Anand S. Jain, Dustin A. Carlson, Joseph Triggs, Michael Tye, Wenjun Kou, Ryan Campagna, Eric Hungness, Donald Kim, Peter J. Kahrilas, and John E. Pandolfino. Esophagogastric junction distensibility on functional lumen imaging probe topography predicts treatment response in achalasia—anatomy matters! *The American Journal of Gastroenterology*, 114(9):1455–1463, 2019.

[30] Wenjun Kou, John E. Pandolfino, Peter J. Kahrilas, and Neelesh A. Patankar. Studies of abnormalities of the lower esophageal sphincter during esophageal emptying based on a fully coupled bolus–esophageal–gastric model. *Biomechanics and Modeling in Mechanobiology*, 17(4):1069–1082, 2018.

[31] W. Yang, T. C. Fung, K. S. Chian, and C. K. Chong. Viscoelasticity of Esophageal Tissue and Application of a QLV Model. *Journal of Biomechanical Engineering*, 128(6):909–916, 05 2006.

[32] W. YANG, T. C. FUNG, K. S. CHIAN, and C. K. CHONG. Investigations of the viscoelasticity of esophageal tissue using incremental stress-relaxation test and cyclic extension test. *Journal of Mechanics in Medicine and Biology*, 06(03):261–272, 2006.

[33] J. L. Puckett, V. Bhalla, J. Liu, G. Kassab, and R. K. Mittal. Oesophageal wall stress and muscle hypertrophy in high amplitude oesophageal contractions§. *Neurogastroenterology & Motility*, 17(6):791–799, 2005.

[34] P. Jacob, P.J. Kahrilas, J.A. Logemann, V. Shah, and T. Ha. Upper esophageal sphincter opening and modulation during swallowing. *Gastroenterology*, 97(6):1469 – 1478, 1989.

[35] Ivan M Lang and Reza Shaker. Anatomy and physiology of the upper esophageal sphincter. *The American Journal of Medicine*, 103(5, Supplement 1):50S – 55S, 1997.

[36] W. Yang, T. C. Fung, K. S. Chian, and C. K. Chong. Directional, Regional, and Layer Variations of Mechanical Properties of Esophageal Tissue and its Interpretation Using a Structure-Based Constitutive Model. *Journal of Biomechanical Engineering*, 128(3):409–418, 11 2005.

[37] W. Kou, J. E. Pandolfino, P. J. Kahrilas, and N. A. Patankar. Could the peristaltic transition zone be caused by non-uniform esophageal muscle fiber architecture? a simulation study. *Neurogastroenterology & Motility*, 29(6):e13022, 2017.

[38] Wenjun Kou, John E. Pandolfino, Peter J. Kahrilas, and Neelesh A. Patankar. Simulation studies of the role of esophageal mucosa in bolus transport. *Biomechanics and Modeling in Mechanobiology*, 16(3):1001–1009, 2017.

[39] P Pouderoux, S Lin, and PJ Kahrilas. Timing, propagation, coordination, and effect of esophageal shortening during peristalsis. *Gastroenterology*, 112(4):1147–1154, 1997.

[40] Ravinder K. Mittal, Bikram Padda, Vikas Bhalla, Valmik Bhargava, and Jianmin Liu. Synchrony between circular and longitudinal muscle contractions during peristalsis in normal subjects. *American Journal of Physiology-Gastrointestinal and Liver Physiology*, 290(3):G431–G438, 2006. PMID: 16210472.

[41] Boyce E. Griffith, Richard D. Hornung, David M. McQueen, and Charles S. Peskin. An adaptive, formally second order accurate version of the immersed boundary method. *Journal of Computational Physics*, 223(1):10–49, 2007.

[42] Hank Childs, Eric Brugger, Brad Whitlock, Jeremy Meredith, Sean Ahern, David Pugmire, Kathleen Biagas, Mark Miller, Cyrus Harrison, Gunther H. Weber, Hari Krishnan, Thomas Fogal, Allen Sanderson, Christoph Garth, E. Wes Bethel, David Camp, Oliver Rübel, Marc Durant, Jean M. Favre, and Paul Navrátil. Visit: An end-user tool for visualizing and analyzing very large data. In *High Performance Visualization–Enabling Extreme-Scale Scientific Insight*, pages 357–372. October 2012.

[43] Sabine Roman, Peter J. Kahrilas, François Mion, Thomas B. Nealis, Nathaniel J. Soper, Gilles Poncet, Frédéric Nicodème, Eric Hungness, and John E. Pandolfino. Partial Recovery of Peristalsis After Myotomy for Achalasia: More the Rule Than the Exception. *JAMA Surgery*, 148(2):157–164, 02 2013.

[44] Sourav Halder, Shashank Acharya, Wenjun Kou, Peter J. Kahrilas, John E. Pandolfino, and Neelesh A. Patankar. Mechanics informed fluoroscopy of esophageal transport. *Biomechanics and Modeling in Mechanobiology*, 20(3):925–940, 2021.

[45] P.K Sahoo, S Soltani, and A.K.C Wong. A survey of thresholding techniques. *Computer Vision, Graphics, and Image Processing*, 41(2):233 – 260, 1988.

[46] Nikhil R Pal and Sankar K Pal. A review on image segmentation techniques. *Pattern Recognition*, 26(9):1277 – 1294, 1993.

[47] G. B. Coleman and H. C. Andrews. Image segmentation by clustering. *Proceedings of the IEEE*, 67(5):773–785, May 1979.

[48] R Senthilkumar, A Bharathi, B Sowmya, and K.R. Sugunamuki. Image segmentation edge detection techniques using - soft computing approaches. pages 1–6, 02 2018.

[49] Dan Ciresan, Alessandro Giusti, Luca M. Gambardella, and Jürgen Schmidhuber. Deep neural networks segment neuronal membranes in electron microscopy images. In F. Pereira, C. J. C. Burges, L. Bottou, and K. Q. Weinberger, editors, *Advances*

in Neural Information Processing Systems 25, pages 2843–2851. Curran Associates, Inc., 2012.

[50] Olaf Ronneberger, Philipp Fischer, and Thomas Brox. U-net: Convolutional networks for biomedical image segmentation. *CoRR*, abs/1505.04597, 2015.

[51] Vladimir Iglovikov and Alexey Shvets. Ternausnet: U-net with VGG11 encoder pre-trained on imagenet for image segmentation. *CoRR*, abs/1801.05746, 2018.

[52] Baris Kayalibay, Grady Jensen, and Patrick van der Smagt. Cnn-based segmentation of medical imaging data. *CoRR*, abs/1701.03056, 2017.

[53] Dzung L. Pham, Chenyang Xu, and Jerry L. Prince. Current methods in medical image segmentation. *Annual Review of Biomedical Engineering*, 2(1):315–337, 2000. PMID: 11701515.

[54] Neeraj. Sharma and Lalit. Aggarwal. Automated medical image segmentation techniques. *Journal of Medical Physics*, 35(1):3–14, 2010.

[55] A C Barnard, W A Hunt, W P Timlake, and E Varley. A theory of fluid flow in compliant tubes. *Biophysical journal*, 6(6):717–724, 1966.

[56] J.T. Ottesen. Valveless pumping in a fluid-filled closed elastic tube-system: one-dimensional theory with experimental validation. *Journal of Mathematical Biology*, 46(4):309–332, Apr 2003.

[57] Christos G. Manopoulos, Demetri S. Mathioulakis, and Sokrates G. Tsangaris. One-dimensional model of valveless pumping in a closed loop and a numerical solution. *Physics of Fluids*, 18(1):017106, 2006.

[58] Roger D. Kamm and Ascher H. Shapiro. Unsteady flow in a collapsible tube subjected to external pressure or body forces. *Journal of Fluid Mechanics*, 95(1):1–78, 1979.

[59] Monika A. Kwiatek, Ikuo Hirano, Peter J. Kahrilas, Jami Rothe, Daniel Luger, and John E. Pandolfino. Mechanical properties of the esophagus in eosinophilic esophagitis. *Gastroenterology*, 140(1):82–90, 2011.

[60] Ravinder Mittal. Motor function of the pharynx, esophagus, and its sphincters. *Colloquium Series on Integrated Systems Physiology: From Molecule to Function*, 3(3):1–84, 2011.

[61] Fan Xia, Jingfang Mao, Jinquan Ding, and Huanjun Yang. Observation of normal appearance and wall thickness of esophagus on ct images. *European Journal of Radiology*, 72(3):406 – 411, 2009.

[62] K. B. Orvar, H. Gregersen, and J. Christensen. Biomechanical characteristics of the human esophagus. *Digestive diseases and sciences*, 38(2):197–205, 1993.

[63] Rig S. Patel and Satish S. C. Rao. Biomechanical and sensory parameters of the human esophagus at four levels. *American Journal of Physiology-Gastrointestinal and Liver Physiology*, 275(2):G187–G191, 1998. PMID: 9688644.

[64] M. Raissi, P. Perdikaris, and G.E. Karniadakis. Physics-informed neural networks: A deep learning framework for solving forward and inverse problems involving nonlinear partial differential equations. *Journal of Computational Physics*, 378:686–707, 2019.

[65] Arzu Oezcelik and Steven R. DeMeester. General anatomy of the esophagus. *Thoracic Surgery Clinics*, 21(2):289–297, 2011. Thoracic Anatomy, Part II: Pleura, Mediastinum, Diaphragm, Esophagus.

[66] J. B. Hollis and D. O. Castell. Effect of dry swallows and wet swallows of different volumes on esophageal peristalsis. *Journal of Applied Physiology*, 38(6):1161–1164, 1975. PMID: 1141133.

[67] Paul A. Yushkevich, Joseph Piven, Heather Cody Hazlett, Rachel Gimpel Smith, Sean Ho, James C. Gee, and Guido Gerig. User-guided 3D active contour segmentation of anatomical structures: Significantly improved efficiency and reliability. *Neuroimage*, 31(3):1116–1128, 2006.

[68] Özgün Çiçek, Ahmed Abdulkadir, Soeren S. Lienkamp, Thomas Brox, and Olaf Ronneberger. 3D U-Net: Learning Dense Volumetric Segmentation from Sparse Annotation. *arXiv e-prints*, page arXiv:1606.06650, June 2016.

[69] Rosnah Shamsudin, Wan Wan Daud, Mohd Takrif, Osman Hassan, and Coskan Ilicali. Rheological properties of josapine pineapple juice at different stages of maturity. *International Journal of Food Science & Technology*, 44:757–762, 03 2009.

[70] Martín Abadi, Ashish Agarwal, Paul Barham, Eugene Brevdo, Zhifeng Chen, Craig Citro, Greg S. Corrado, Andy Davis, Jeffrey Dean, Matthieu Devin, Sanjay Ghemawat, Ian Goodfellow, Andrew Harp, Geoffrey Irving, Michael Isard, Yangqing Jia, Rafal Jozefowicz, Lukasz Kaiser, Manjunath Kudlur, Josh Levenberg, Dan Mane, Rajat Monga, Sherry Moore, Derek Murray, Chris Olah, Mike Schuster, Jonathon Shlens, Benoit Steiner, Ilya Sutskever, Kunal Talwar, Paul Tucker, Vincent Vanhoucke, Vijay Vasudevan, Fernanda Viegas, Oriol Vinyals, Pete Warden, Martin Wattenberg, Martin Wicke, Yuan Yu, and Xiaoqiang Zheng. Tensorflow: Large-scale machine learning on heterogeneous distributed systems, 2016.

[71] Diederik P. Kingma and Jimmy Ba. Adam: A method for stochastic optimization, 2017.

[72] Dustin A. Carlson, Alexandra J. Baumann, Erica N. Donnan, Amanda Krause, Wenjun Kou, and John E. Pandolfino. Evaluating esophageal motility beyond primary peristalsis: Assessing esophagogastric junction opening mechanics and secondary peristalsis in patients with normal manometry. *Neurogastroenterology & Motility*, 33(10):e14116, 2021.

[73] Edoardo Savarino, Massimiliano di Pietro, Albert J. Bredenoord, Dustin A. Carlson, John O. Clarke, Abraham Khan, Marcelo F. Vela, Rena Yadlapati, Daniel Pohl, John E. Pandolfino, Sabine Roman, and C. Prakash Gyawali. Use of the functional lumen imaging probe in clinical esophagology. *The American Journal of Gastroenterology*, 115(11):1786–1796, 2020.

[74] Dustin A. Carlson. Functional lumen imaging probe: The flip side of esophageal disease. *Current Opinion in Gastroenterology*, 32(4):310–318, 2016.

[75] Ezra N. Teitelbaum, Lubomyr Boris, Fahd O. Arafat, Frédéric Nicodème, Zhiyue Lin, Peter J. Kahrilas, John E. Pandolfino, Nathaniel J. Soper, and Eric S. Hungness. Comparison of esophagogastric junction distensibility changes during poem and heller myotomy using intraoperative flip. *Surgical Endoscopy*, 27(12):4547–4555, 2016.

[76] Ryan A. J. Campagna, Dustin A. Carlson, Eric S. Hungness, Amy L. Holmstrom, John E. Pandolfino, Nathaniel J. Soper, and Ezra N. Teitelbaum. Intraoperative assessment of esophageal motility using flip during myotomy for achalasia. *Surgical Endoscopy*, 34(6):2593–2600, 2013.

[77] Shashank Acharya, Sourav Halder, Dustin A. Carlson, Wenjun Kou, Peter J. Kahrilas, John E. Pandolfino, and Neelesh A. Patankar. Estimation of mechanical work done to open the esophagogastric junction using functional lumen imaging probe panometry. *American Journal of Physiology-Gastrointestinal and Liver Physiology*, 320(5):G780–G790, 2021. PMID: 33655760.

[78] Travers Ching, Daniel S. Himmelstein, Brett K. Beaulieu-Jones, Alexandr A. Kalinin, Brian T. Do, Gregory P. Way, Enrico Ferrero, Paul-Michael Agapow, Michael Zietz, Michael M. Hoffman, Wei Xie, Gail L. Rosen, Benjamin J. Lengerich, Johnny Israeli, Jack Lanchantin, Stephen Woloszynek, Anne E. Carpenter, Avanti Shrikumar, Jinbo Xu, Evan M. Cofer, Christopher A. Lavender, Srinivas C. Turaga,

Amr M. Alexandari, Zhiyong Lu, David J. Harris, Dave DeCaprio, Yanjun Qi, Anshul Kundaje, Yifan Peng, Laura K. Wiley, Marwin H. S. Segler, Simina M. Boca, S. Joshua Swamidass, Austin Huang, Anthony Gitter, and Casey S. Greene. Opportunities and obstacles for deep learning in biology and medicine. *Journal of The Royal Society Interface*, 15(141):20170387, 2018.

[79] Andre Esteva, Alexandre Robicquet, Bharath Ramsundar, Volodymyr Kuleshov, Mark DePristo, Katherine Chou, Claire Cui, Greg Corrado, Sebastian Thrun, and Jeff Dean. A guide to deep learning in healthcare. *Nature Medicine*, 25(1):24–29, 2019.

[80] Oliver Faust, Yuki Hagiwara, Tan Jen Hong, Oh Shu Lih, and U Rajendra Acharya. Deep learning for healthcare applications based on physiological signals: A review. *Computer Methods and Programs in Biomedicine*, 161:1–13, 2018.

[81] Pavel Hamet and Johanne Tremblay. Artificial intelligence in medicine. *Metabolism*, 69:S36–S40, 2017. Insights Into the Future of Medicine: Technologies, Concepts, and Integration.

[82] Fei Jiang, Yong Jiang, Hui Zhi, Yi Dong, Hao Li, Sufeng Ma, Yilong Wang, Qiang Dong, Haipeng Shen, and Yongjun Wang. Artificial intelligence in healthcare: past, present and future. *Stroke and Vascular Neurology*, 2(4):230–243, 2017.

[83] Riccardo Miotto, Fei Wang, Shuang Wang, Xiaoqian Jiang, and Joel T Dudley. Deep learning for healthcare: review, opportunities and challenges. *Briefings in Bioinformatics*, 19(6):1236–1246, 05 2017.

[84] Francesco Piccialli, Vittorio Di Somma, Fabio Giampaolo, Salvatore Cuomo, and Giancarlo Fortino. A survey on deep learning in medicine: Why, how and when? *Information Fusion*, 66:111–137, 2021.

[85] Eric J. Topol. High-performance medicine: the convergence of human and artificial intelligence. *Nature Medicine*, 25(1):44–56, 2019.

[86] KH. Yu, A.L. Beam, and I.S. Kohane. Artificial intelligence in healthcare. *Nature Biomedical Engineering*, 2(10):719–731, 2018.

[87] Catherine Le Berre, William J. Sandborn, Sabeur Aridhi, Marie-Dominique Devignes, Laure Fournier, Malika Smaïl-Tabbone, Silvio Danese, and Laurent Peyrin-Biroulet. Application of artificial intelligence to gastroenterology and hepatology. *Gastroenterology*, 158(1):76–94.e2, 2020.

[88] James K. Ruffle, Adam D. Farmer, and Qasim Aziz. Artificial intelligence-assisted gastroenterology— promises and pitfalls. *The American Journal of Gastroenterology*, 114(3):422–428, 2019.

[89] Young Joo Yang and Chang Seok Bang. Application of artificial intelligence in gastroenterology. *World journal of gastroenterology*, 25(14):1666–1683, 2019.

[90] Wenjun Kou, Dustin A. Carlson, Alexandra J. Baumann, Erica Donnan, Yuan Luo, John E. Pandolfino, and Mozziyar Etemadi. A deep-learning-based unsupervised model on esophageal manometry using variational autoencoder. *Artificial Intelligence in Medicine*, 112:102006, 2021.

[91] Diederik P Kingma and Max Welling. Auto-encoding variational bayes, 2014.

[92] Dustin A. Carlson, C. Prakash Gyawali, Abraham Khan, Rena Yadlapati, Joan Chen, Reena V. Chokshi, John O. Clarke, Jose M. Garza, Anand S. Jain, Philip Katz, Vani Konda, Kristle Lynch, Felice H. Schnoll-Sussman, Stuart J. Spechler, Marcelo F. Vela, Jacqueline E. Prescott, Alexandra J. Baumann, Erica N. Donnan, Wenjun Kou, Peter J. Kahrilas, and John E. Pandolfino. Classifying esophageal motility by flip panometry: A study of 722 subjects with manometry. *The American Journal of Gastroenterology*, 116(12):2357–2366, 2021.

[93] H. Al-Jafar, M. Laffan, S. Al-Sabah, M. Elmorsi, M. Habeeb, and F. Alnajar. Severe recurrent achalasia cardia responding to treatment of severe autoimmune acquired haemophilia. *Case Reports in Gastroenterology*, 6(3):618–623, 2012.

[94] Edoardo Savarino, Lorenzo Gemignani, Patrizia Zentilin, Nicola De Bortoli, Alberto Malesci, Luca Mastracci, Roberto Fiocca, and Vincenzo Savarino. Achalasia with dense eosinophilic infiltrate responds to steroid therapy. *Clinical Gastroenterology and Hepatology*, 9(12):1104–1106, 2011.

[95] Stuart Jon Spechler, Vani Konda, and Rhonda Souza. Can eosinophilic esophagitis cause achalasia and other esophageal motility disorders? *American Journal of Gastroenterology*, 113(11):1594–1599, 2018.

[96] John G. Hunter, Thadeus L. Trus, Gene D. Branum, and J. Patrick Waring. Laparoscopic heller myotomy and fundoplication for achalasia. *Annals of Surgery*, 225(6):655–665, 1997.

[97] William O. Richards, Alfonso Torquati, Michael D. Holzman, Leena Khaitan, Daniel Byrne, Rami Lutfi, and Kenneth W. Sharp. Heller myotomy versus heller myotomy with dor fundoplication for achalasia: A prospective randomized double-blind clinical trial. *Annals of Surgery*, 240(3):405–415, 2004.

[98] H. Inoue, H. Minami, Y. Kobayashi, Y. Sato, M. Kaga, M. Suzuki, H. Satodate, N. Odaka, H. Itoh, and S. Kudo. Peroral endoscopic myotomy (poem) for esophageal achalasia. *Endoscopy*, 42(4):265–271, 2010.

[99] Daniel Von Renteln, Karl–Hermann Fuchs, Paul Fockens, Peter Bauerfeind, Melina C. Vassiliou, Yuki B. Werner, Gerald Fried, Wolfram Breithaupt, Henriette Heinrich, Albert J. Bredenoord, Jan F. Kersten, Tessa Verlaan, Michael Trevisonno, and Thomas Rösch. Peroral endoscopic myotomy for the treatment of achalasia: An international prospective multicenter study. *Gastroenterology*, 145(2):309–311.e3, 2013.

[100] Alexander Buslaev, Vladimir I. Iglovikov, Eugene Khvedchenya, Alex Parinov, Mikhail Druzhinin, and Alexandr A. Kalinin. Albumentations: Fast and flexible image augmentations. *Information*, 11(2), 2020.

[101] F. Pedregosa, G. Varoquaux, A. Gramfort, V. Michel, B. Thirion, O. Grisel, M. Blondel, P. Prettenhofer, R. Weiss, V. Dubourg, J. Vanderplas, A. Passos, D. Cournapeau, M. Brucher, M. Perrot, and E. Duchesnay. Scikit-learn: Machine learning in Python. *Journal of Machine Learning Research*, 12:2825–2830, 2011.

[102] Charles A. Taylor and Mary T. Draney. Experimental and computational methods in cardiovascular fluid mechanics. *Annual Review of Fluid Mechanics*, 36(1):197–231, 2004.

[103] James B. Grotberg. Respiratory fluid mechanics and transport processes. *Annual Review of Biomedical Engineering*, 3(1):421–457, 2001. PMID: 11447070.

[104] Aranyak Chakravarty, Mahesh V. Panchagnula, Alladi Mohan, and Neelesh A. Patankar. Pulmonary drug delivery and retention: A computational study to identify plausible parameters based on a coupled airway-mucus flow model. *PLOS Computational Biology*, 18(6):1–15, 06 2022.

[105] François Chollet et al. Keras. `https://keras.io`, 2015.

APPENDIX A

Immersed boundary method for the vEsophagus

The vEsophagus was modeled as a fluid-structure interaction system using Immersed boundary (IB) method. In this method, the structure (esophagus) is represented using Lagrangian coordinates, and the fluid is represented using Eulerian coordinates. The governing equations are as follows:

$$\rho\left(\frac{\partial \boldsymbol{u}}{\partial t}+\boldsymbol{u}\cdot\nabla\mathbf{u}\right)=-\nabla p+\mu\nabla^2\boldsymbol{u}+\boldsymbol{f}, \tag{A.1}$$

$$\nabla\cdot\boldsymbol{u}=0, \tag{A.2}$$

$$\boldsymbol{f}(\boldsymbol{x},t)=\int_\Gamma \boldsymbol{F}(\boldsymbol{s},t)\delta\left(\boldsymbol{x}-\boldsymbol{X}(\boldsymbol{s},t)\right)d\boldsymbol{s}, \tag{A.3}$$

$$\int_\Gamma \boldsymbol{F}(\boldsymbol{s},t)\cdot\boldsymbol{V}(\boldsymbol{s})d\boldsymbol{s}=-\int_\Gamma \mathbf{P}:\nabla_{\boldsymbol{s}}\boldsymbol{V}(\boldsymbol{s})d\boldsymbol{s},\forall\boldsymbol{V}(\boldsymbol{s}), \tag{A.4}$$

$$\boldsymbol{U}(\boldsymbol{x},t)=\int_\Omega \boldsymbol{u}(\boldsymbol{x},t)\delta\left(\boldsymbol{x}-\boldsymbol{X}(\boldsymbol{s},t)\right)d\boldsymbol{x}, \tag{A.5}$$

$$\int_\Gamma \frac{\partial \boldsymbol{X}(\boldsymbol{s},t)}{\partial t}\cdot\boldsymbol{V}(\boldsymbol{s})d\boldsymbol{s}=-\int_\Gamma \boldsymbol{U}(\boldsymbol{s},t)\cdot\boldsymbol{V}(\boldsymbol{s})d\boldsymbol{s},\forall\boldsymbol{V}(\boldsymbol{s}), \tag{A.6}$$

$$\mathbf{P}=\mathcal{P}\left[\boldsymbol{X}(\cdot,t)\right], \tag{A.7}$$

wherein Equations A.1 and A.2 are the momentum and mass conservation equations for an incompressible fluid-structure system in Eulerian description. $\boldsymbol{u}$ and p are the Eulerian velocity and pressure, respectively. ρ and μ are the density and viscosity of the entire system. In this case, fluid was assumed to be Newtonian and had a density and viscosity

of 1000 kg/m^3 and 10 cP, respectively. The esophageal wall was assumed to have the same density and viscosity as the fluid to avoid buoyancy effect in the IB method. Equations A.3 - A.6 are the IB fluid-structure equations, where $\boldsymbol{f}$ and $\boldsymbol{F}$ are the Eulerian and Lagrangian elastic force density, respectively. $\boldsymbol{U}$, $\boldsymbol{X}$ and $\mathbf{P}$ are the structure velocity, position, and first Piola-Kirchhoff stress, respectively. Equation A.7 is a generic form representing the relation between $\mathbf{P}$ and the hyperelastic strain energy function that define the elastic behavior of the structure.

In IB method, the whole vEsophagus model is immersed in a fluid box that include the fluid bolus inside the esophagus. The proximal end of the vEsophagus is fixed with zero outflow to account for the closed UES once the bolus is inside the esophagus. For simulation set 1 and 2, the lower end of the esophagus is also fixed to model the extreme scenario of fully occluded EGJ. For simulation set 3, the lower end of the esophagus is free to move. In all these simulations, the sides of the esophagus do not have any constraint and are free to move. We have imposed zero velocity boundary condition at the upper surface of the fluid domain. The same boundary condition was also imposed at the lower surface for simulation set 1 and 2. For simulation set 3, the lower fluid surface has free outflow boundary condition. The other 4 outer surfaces of the fluid domain for all these simulations have free outflow boundary condition enforced.

APPENDIX B

Image segmentation of fluoroscopy

A convolutional neural network architecture (CNN) called TernausNet [**51**] was used to perform image segmentation. TernausNet is a modified form of the classical UNet [**50**] which consists of an encoder and decoder path with skip connections that combine feature maps from the encoder and decoder paths leading to precise localization. TernausNet takes advantage of transfer learning by replacing the encoder part of U-Net with VGG11/VGG16 network pretrained on ImageNet dataset, which consists of millions of images. Therefore, the low-level features learned from a huge dataset can be efficiently utilized and the total number of parameters to be learned is reduced significantly. In this work, the encoder part consists of VGG16. The decoder path is similar to that of the original TernausNet with the slight modification of having two sets of Conv 3×3 and ReLU at each level instead of one. The full network architecture is shown in Figure B.1. In order to prevent over-fitting, we have also introduced batch normalization after every convolution layer in the decoder section. The whole network consists of 36,319,201 parameters, of which 28,676,001 were pre-trained and 7,643,200 were trained.

To train the CNN, it is necessary to have a dataset of esophagram images that show the bolus at various locations along the length of the esophagus in different shapes and sizes. We used 136 esophagram images collected from a total of 99 different swallows from 14 different subjects that include both normal controls and patients. The sole purpose of the CNN is to identify the bolus from the background, and for that, it does not require

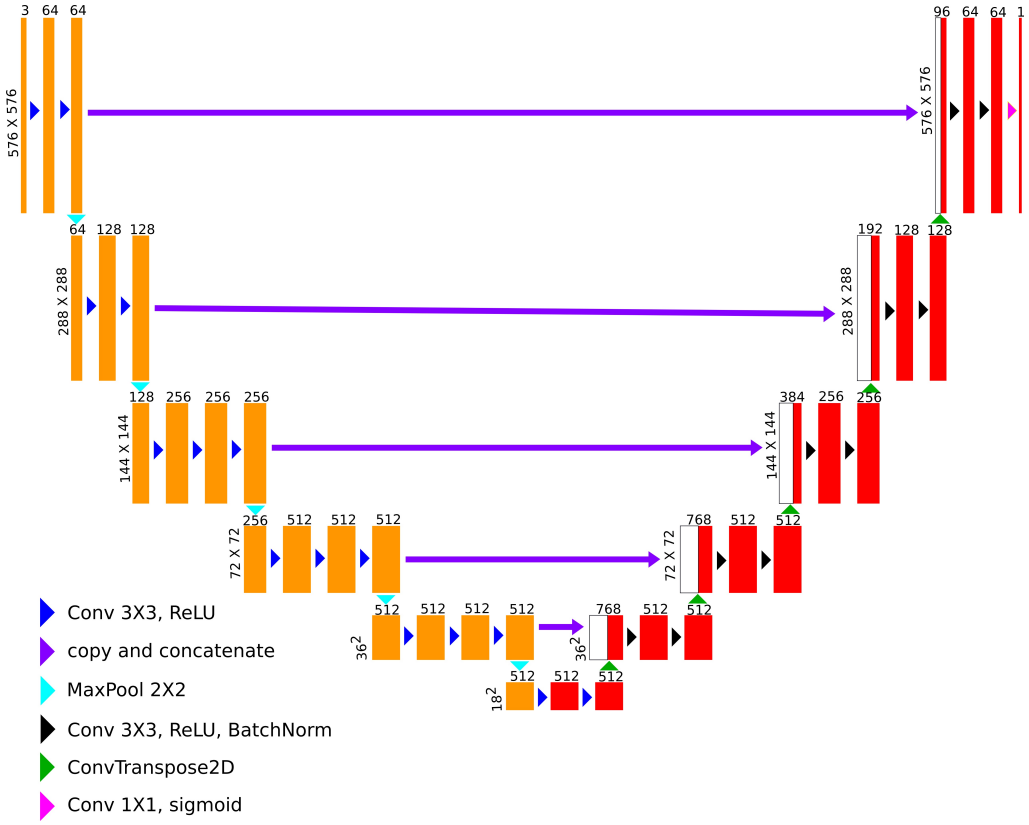

Figure B.1. Neural network architecture (based on TernausNet). The feature maps marked in yellow represents the VGG16 encoder pre-trained with the ImageNet dataset. The feature maps in red represent the decoder which is trained using the fluoroscopy images

to be trained with fluoroscopy images from a large cohort of subjects that include both normal controls and patients with a large variety of esophageal disorders. The 136 images along with augmentations contained enough variability and were large enough to train and validate the CNN to identify the bolus in any fluoroscopy image irrespective of the state of the esophagus. Each of these images has a size of 576×576 pixels. We obtained these images from VFSE done in association with HRM recordings (hence, the presence of the catheter in Figure 3.1(a)). These images were manually segmented for labeling as shown in Figure 3.1(b). Since the training dataset is very small, it makes sense to take advantage

Table B.1. Details of data augmentations for fluoroscopy images

Augmentation type	**Range**	
	min	max
Rotation	-10.0^{o}	10.0^{o}
Width shift	-10%	10%
Height shift	-10%	10%
Brightness	50%	150%
Shear	-5^{o}	5^{o}
Zoom	80%	120%
Piecewise affine	0	0.03

of transfer learning through the pre-trained encoder to prevent over-fitting. In addition to that, we have also implemented various image augmentations such as rotation, height and width shifts, varying brightness, shearing, piecewise affine and scaling. This was done to prevent overfitting due to the lack of a huge dataset and to introduce generalizability into the model. These augmentations were applied randomly to varying extents, the range of which is provided in Table B.1.

The dataset of 136 images was divided into two parts: 112 images for training and 24 images for validation. This is a semantic segmentation problem, wherein each pixel belongs to one of the two classes: 1 for bolus and 0 for the background. We used a sum of binary crossentropy (BCE) and negative Intersection over Union (IOU) loss functions as the total loss (L) defined as follows:

$$BCE = -\frac{1}{N}\sum_{i=1}^{N}\left[y_i \log\left(\hat{y}_i\right) + \left(1-y_i\right)\log\left(1-\hat{y}_i\right)\right], \tag{B.1}$$

$$IOU = \frac{1}{N}\sum_{i=1}^{N}\frac{y_i\hat{y}_i + \epsilon}{y_i + \hat{y}_i - y_i\hat{y}_i + \epsilon}, \tag{B.2}$$

$$L = BCE - IOU, \tag{B.3}$$

where N is the total number of pixels in the output, y_i and $\hat{y}_i$ are the target binary value and predicted value of the i-th pixel, respectively. The ϵ added in the numerator and denominator of IOU is a small number ($= 10^{-7}$), which is introduced to calculate IOU over both the classes: bolus and background. To evaluate the performance of the model, the predicted images were converted to their binary forms using various thresholds between 0.5 and 1.0, and IOU were calculated for each of them and then averaged.

The model was trained for 200 epochs with batches of 2 images using Keras, a high-level neural network API [**105**], which runs on top of TensorFlow [**70**], to train the network. The training was performed using RMSProp optimization algorithm with a learning rate of 0.001. The Intersection over Union for the validation set obtained at the end of the training was 0.75, which was good enough for our analysis, and show that the trained CNN is generalized to predict on a large variety of fluoroscopy images. The segmented output images were converted to binary form using a threshold of 0.5 for the final output. Some of the image frames for a sequence of images generated from a VFSE and the predicted segmentation of those images after thresholding are shown in Figure 3.2(a)-(j).

The sharp interface between the white and dark regions of the segmented images marks the outline of the bolus. It gives the shape of the inner mucosal surface of the esophagus at the location of the bolus, but no information about regions of esophageal contraction or relaxation. The diameter of the catheter (dashed curve in Figure 3.1(a)) is approximately 4.2 mm. We used this as the scale for mapping the pixel data to length. In some image frames, the relaxed diameter of the esophagus can be identified at some locations along the length due to remnant barium lining the lumen. To simplify our analysis, we assumed that this diameter is the relaxed diameter of the esophagus throughout its length, although,

in reality, the esophagus may be collapsed or the inner diameter may vary along the length [**61**]. The semantic segmentation performed on the esophagram images basically assigns each pixel to one of the two classes: bolus (white region) and the remainder (dark region). The resulting segmented images do not show a smooth boundary for the bolus and is irregular at the scale of the resolution of the original image. Also, since the segmentation is done on each of the images separately, the continuity between the images at consecutive time frames is broken. Therefore, the pixel data were smoothed both in space and time without the loss of bolus geometry detail. The smoothing is performed by Gaussian weighted moving average over a window of 10 and 30 points in space and time, respectively.

APPENDIX C

Kullback–Leibler divergence for mechanics-informed VAE (MI-VAE)

The MI-VAE learns to model an input dataset as a distribution, $p(\theta)$ such that the input variable θ is generated from a likelihood distribution $p(\theta|z)$, where z is the latent variable. This distribution $p(\theta)$ is parameterized by the weights of the neural network. The decoder yields the likelihood distribution $p(\theta, z)$, i.e., it takes z as input and outputs θ. The encoder should ideally yield the posterior distribution $p(z|\theta)$. Unfortunately, $p(z|\theta)$ is computationally intractable in general. So, in practice, the encoder yields a conditional distribution $q(z|\theta)$ which approximates $p(z|\theta)$. The Kullback-Leibler divergence (KLD) provides a measure of the difference between the two distributions $q(z|\theta)$ and $p(z|\theta)$, and leads to the following relation:

(C.1)

$$D_{KL}\left[q\left(z|\theta\right)\|p\left(z|\theta\right)\right] = -\int q\left(z|\theta\right)\left[\log p\left(\theta|z\right) + \log p(z) - \log q\left(z|\theta\right)\right] dz + \log p(\theta).$$

Since KLD is always positive, the right-hand side of the above expression can be written as follows:

(C.2)

$$p(\theta) \geq \int q\left(z|\theta\right)\left[\log p\left(\theta|z\right) + \log p(z) - \log q\left(z|\theta\right)\right] dz.$$

The above equation can be re-written in terms of a new KLD form as follows:

$$p(\theta) \geq -D_{KL}\left[q(z|\theta)\|p(z)\right] + \mathbb{E}_{z\sim q(z|\theta)}\left[\log p(\theta|z)\right], \tag{C.3}$$

where $\mathbb{E}_{z\sim q(z|\theta)}\left[\log p(\theta|z)\right]$ is the joint log-likelihood of the input θ and the latent variable z. The right-hand side is called the Evidence Lower bound (ELBO) and is named so since it estimates the lower bound of the likelihood of the data. Thus, maximizing ELBO maximizes the likelihood of the data. The KLD term works like a regulariser and forces the approximate posterior $q(z|\theta)$ to be as close to the prior $p(z)$ as possible. This term causes the posterior $q(z|\theta)$ to enforce a high probability to z values that can generate the point θ without collapsing to a single point like an autoencoder. This gives a continuous behavior to the latent space so that meaningful generations are possible from points in the latent space which are not related to any input in the training dataset. The second term of Equation C.3 is the reconstruction error between in the input and the generated output of the entire network. It is possible to derive a closed form solution for the KLD term if we choose the approximate posterior $q(z|\theta)$ to have a Gaussian distribution and choose the prior $p(z)$ to have a standard normal distribution as shown below:

$$-D_{KL}\left[q(z|\theta)\|p(z)\right] = \frac{1}{2}\left[1 + \log\sigma_q^2 - \sigma_q^2 - \mu_q^2\right]. \tag{C.4}$$

The encoder, as shown in Figure 5.4, outputs μ_q^2 and $\log\sigma_q^2$. Although we have an analytical form for the KLD term of Equation C.3, the reconstruction error requires to be estimated by sampling. Sampling z from $q(z|\theta)$ directly leads to a problem in implementing backpropagation since the network would have a random node at the input of decoder. This problem can be tackled by a reparameterization trick where z is sampled from the

mean and log variance parameters of $q(z|\theta)$ as estimated by the encoder shown as follows:

$$z = \mu_q + \varepsilon \cdot \exp\left(\frac{1}{2}\log\sigma_q^2\right), \tag{C.5}$$

where ε is a random number generated from a standard normal distribution. This step makes it possible to backpropagate in a deterministic manner by considering ε as an extra input. Since ε is sampled from a different distribution which is not a function of any variables with respect to which derivatives might be required, stochasticity is introduced in the network without affecting backpropagation. The final form of the loss function used for the MI-VAE is as follows:

$$L := \frac{1}{2M}\sum_{i}^{M}\left[1 + \log\sigma_{q,i}^2 - \sigma_{q,i}^2 - \mu_{q,i}^2\right] + \frac{\beta}{N}\sum_{j}^{N}\left(\theta_j - \hat{\theta}_j\right)^2, \tag{C.6}$$

where M is the dimension of the latent space, N is the product of the two spatial dimensions of the input and generated output. In this case, $M = 24$ and $N = 256$. The first term is the KLD and the second term is the reconstruction loss. β is a scaling parameter used to balance the magnitudes of the reconstruction loss and the KLD for proper training of MI-VAE.